# Stochastic Maxwell's Equations:

# Robust Reconstruction of Wave Dynamics from Sensor Data and Optimal Observation Time

by

Bryce Barclay

A Dissertation Presented in Partial Fulfillment
of the Requirements for the Degree
Doctor of Philosophy

Approved June 2023 by the
Graduate Supervisory Committee:

Alex Mahalov, Co-Chair
Eric Kostelich, Co-Chair
Mohamed Moustaoui
Sebastien Motsch
Rodrigo Platte

ARIZONA STATE UNIVERSITY

August 2023

ABSTRACT

This work presents a thorough analysis of reconstruction of global wave fields (governed by the inhomogeneous wave equation and the Maxwell vector wave equation) from sensor time series data of the wave field. Three major problems are considered. First, an analysis of circumstances under which wave fields can be fully reconstructed from a network of fixed-location sensors is presented. It is proven that, in many cases, wave fields can be fully reconstructed from a single sensor, but that such reconstructions can be sensitive to small perturbations in sensor placement. Generally, multiple sensors are necessary. The next problem considered is how to obtain a global approximation of an electromagnetic wave field in the presence of an amplifying noisy current density from sensor time series data. This type of noise, described in terms of a cylindrical Wiener process, creates a nonequilibrium system, derived from Maxwell's equations, where variance increases with time. In this noisy system, longer observation times do not generally provide more accurate estimates of the field coefficients. The mean squared error of the estimates can be decomposed into a sum of the squared bias and the variance. As the observation time $\tau$ increases, the bias decreases as $\mathcal{O}(1/\tau)$ but the variance increases as $\mathcal{O}(\tau)$. The contrasting time scales imply the existence of an "optimal" observing time (the bias-variance tradeoff). An iterative algorithm is developed to construct global approximations of the electric field using the optimal observing times. Lastly, the effect of sensor acceleration is considered. When the sensor location is fixed, measurements of wave fields composed of plane waves are almost periodic and so can be written in terms of a standard Fourier basis. When the sensor is accelerating, the resulting time series is no longer almost periodic. This phenomenon is related to the Doppler effect, where a time transformation must be performed to obtain the frequency and amplitude information from the time series data. To obtain frequency and amplitude information from accelerating sensor time

series data in a general inhomogeneous medium, a randomized algorithm is presented. The algorithm is analyzed and example wave fields are reconstructed.

# ACKNOWLEDGMENTS

I would like to thank so many people for supporting me, both professionally and personally, during my time as a PhD student.

Thank you to my advisors—Alex and Eric. Thank you for teaching me countless skills for my research and thank you for being available in the evenings and the weekends to discuss research.

Thank you to my committee—Drs. Motsch, Moustaoui, and Platte. I have learned a lot from my interactions with each of you through classes and research projects. Discussing research with each of you has always been engaging which is why I am excited to present this dissertation to you.

Thank you to my family and friends—Mom, Dad, Ryan, Nicole, Demetri, Sam, Drew, Chelsea, Nikolay, Hezekiah, and Braden. Thank you for spending time with me when I needed a break from work and thank you to my friends at ASU for discussing math when I needed a break from work but still wanted to think about math.

This work was partially supported by the Air Force Office of Scientific Research under award numbers FA9550-23-1-0177 and FA9550-19-1-0064.

TABLE OF CONTENTS

CHAPTER Page

LIST OF FIGURES

Chapter 1

# INTRODUCTION

Waves are ubiquitous in nature with many important applications in science and engineering today [3]. Waves occur in areas as diverse as geophysics [11], acoustics, and electromagnetics [18, 31]. In their simplest form, waves are solutions to the wave equation:

$$\frac{\partial^2 u}{\partial t^2} - c^2(\mathbf{x})\Delta u = F(\mathbf{x}, t) \tag{1.1}$$

as is the case for acoustics where $u$ represents pressure and $c$ represents the wave speed, and the simplest solutions are superpositions of plane waves:

$$u(\mathbf{x}, t) = \sum_{n=1}^{\infty} A_n \exp(i(\mathbf{k}_n \cdot \mathbf{x} - \omega_n t)) \tag{1.2}$$

where the angular frequency $\omega$ and wavenumber $\mathbf{k}$ are related by $\omega^2 = c^2|\mathbf{k}|^2$, known as the dispersion relation. Other types of waves can be differentiated from this simple case in several ways: governing equations for wave phenomena can be nonlinear, inhomogeneous, and have different dispersion relations.

In this dissertation, we consider acoustic and electromagnetic waves. For the former, (1.1) is the governing equation. The latter is governed by Maxwell's equations and is vectorial. A wave equation for the electric field $\mathbf{E}$ can be obtained from Faraday's law of induction and Ampére's law giving the Maxwell vector wave equation:

$$\epsilon(\mathbf{x})\frac{\partial^2 \mathbf{E}}{\partial t^2} + \nabla \times \left([\mu(\mathbf{x})]^{-1}\nabla \times \mathbf{E}\right) = -\frac{\partial \mathbf{J}}{\partial t} \tag{1.3}$$

where $\epsilon$, $\mu$, and $\mathbf{J}$ are the permittivity, permeability, and current density, respectively.

For the general cases of (1.1) and (1.3), an explicit representation such as (1.2) cannot be obtained. Instead, the wave field is written as

$$u(\mathbf{x}, t) = \sum_{n=1}^{\infty} A_n \exp(-i\omega_n t)\Phi_n(\mathbf{x}) \tag{1.4}$$

where the functions $\Phi_n$ are the "features" of the problem. In the case of (1.1), $\Phi_n$ are eigenfunctions of the weighted Laplace operator. For the Maxwell vector wave equation (1.3), the functions $\Phi_n$ are replaced with the vector-valued eigenfunctions $\mathbf{\Phi}_n$ of the weighted curl-squared operator. The requirement of the features in both cases is that they are mutually orthogonal. The features framework is general and used in other areas such as machine learning and compressed sensing [29].

The primary question of interest in this work is whether wave fields such as (1.4) can be fully reconstructed or approximated using time series data of the wave field:

$$R_s(t) := u(\mathbf{x}_s(t), t) \tag{1.5}$$

obtained from a sensor. Here, $\mathbf{x}_s(t)$ is the spatial trajectory of the sensor.

Consider the following simple reconstruction example. Suppose we want to construct an approximation of the acoustic wave field $u(\mathbf{x}, t)$ of a human voice given by (1.4) using a time series of observations $R_{\mathbf{s}}(t) = u(\mathbf{s}, t)$ obtained from a sensor fixed at the location $\mathbf{s}$. The time series takes the form

$$R_{\mathbf{s}}(t) = \sum_n A_n \exp\left(-i\omega_n t\right) \Phi_n(\mathbf{s}) = \sum_n D_n \exp\left(-i\omega_n t\right) \tag{1.6}$$

where the frequencies of the human voice $\omega_n$ are contained in a bounded range $[\omega_{min}, \omega_{max}]$ such as 300-3,000 Hz. Since this time series is almost periodic, the inner product

$$(R_{\mathbf{s}}(t), \exp(-i\omega t)) := \lim_{\tau\to\infty} \frac{1}{\tau} \int_0^{\tau} R_{\mathbf{s}}(t) \exp(i\omega t)\, dt \tag{1.7}$$

can be used to obtain the frequencies $\omega_n$ and coefficients $D_n$. The time series of the wave field at another location $\mathbf{s}_0$ is then

$$R_{\mathbf{s}_0}(t) = \sum_n D_n \frac{\Phi_n(\mathbf{s}_0)}{\Phi_n(\mathbf{s})} \exp\left(-i\omega_n t\right).$$

This formula implicitly assumes that $\Phi_n(\mathbf{x}) \neq 0$ at the sensor location $\mathbf{x} = \mathbf{s}$ which is a requirement of reconstruction.

This dissertation is organized as follows. In chapter 2, we consider a network of fixed-location sensors and how the number of sensors affects wave field reconstruction. In chapter 3, we consider reconstruction of the electric field from a fixed-location sensor in the presence of a noisy current density. In terms of the Maxwell vector wave equation, this amounts to additive noise:

$$\frac{\partial \mathbf{J}}{\partial t} := \left\langle \frac{\partial \mathbf{J}}{\partial t} \right\rangle (\mathbf{x}, t) + \sqrt{Q} \frac{\partial \mathcal{W}}{\partial t} \tag{1.8}$$

where $\langle \cdot \rangle$ denotes the ensemble average and $\mathcal{W}$ is a cylindrical Wiener process. In chapter 4, we consider the problem of wave field reconstruction from an accelerating sensor. We make concluding remarks in chapter 5.

Chapter 2

# SENSOR PLACEMENT SENSITIVITY AND ROBUST RECONSTRUCTION OF WAVE DYNAMICS FROM MULTIPLE SENSORS

## 2.1 Introduction

Wave propagation is a classical physical problem with wide application in electromagnetics, acoustics, and geo- and astrophysics. Of particular interest is to capture data at a specific location to determine properties of the wave field. For example, in wave gradiometry, sensor arrays are used to determine properties of seismic waves, such as geometric spreading and horizontal slowness [35]. In 2013, the National Research Council listed the deployment of small satellite constellations, which would expand the use of multiple sensors to capture wave dynamics, as a priority for the coming decade [8]. Data assimilation strategies have been developed to incorporate both sensor data and physics phenomena in ionospheric modeling [16]. Kak *et al.* [32] recently proved some necessary placement conditions to optimize the design of large CubeSat constellations for low-orbit, "Internet of Things" communication networks. Ma *et al.* [37] have evaluated statistical and physical models to predict the distribution of electromagnetic waves in complex enclosures.

Advancements in sensor technology motivate the present study, which addresses two main questions. First, under what conditions are multiple sensors required to reconstruct solutions of the wave equation? Second, how do multiple sensors reduce errors in the reconstructions? The mathematical tools we develop are more general and apply to systems such as Maxwell's equations; however, we illustrate the general methodology on the forced wave equation. It is useful to characterize full solution

reconstruction in terms of time series. Full solution reconstruction is equivalent to time series reconstruction at every point in the spatial domain. Therefore, a useful rephrasing of the stated problem is the following: how many sensors are required to reconstruct a time series at every location? We prove three main results: (1) time series from a single sensor can be used to reconstruct solutions to the wave equation for a large class of problems but does not suffice for full reconstruction in the general case. A proposed method that uses multiple sensors can provide full reconstruction; (2) solution reconstruction from a single sensor is highly sensitive to perturbations in sensor location; and (3) given $n$ noisy sensors, the error in solution reconstruction decreases as $\mathcal{O}(n^{-1/2})$. These results are mathematically rigorous and provide necessary conditions for reconstruction of wave dynamics. We also present numerical simulations to demonstrate the theory.

Our theoretical approach relies on the eigenfunctions of the weighted Laplace operator. Although the use of eigenfunction expansions is classical, to our knowledge its application to questions of sensor placement and wave field reconstruction is new. Furthermore, there are interesting connections with some mathematical approaches used in machine learning and compressed sensing. The latter case, as in [29], can be described as choosing "features" $\{\psi_i\}$ to model the data as $u(\mathbf{x}, t) = \sum k_i \psi_i(\mathbf{x}, t)$. The features are orthogonal polynomials, and the coefficients $k_i$ are found by a regularization procedure when the model contains more features than data points [10, 15, 45]. Data-driven features have been exploited to optimize the placement of sensors in sparse networks for image and field reconstruction [40].

In the case of the wave equation, the features are $\psi_i(\mathbf{x}, t) = \phi_i(\mathbf{x})h_i(t)$, where $\phi_i$ are eigenfunctions of the weighted Laplace operator, and the temporal features $h_i$ uniquely identify the eigenfunctions. The key result in this framework is that the solution can be fully reconstructed using data on a low-dimensional subspace of the

space-time domain in $\mathbb{R}^d \times \mathbb{R}$, where $d$ is the number of spatial dimensions. We show how to reconstruct the solution of the wave equation from fixed-location sensors by approximating the coefficients $k_i$ from sensor time series data. The eigenfunctions depend on the physical domain and on the wave speed, which may vary by location. For Maxwell's equations, the features are vector fields that can be written in terms of the eigenfunctions of the squared curl operator, weighted by the permittivity, which capture the physics of electromagnetism. The effect of the vectorial nature of Maxwell's equations and fluctuations in properties of the medium have been discussed in [38, 41, 48].

## 2.2 Problem Background

We begin by deriving the solution to the wave equation in terms of eigenfunctions of the weighted Laplace operator $-c^2(\mathbf{x})\Delta$, where $c(\mathbf{x})$ is the spatially-dependent wave speed. We use the wave equation throughout to illustrate the approach. The form of the solution will then be used to reconstruct the wave dynamics from sensor data. In particular, we consider the forced wave equation on an open bounded domain $\mathcal{D}$ in $\mathbb{R}^d$ with initial conditions $f$ and $g$ and homogeneous boundary conditions:

$$(\partial_{tt} - c^2(\mathbf{x})\Delta)u(\mathbf{x},t) = F(\mathbf{x},t), \tag{2.1}$$

$$u(\mathbf{x},0) = f(\mathbf{x}), \tag{2.2}$$

$$u_t(\mathbf{x},0) = g(\mathbf{x}), \tag{2.3}$$

$$u(\mathbf{x},t) = 0, \quad \mathbf{x} \in \partial\mathcal{D}. \tag{2.4}$$

The features $\psi_i$ thus depend upon the properties of the medium. In this chapter, we consider only the case of constant wave speed $c$ for simplicity, but the methodology is the same for spatially variable wave speed $c(\mathbf{x})$. The method of eigenfunction expansion can be used to obtain the solution $u$. We choose the solutions $\{\phi_i\}$ of the

associated eigenvalue problem

$$-\Delta\phi(\mathbf{x}) = \lambda\phi(\mathbf{x}) \tag{2.5}$$

$$\phi(\mathbf{x}) = 0, \quad \mathbf{x} \in \partial\mathcal{D} \tag{2.6}$$

which form an orthonormal basis on $L^2(\mathcal{D})$. In the case of variable wave speed $c = c(\mathbf{x})$, the eigenfunctions of the weighted Laplace operator are used instead. The solution can then be represented as

$$u(\mathbf{x}, t) = \sum_i A_i(t)\phi_i(\mathbf{x}). \tag{2.7}$$

Here and throughout, $i$ and $j$ represent multi-indices corresponding to the eigenfunctions $\{\phi_i\}$. One can solve for the coefficients $A_i(t)$ using the initial conditions and the forcing term. We write the forcing term in the same basis:

$$F(\mathbf{x}, t) = \sum_i \hat{F}_i(t)\phi_i(\mathbf{x}), \qquad \hat{F}_i(t) = \int_{\mathcal{D}} F(\mathbf{x}, t)\phi_i(\mathbf{x})\, d\mathbf{x}. \tag{2.8}$$

By differentiating the solution term by term with respect to time, we obtain the set of ordinary differential equations

$$\frac{d^2 A_i}{dt^2} + c^2\lambda_i A_i = \hat{F}_i(t). \tag{2.9}$$

The initial conditions and orthonormality of $\{\phi_i\}$ yield

$$A_i(0) = \int_{\mathcal{D}} f(\mathbf{x})\phi_i(\mathbf{x})\, d\mathbf{x} = \hat{f}_i \tag{2.10}$$

$$A_i'(0) = \int_{\mathcal{D}} g(\mathbf{x})\phi_i(\mathbf{x})\, d\mathbf{x} = \hat{g}_i. \tag{2.11}$$

By solving these initial value problems for each $A_i$, we obtain the solution to the wave equation:

$$u(\mathbf{x}, t) = \sum_i A_i(t)\phi_i(\mathbf{x}) \tag{2.12}$$

$$A_i(t) = \hat{f}_i \cos\big(c\sqrt{\lambda_i}\, t\big) + \frac{\hat{g}_i}{c\sqrt{\lambda_i}} \sin\big(c\sqrt{\lambda_i}\, t\big) + F_{A_i}(t), \tag{2.13}$$

where

$$F_{A_i}(t) = \int_0^t \frac{\hat{F}_i(\tau)}{c\sqrt{\lambda_i}} \sin\left(c\sqrt{\lambda_i}(t-\tau)\right)\, d\tau. \tag{2.14}$$

The natural frequencies of the problem are $c\sqrt{\lambda_i}$.

## 2.3 Results: Sensor Solutions

We can now investigate the conditions under which the solution (2.12) can be derived from a time series, $B_{\mathbf{s}}(t) = u(\mathbf{s}, t)$, given by a fixed-location sensor located at $\mathbf{s} \in \mathcal{D}$. We assume that the governing equation (i.e., the wave equation (2.1)) and the boundary conditions are known and that the initial conditions of the system are desired. Reconstructing the initial conditions is equivalent in this case to reconstructing the full solution, because the solution is uniquely determined from the initial data. We will show result (1): *time series from a single sensor can be used to fully reconstruct the solution of wave equation for a large class of problems*; however, a single sensor does not suffice in general, and we provide a method for solution reconstruction using multiple sensors. Sensor time series are typically nonperiodic functions characterized by a countable set of frequencies.

The initial conditions can be written in the form

$$f(\mathbf{x}) = \sum_i \hat{f}_i \phi_i(\mathbf{x}) \tag{2.15}$$

$$g(\mathbf{x}) = \sum_i \hat{g}_i \phi_i(\mathbf{x}), \tag{2.16}$$

and we must recover the coefficients $\hat{f}_i$ and $\hat{g}_i$. Because the general solution (2.12) is a sum of terms of the form $\cos(c\sqrt{\lambda_j}\, t)$ and $\sin(c\sqrt{\lambda_j}\, t)$, and using the properties of

orthogonality in spaces of almost periodic functions [7, 24], we consider the constants

$$\alpha_j = \lim_{\tau\to\infty} \frac{1}{\tau} \int_0^\tau B_{\mathbf{s}}(t) \cos\big(c\sqrt{\lambda_j}\, t\big)\, dt \tag{2.17}$$

$$\beta_j = \lim_{\tau\to\infty} \frac{1}{\tau} \int_0^\tau B_{\mathbf{s}}(t) \sin\big(c\sqrt{\lambda_j}\, t\big)\, dt. \tag{2.18}$$

Assuming that the spectrum of the solution is known, we compute

$$\begin{aligned} \alpha_j = \quad & \sum_{i\in I_{\lambda_j}} \phi_i(\mathbf{s}) \frac{\hat{f}_i}{2} \\ & + \underbrace{\lim_{\tau\to\infty} \frac{1}{\tau} \int_0^\tau \sum_i \phi_i(\mathbf{s}) F_{A_i}(t) \cos\big(c\sqrt{\lambda_j}\, t\big)\, dt}_{F_{\alpha_j}} \end{aligned} \tag{2.19}$$

$$\begin{aligned} \beta_j = \quad & \sum_{i\in I_{\lambda_j}} \phi_i(\mathbf{s}) \frac{\hat{g}_i}{2c\sqrt{\lambda_j}} \\ & + \underbrace{\lim_{\tau\to\infty} \frac{1}{\tau} \int_0^\tau \sum_i \phi_i(\mathbf{s}) F_{A_i}(t) \sin\big(c\sqrt{\lambda_j}\, t\big)\, dt}_{F_{\beta_j}}, \end{aligned} \tag{2.20}$$

where $I_{\lambda_j} = \{i : \lambda_i = \lambda_j\}$ is the set of multi-indices that correspond to the same eigenvalue $\lambda_j$, and $F_{A_i}(t)$ is given by Eq. (2.14). The constants $\alpha_j$ and $\beta_j$ are linear combinations of the coefficients $\hat{f}_i$ and $\hat{g}_i$. The spectrum of the solution needed to compute $\alpha_j$ and $\beta_j$ can be obtained by computing the eigenvalues of the operator $\Delta$ on the domain $\mathcal{D}$. The cardinality of $I_{\lambda_j}$ is the multiplicity $m_j$ of $\lambda_j$. In the simplest case, every eigenvalue has multiplicity 1 and the coefficients $\hat{f}_i$ and $\hat{g}_i$ can be recovered directly from Eqs. (2.19) and (2.20).

In the case where $\lambda_j$ has multiplicity $m_j > 1$, we instead use $n = m_j$ sensors placed at spatial locations $\mathbf{s}_1, \ldots, \mathbf{s}_n$. Assuming that the forcing terms $F_{\alpha_j}$ and $F_{\beta_j}$ converge, the coefficients can be obtained by solving a linear system of the form

$$2\begin{pmatrix} \alpha_j^{\mathbf{s}_1} - F_{\alpha_j^{\mathbf{s}_1}} \\ \vdots \\ \alpha_j^{\mathbf{s}_n} - F_{\alpha_j^{\mathbf{s}_n}} \end{pmatrix} = \begin{pmatrix} \phi_{i_1}(\mathbf{s}_1) \dots \phi_{i_{m_j}}(\mathbf{s}_1) \\ \vdots \\ \phi_{i_1}(\mathbf{s}_n) \dots \phi_{i_{m_j}}(\mathbf{s}_n) \end{pmatrix} \begin{pmatrix} \hat{f}_{i_1} \\ \vdots \\ \hat{f}_{i_{m_j}} \end{pmatrix}. \tag{2.21}$$

The above system can be written more succinctly as

$$\alpha_J = \Phi_J \hat{f}_J, \tag{2.22}$$

and one can solve for the coefficients $\hat{f}_J$ if and only if $\Phi_J$ is invertible. The coefficients $\hat{g}_J$ can be obtained with the same matrix $\Phi_J$.

The above analysis places a lower bound on the number of sensors required for reconstruction. If the eigenvalue problem (2.5) has a maximum eigenvalue multiplicity $M$, then the initial conditions $f$ and $g$ cannot be fully determined using fewer than $M$ fixed-location sensors.

As an illustration, consider the case of the rectangular domain $\mathcal{D} = [0, L_x] \times [0, L_y]$. The multiplicity of every eigenvalue is 1 unless the ratio $L_y/L_x$ is rational. If $L_y/L_x = p/q$ for relatively prime integers $p$ and $q$, then the eigenvalues become

$$\lambda_{mn} = \left(\frac{m\pi}{L_x}\right)^2 + \left(\frac{qn\pi}{pL_x}\right)^2 \tag{2.23}$$

and there are distinct multi-indices with the same eigenvalue, such as $(m, n) = (q, p\ell)$ and $(q\ell, p)$ for $\ell = 1, 2, \dots$. Thus, there exist eigenvalues of arbitrarily large multiplicity, which implies that arbitrary initial conditions cannot be derived from finitely many sensors when $L_y/L_x$ is rational. Otherwise, the condition for reconstruction reduces to the requirement that, for each $i$, there be a sensor at $\mathbf{s}_k$ such that $\phi_i(\mathbf{s}_k) \neq 0$.

We now provide a numerical illustration of the effect of the domain shape on the number of sensors required for solution reconstruction. Figure 2.1 shows the results

of a simulation of Eqs. (2.1)–(2.4) on $\mathcal{D}_1 = [\,0, \pi] \times [\,0, 1]$ with the initial conditions

$$f(\mathbf{x}) = \exp\bigl(-30((x - \pi/2 + 0.5)^2 + (y - 0.6)^2)\bigr) \tag{2.24}$$

$$g(\mathbf{x}) = \exp\bigl(-30((x - \pi/2 + 0.8)^2 + (y - 0.3)^2)\bigr) \tag{2.25}$$

and forcing term

$$F(\mathbf{x}, t) = 0.3 \sin(x) \sin(\pi y / L_y) \cos(12t) \tag{2.26}$$

assuming data from a single sensor located at $(1.90, 0.66)$.

The initial conditions (2.24)–(2.25) are first normalized with respect to the $L^2$ norm before each simulation. The forcing term (2.26) is chosen because it represents a simple case of non-resonant forcing (discussed in subsection 2.3.2) and because it is of comparable size to the initial conditions after normalization. We measure the quality of the reconstruction using the relative $L^2(\mathcal{D})$ error in the initial condition as:

$$\left( \frac{\int_{\mathcal{D}} |f_{\text{exact}}(\mathbf{x}) - f_{\text{approx}}(\mathbf{x})|^2 \, d\mathbf{x}}{\int_{\mathcal{D}} |f_{\text{exact}}(\mathbf{x})|^2 \, d\mathbf{x}} \right)^{1/2}. \tag{2.27}$$

Figure 2.1(a) shows a plot of Eq. (2.24), and Figure 2.1(b) shows the reconstruction, whose relative $L^2(\mathcal{D}_1)$ error, Eq. (2.27), is 0.16. (One inherent limitation of this simulation is that it has been done using floating-point arithmetic, which consists of rational numbers.)

Next, we simulate the same problem and initial conditions, except that the domain is now $\mathcal{D}_2 = [\,0, \pi] \times [\,0, \pi]$. Figure 2.2(a) shows a plot of Eq. (2.24), and Fig. 2.2(b)–(d) show the reconstruction using, respectively, one, two, and three sensors located at $(1.90, 2.07)$, $(0.97, 3.02)$, and $(1.68, 2.07)$. In this example, data from at least two sensors are needed to reconstruct the initial condition (2.24) with comparable accuracy to Figure 2.1. The key parameter is the ratio $L_x/L_y$, which is 1 in this example and $\pi$ in the previous one.

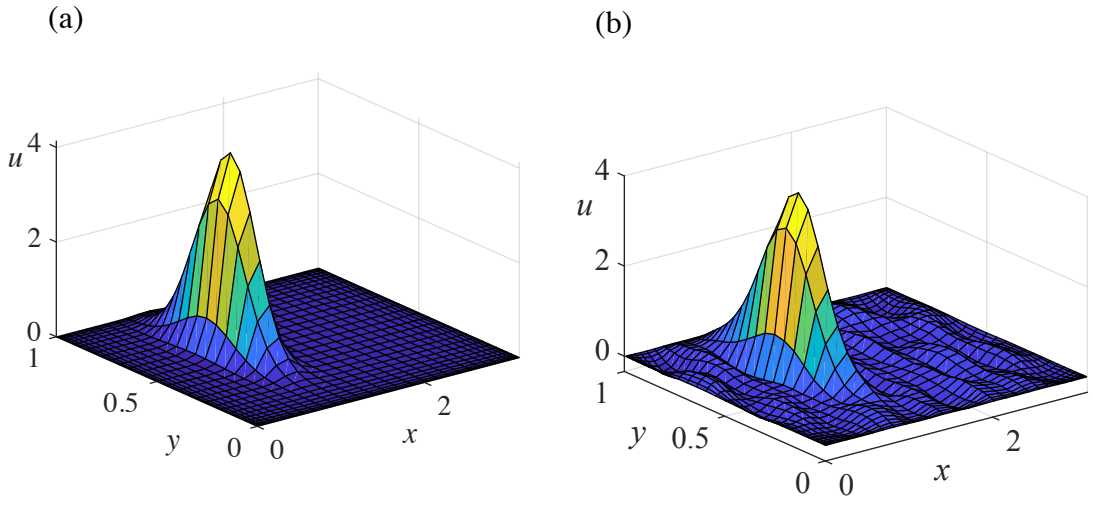


**Figure 2.1:** Reconstruction of the initial condition (2.24) of problem (2.1)–(2.4) with forcing (2.26) on the domain $\mathcal{D} = [\,0, \pi] \times [\,0, 1]$. The initial conditions are given by Eqs. (2.24)–(2.25). (a) The exact initial condition. (b) Reconstruction using one noiseless sensor at $(1.90, 0.66)$. The relative error (2.27) is 0.16. The solution is well approximated using data from one noiseless sensor on a rectangular domain whose length ratio is irrational: $r = L_x/L_y = \pi$.

Finally, we illustrate the first example (domain $\mathcal{D}_1$, Figure 2.1) from a time series perspective. Consider a sensor placed at $\mathbf{s}_1 = (1.90, 0.66)$ and another at $\mathbf{s}_2 = (0.97, 0.96)$. (These locations have been chosen arbitrarily.) The blue curve in Figure 2.3(a) shows the time series of the exact solution at $\mathbf{s}_1$, and the red curve shows the time series of the solution at $\mathbf{s}_1$ as it has been reconstructed from data collected at $\mathbf{s}_2$. Figure 2.3(b) shows the exact solution (blue) at $\mathbf{s}_2$ and its reconstruction (red) at $\mathbf{s}_1$. In both cases, the reconstructed time series follows the exact one closely, but with occasional small errors in amplitude. The results suggest that the wave dynamics allow data from multiple sensors can be cross-checked for accuracy and perhaps incorporated into an error detection and correction scheme.

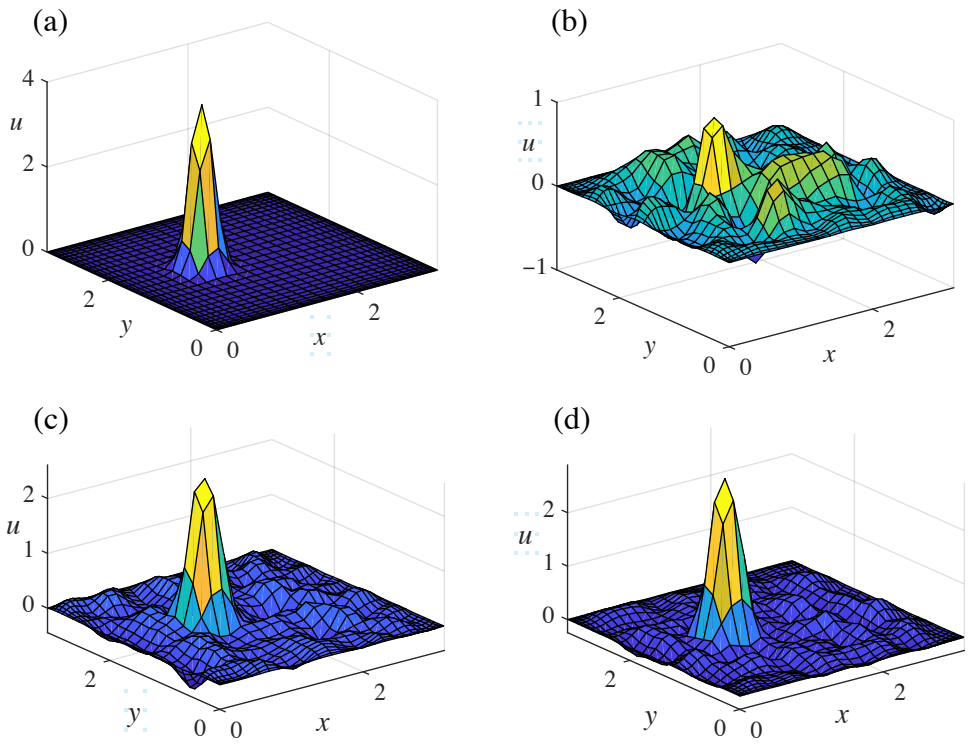


**Figure 2.2:** Reconstructions of the initial condition (2.24) of problem (2.1)–(2.4) with forcing (2.26) on the domain $\mathcal{D} = [0, \pi] \times [0, \pi]$. The initial conditions are given by Eqs. (2.24)–(2.25). (a) The exact initial condition. Reconstruction using (b) one sensor, (c) two sensors, and (d) three sensors at representative locations using the least squares solution from Eq. (2.51). The relative errors (2.27) are (b) 0.89, (c) 0.41, and (d) 0.33. The solution is poorly approximated using data from one sensor, even in the absence of noise, on a domain with a rational ratio of domain lengths: $r = L_x/L_y = 1$.

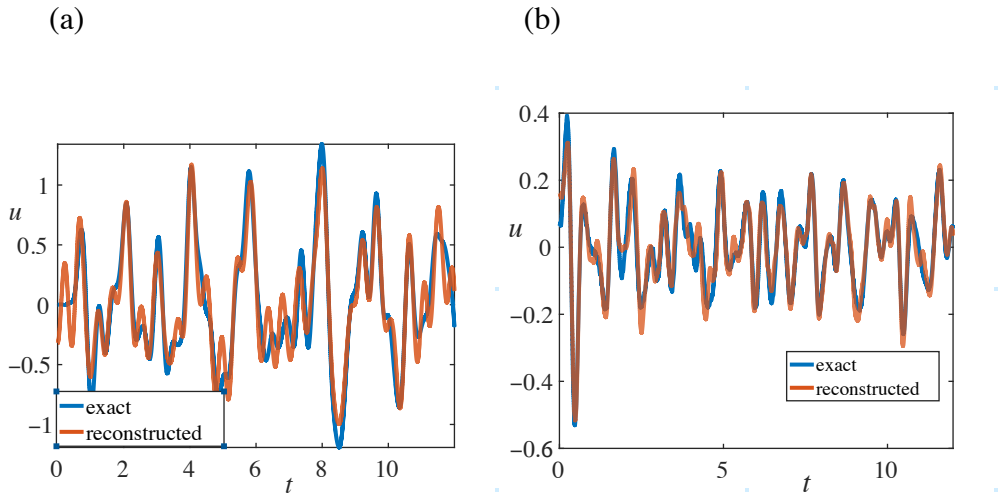


**Figure 2.3:** Time series reconstructions using one sensor of the problem (2.1)–(2.4) as in Figure 2.1. Sensors are placed at two representative locations: $\mathbf{s}_1 = (1.90, 0.66)$ and $\mathbf{s}_2 = (0.97, 0.96)$. (a) Blue curve: the time series of the "exact" solution at $\mathbf{s}_1$. Red curve: the time series of the reconstructed solution at $\mathbf{s}_1$ using the sensor at $\mathbf{s}_2$. (b) Blue curve: the "exact" time series at $\mathbf{s}_2$. Red curve: the time series of the reconstructed solution at $\mathbf{s}_2$ using the sensor at $\mathbf{s}_1$.

### *2.3.1 Reconstruction Errors with Respect to Sensor Position*

An interesting question concerns the relationship between sensor position and the error in the reconstruction of the initial condition (which, as mentioned above, is equivalent in this problem to reconstructing the entire solution). The initial condition (2.24) has a unique maximum at $\mathbf{x}_0 = ((\pi - 1)/2, 0.6)$. Figure 2.4(a) shows the $L^2$ relative error (as defined by (2.27)) as a function of distance from $\mathbf{x}_0$ on the domain $\mathcal{D}_1$; Figure 2.4(c) is the same, except on the domain $\mathcal{D}_2$. No simple functional relationship is apparent. Panels (b) and (d) show the $L^2$ relative error on $\mathcal{D}_1$ and $\mathcal{D}_2$, respectively, as a function of sensor position; the point $\mathbf{x}_0$ is shown as a red dot. Here a spatial structure is evident in the relative $L^2$ reconstruction error. If a sensor is located near a node (i.e., a zero point) of an eigenfunction $\phi_i$, then small errors in approximation, which are inevitable in floating-point arithmetic, dominate the reconstruction error.

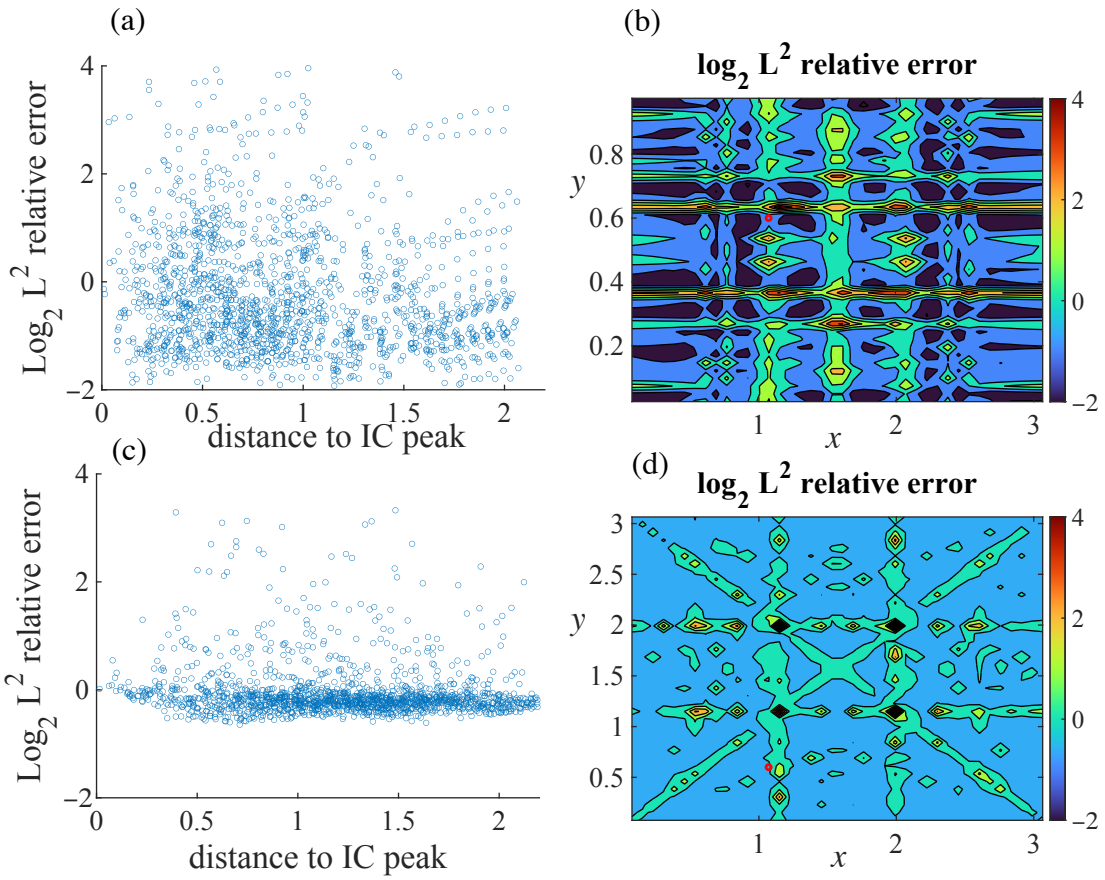


**Figure 2.4:** Relative reconstruction error (2.27) against the distance from the sensor to the peak of the initial condition. The problem simulated is as in Figure 2.1 for (a)–(b) and as in Figure 2.2 for (c)–(d) with the color axis on (b) and (d) and the y axis on (a) and (c) capped at 4. Panels (a) and (c) show that the two quantities are not clearly correlated. In panels (a)–(b) reconstructions from sensors in about 27.3% of locations had an $L^2(\mathcal{D})$ relative error below 1; no locations had $L^2$ errors less than in panels (c)–(d). Panels (b) and (d) display the error against the location of the sensor; the red circle indicates the location of the initial peak.

The nodes depend on the domain as well as the (weighted) Laplace operator, and their structure, together with the frequencies of greatest interest, can be used to determine a suitable arrangement of sensors. In these examples, a circular array of sensors may be an effective way to reduce the reconstruction error, because the sensors will not all lie near a node. Another strategy would be to place the sensors randomly throughout the domain.

### *2.3.2 Remarks on Convergence*

We now investigate the circumstances under which $F_{\alpha_j}$ and $F_{\beta_j}$ converge (cf. Eqs. (2.19)–(2.20)). Suppose that the forcing term is time periodic:

$$F(\mathbf{x},t) = \overline{F}(\mathbf{x})\cos(\omega t) = \sum_i \hat{F}_i(t)\phi_i(\mathbf{x}) \tag{2.28}$$

where

$$\hat{F}_i(t) = \int_{\mathcal{D}} \overline{F}(\mathbf{x})\phi_i(\mathbf{x})\,d\mathbf{x}\cos(\omega t). \tag{2.29}$$

We make the additional assumption that $\omega \neq c\sqrt{\lambda_i}$ for any multi-index $i$ to avoid resonant frequencies. Using the relation

$$\int_0^t \cos(\omega s)\sin\big(c\sqrt{\lambda_i}\,(t-s)\big)\,ds = \frac{c\sqrt{\lambda_i}\,\big(\cos(c\sqrt{\lambda_i}\,t) - \cos(\omega t)\big)}{\omega^2 - c^2\lambda_i} \tag{2.30}$$

and substituting the definitions of $F_{A_i}$ and $\hat{F}_i$ from Eqs. (2.14) and (2.8) into $F_{\alpha_j}$, we obtain

$$\begin{aligned} F_{\alpha_j} &= \sum_i \phi_i(\mathbf{s}) \frac{\int_{\mathcal{D}} \overline{F}(\mathbf{x})\phi_i(\mathbf{x})d\mathbf{x}}{\omega^2 - c^2\lambda_i} \\ &\qquad \times \lim_{\tau\to\infty} \frac{1}{\tau}\int_0^\tau \big(\cos(c\sqrt{\lambda_i}\,t) - \cos(\omega t)\big)\cos(c\sqrt{\lambda_j}\,t)\,dt \\ &= \sum_{i\in I_{\lambda_j}} \frac{1}{2}\phi_i(\mathbf{s}) \cdot \frac{\int_{\mathcal{D}} \overline{F}(\mathbf{x})\phi_i(\mathbf{x})d\mathbf{x}}{\omega^2 - c^2\lambda_i}. \end{aligned} \tag{2.31}$$

Thus $F_{\alpha_j}$ converges. The forcing can be further generalized to a finite sum of the form

$$F(\mathbf{x},t) = \sum_{k=1}^{n} \overline{F}_k(\mathbf{x}) \cos(\omega_k t), \tag{2.32}$$

when each $\omega_k$ is not a natural frequency $c\sqrt{\lambda_i}$.

### *2.3.3 Remarks on Small Damping*

In the more general case where the wave equation includes damping, Eq. (2.1) becomes

$$(\partial_{tt} + \gamma\partial_t - c^2(\mathbf{x})\Delta)u(\mathbf{x},t) = F(\mathbf{x},t) \tag{2.33}$$

where $\gamma > 0$ is the damping parameter. If the damping is sufficiently small, i.e., $\gamma < 2c\sqrt{\lambda_i}$ for all $i$, then the solution is again of the form (2.12) with

$$A_i(t) = e^{-\gamma t/2}\left(\hat{f}_i \cos(\omega_i t) + \frac{1}{\omega_i}\left[\frac{\gamma}{2}\hat{f}_i + \hat{g}_i\right]\sin(\omega_i t)\right) \tag{2.34}$$

where $\omega_i = \sqrt{c^2\lambda_i - (\gamma/2)^2}$. Therefore, if $\gamma$ is sufficiently small, then the eigenvalue perturbations are small, and the analysis becomes a regular perturbation problem; approximating $\gamma$ will result in only a small error. We can apply the transformation

$$\tilde{B}_{\mathbf{s}}(t) = e^{\gamma t/2} B_{\mathbf{s}}(t) \tag{2.35}$$

and the same analysis as above to $\tilde{B}_{\mathbf{s}}$ with perturbed eigenvalues to obtain the coefficients $\hat{f}_i$ and $\hat{g}_i$. (An analogous mathematical development has been presented in [19, 46] to analyze plasmonic dynamics in the presence of damping.) The assumption $\gamma < 2c\sqrt{\lambda_i}$ for all $i$ is essential to applying this method of reconstruction. If the damping coefficient is above this threshold, then the damping dominates the wave dynamics, making this problem similar to the heat equation, where reconstruction of initial conditions from future data is an ill-posed problem.

### 2.3.4 Sensor Placement Sensitivity

The discussion so far shows that, in many cases, a single sensor does not suffice to reconstruct the solution. We now discuss result (2): *solution reconstructions from an individual sensor are sensitive to perturbations in sensor placement.* Consider the case of the interval domain $\mathcal{D} = [\,0, L_x]$. The solutions of the eigenvalue problem (2.5) are

$$\lambda_n = \left(\frac{n\pi}{L_x}\right)^2 \tag{2.36}$$

$$\phi_n(x) = \left(\frac{2}{L_x}\right)^{1/2} \sin\left(\frac{n\pi x}{L_x}\right). \tag{2.37}$$

As discussed above, the coefficients of $f$ and $g$ can be determined from a single sensor if and only if $\phi_n(\mathbf{s}) \neq 0$ for all $n$. The zeros of the eigenfunction $\phi_n$ are $x = (j/n)L_x$, $j = 0, 1, \ldots, n$. Therefore, $f$ and $g$ can be determined from a single sensor located at $\mathbf{s}$ provided that $\mathbf{s}$ is not in the dense subset $B = L_x(\mathbb{Q}) \cap \mathcal{D}$ of the domain, where $L_x(\mathbb{Q})$ is the set of rational multiples of $L_x$. Informally, we can regard $B$ as the set of "bad" locations for sensor placement.

Even though a solution can be reconstructed from a sensor located at $\mathbf{s}_0 \notin B$, for every $\epsilon > 0$ there are infinitely many other locations $\mathbf{s}$ in an $\epsilon$ neighborhood of $\mathbf{s}_0$ from which a sensor at $\mathbf{s}$ cannot be used to reconstruct the solution. Although $B$ has Lebesgue measure zero, the placement of the sensor is sensitive. Furthermore, this result can be extended to $d$ dimensions by considering the zeros of the eigenfunctions $\phi_i$ in the domain $\mathcal{D} = \prod_{k=1}^{d}[\,0, L_k]$.

### 2.3.5 Truncation Error and Bounded Frequency Range

The above discussion shows that it is not practical to recover all possible frequencies from a given set of sensors: the relevant eigenvalues may have arbitrarily large

multiplicity, and arbitrarily small perturbations in sensor location can result in unrecoverable frequencies. In practice, however, one is interested only in frequencies in some bounded range $[\omega_{\min}, \omega_{\max}]$; that is, the solution has either a bounded spatial frequency or a bounded temporal frequency. In the case of (2.5) with a $d$-dimensional rectangular domain $\mathcal{D}$, the bounded frequency range yields only finitely many eigenfunctions and eigenvalues, and the solution (2.12) reduces to a finite sum. Hence there is a maximum multiplicity $M$ of the set of relevant eigenvalues, and the set $B$ of bad sensor locations is no longer dense. However, $B$ may still contain many points, because an eigenfunction $\phi_n$ has $n-1$ zeros on the interior of the domain in the one dimensional case and infinitely many zeros in higher dimensions. Sensor placement strategies should avoid locations $\mathbf{s}$ where $\phi_n(\mathbf{s})$ is close to 0.

In the previous sections, the full series expansion of the solution to the wave equation is used, which involves infinitely many terms. In the simulations, the solution series expansion is truncated. We now discuss the error induced by this truncation. If the initial conditions $f$ and $g$ are in $L^2(\mathcal{D})$, then by the Parseval's identity, the sequences $(\hat{f}_j)$ and $(\hat{g}_j)$ are in $\ell^2$, i.e.,

$$\sum_j |\hat{f}_j|^2 < \infty, \qquad \sum_j |\hat{g}_j|^2 < \infty \tag{2.38}$$

and so we are guaranteed that the truncation error tends to 0. The existence of a solution is guaranteed if $f \in H_0^1(\mathcal{D})$. If the initial conditions are in a Gevrey class, then the Fourier coefficients tend to 0 exponentially fast. In fact, for any initial conditions in a Gevrey class, the solution is guaranteed to belong to that Gevrey class for all $t > 0$ [28].

### 2.3.6 Analytical Estimate of Reconstruction Error

So far, we have assumed that parameters of the problem (2.1) are known exactly and that sensors can observe for arbitrarily long times. Now suppose that the sensors can observe only for a finite time $\tau$, and that the lengths of the sides of the rectangular domain are $\widetilde{L}_i$ instead of $L_i$. The actual eigenvalues are $\widetilde{\lambda}_i$ instead of $\lambda_i$. Assuming that $|\widetilde{L}_i - L_i|$ is sufficiently small so that $\widetilde{\lambda}_i \neq \lambda_j$ for $i \neq j$, then

$$\lim_{\tau\to\infty} \frac{1}{\tau} \int_0^\tau \cos\left(c\sqrt{\lambda_i}\, t\right) \cos\left(c\sqrt{\widetilde{\lambda}_i}\, t\right)\, dt = 0, \tag{2.39}$$

which implies that $\alpha_i = 0$ for all $i$, and the solution cannot be reconstructed from an infinite time series of sensor data using the relations in Eqs. (2.17)–(2.20). Instead, let us consider the functions

$$\alpha_i(\tau) = \frac{1}{\tau} \int_0^\tau B_{\mathbf{s}}(t) \cos\left(c\sqrt{\widetilde{\lambda}_i}\, t\right)\, dt \tag{2.40}$$

$$\beta_i(\tau) = \frac{1}{\tau} \int_0^\tau B_{\mathbf{s}}(t) \sin\left(c\sqrt{\widetilde{\lambda}_i}\, t\right)\, dt \tag{2.41}$$

and choose $\tau$ to be $p$ complete periods of the frequency $c\widetilde{\lambda}_i^{1/2}$ for each $i$, i.e., $\tau = p(2\pi)/c\widetilde{\lambda}_i^{1/2}$. If the frequency range of interest is $[\omega_{\min}, \omega_{\max}]$, then the observed sensor time series may be written as the finite sum

$$B_{\mathbf{s}}(t) = \sum_{i\in\Lambda} A_i(t)\phi_i(\mathbf{s}), \tag{2.42}$$

where $\Lambda$ is the set of relevant eigenfunction indices and $A_i(t)$ is defined by (2.13).

The difference in the approximate Fourier coefficient $\widetilde{f}_i$ and the "exact" one $\hat{f}_i$ is determined from the relation

$$\frac{2}{\phi_i(\mathbf{s})}\alpha_i(\tau) - \hat{f}_i = (2\hat{f}_i E_{ii} - \hat{f}_i) + \sum_{j\in\Lambda, i\neq j} 2\frac{\phi_j(\mathbf{s})}{\phi_i(\mathbf{s})}\hat{f}_j E_{ij}. \tag{2.43}$$

where $E_{ij}$ and $E_{ii}$ are given by Eqs. (2.45)–(2.46), below. The difference between the approximate ($\tilde{u}$) and exact ($u$) reconstructed time series at the point $\mathbf{x}_0$ is

$$\tilde{u}(\mathbf{x}_0,t) - u(\mathbf{x_0},t) = \sum_{i\in\Lambda}\Big[\frac{2}{\tilde{\phi}_i(\mathbf{s})}\alpha_i(\tau)\tilde{\phi}_i(\mathbf{x}_0)\cos\left(c\sqrt{\widetilde{\lambda}_i}\,t\right) - \hat{f}_i\phi_i(\mathbf{x}_0)\cos\left(c\sqrt{\lambda_i}\,t\right)\Big]. \tag{2.44}$$

For further analysis, we consider the rectangular domain $\mathcal{D} = [\,0, L_1] \times [\,0, L_2]$. Let $\rho_k = \widetilde{L}_k/L_k$, $k = 1, 2$ and let $i$ be the multi-index $i = (m_i, n_i)$. We interchange the order of integration and (finite) summation in $\alpha_j(\tau)$ and $\beta_j(\tau)$ and expand each term in the sum as a Taylor series in $(\rho_1, \rho_2)$ about $(1, 1)$ to obtain

$$\begin{aligned} E_{ij} = \frac{1}{\tau}\int_0^\tau \cos\left(c\sqrt{\widetilde{\lambda}_i}\,t\right)\cos\left(c\sqrt{\lambda_j}\,t\right)\,dt = \\ \frac{-\sqrt{\lambda_i\lambda_j}}{p\pi(\lambda_i-\lambda_j)}\sin\left(\pi p\sqrt{\frac{\lambda_j}{\lambda_i}}\right)\cos\left(\pi p\sqrt{\frac{\lambda_j}{\lambda_i}}\right) \\ +\mathcal{O}\left(\frac{\widetilde{L}_1-L_1}{L_1}\right)+\mathcal{O}\left(\frac{\widetilde{L}_2-L_2}{L_2}\right) \end{aligned} \tag{2.45}$$

when $i \neq j$ and

$$\begin{aligned} E_{ii} = \frac{1}{\tau}\int_0^\tau \cos\left(c\sqrt{\widetilde{\lambda}_i}\,t\right)\cos\left(c\sqrt{\lambda_i}\,t\right)\,dt = \\ \frac{1}{2}+\frac{n_1^2L_2^2}{4(m_1^2L_1^2+n_1^2L_2^2)}\cdot\frac{\widetilde{L}_1-L_1}{L_1} \\ +\frac{m_1^2L_1^2}{4(m_1^2L_1^2+n_1^2L_2^2)}\cdot\frac{\widetilde{L}_2-L_2}{L_2}+H.O.T. \end{aligned} \tag{2.46}$$

when $i = j$. (Here H.O.T. stands for higher-order terms.) This elementary calculation shows that the reconstruction error approaches 0 only if $p \to \infty$, $\widetilde{L}_1 \to L_1$ and $\widetilde{L}_2 \to L_2$. To first order, the difference between the "true" and computed Fourier coefficient for each $i$ is proportional to the relative errors in the dimensions of the domain and inversely proportional to the observing time:

$$\tilde{f}_i - \hat{f}_i = \mathcal{O}\left(\frac{1}{p}\right)+\mathcal{O}\left(\frac{\widetilde{L}_1-L_1}{L_1}\right)+\mathcal{O}\left(\frac{\widetilde{L}_2-L_2}{L_2}\right). \tag{2.47}$$

Higher-order Taylor series terms become too large to display and interpret.

### 2.3.7 Error Decay Rate

Suppose we have a network of $n$ noisy sensors at locations $\mathbf{s}_1, \ldots, \mathbf{s}_n$. We now derive result (3): *If the time series from each sensor is contaminated with Gaussian noise, then the error in the reconstructed solution decreases as* $\mathcal{O}(n^{-1/2})$. Suppose that the time series from the $k$th sensor is $B_k(t) = \mu_k(t) + \epsilon_k(t)$, where $\mu_k(t) = u(\mathbf{s}_k, t)$ is the "true" signal and $\epsilon_k(t)$ is Gaussian white noise. The series coefficients, $\alpha_j^k$, for the $k$th sensor are given by (cf. Eqs. (2.17)–(2.20))

$$\alpha_j^k = \sum_{i \in I_{\lambda_j}} \phi_i(\mathbf{s}_k) \frac{\hat{f}_i}{2} + F_{\alpha_j^k} + \underbrace{\lim_{\tau \to \infty} \frac{1}{\tau} \int_0^\tau \epsilon_k(t) \cos\bigl(c\sqrt{\lambda_j}\, t\bigr)\, dt}_{\epsilon_j^k}, \tag{2.48}$$

which for $n$ sensors yields the linear system

$$2 \begin{pmatrix} \alpha_j^1 - F_{\alpha_j^1} - \epsilon_j^1 \\ \vdots \\ \alpha_j^n - F_{\alpha_j^n} - \epsilon_j^n \end{pmatrix} = \begin{pmatrix} \phi_{i_1}(\mathbf{s}_1) \cdots \phi_{i_{m_j}}(\mathbf{s}_1) \\ \vdots \\ \phi_{i_1}(\mathbf{s}_n) \cdots \phi_{i_{m_j}}(\mathbf{s}_n) \end{pmatrix} \begin{pmatrix} \hat{f}_{i_1} \\ \vdots \\ \hat{f}_{i_{m_j}} \end{pmatrix}, \tag{2.49}$$

where $m_j$ is the multiplicity of the eigenvalue $\lambda_j$. (We assume throughout that the number of sensors, $n$, is at least as large as the largest multiplicity of any relevant eigenvalue.) The system (2.49) may be written more succinctly as

$$\tilde{\alpha}_J = \Phi_J \hat{f}_J \quad \text{where} \quad \tilde{\alpha}_J = \alpha_J - 2\epsilon_J. \tag{2.50}$$

In practice, each sensor time series is discrete and finite, as are the sampled noise terms. We assume that $\epsilon_J$ is distributed as $N_n(0, \sigma^2 I)$ for some $\sigma > 0$. The system (2.49) is overdetermined when $n > m_j$; standard least-squares theory implies that the best linear unbiased estimate $\widetilde{f}_J$ of $f_J$ and its associated variance are, re-

spectively,

$$\widetilde{f}_J = (\Phi_J^T \Phi_J)^{-1} \Phi_J^T \widetilde{\alpha}_J \tag{2.51}$$

$$\sigma_J^2 = E[(\widetilde{f}_J - f_J)(\widetilde{f}_J - f_J)^T \mid \Phi_J] = (\Phi_J^T \Phi_J)^{-1} \sigma^2. \tag{2.52}$$

We illustrate the case of approximating Fourier coefficients from $n$ sensors with normal data. If the sensor data $[\phi_{i_1}(\mathbf{s}_k) \cdots \phi_{i_{m_j}}(\mathbf{s}_k)]$ are distributed as $\mathcal{N}(0, \Sigma)$, then

$$(\Phi_J^T \Phi_J)^{-1} \sim \mathcal{W}_{m_j}^{-1}(\Sigma^{-1}, n) \tag{2.53}$$

where $\mathcal{W}^{-1}$ denotes the inverse Wishart distribution, and the law of iterated expectation implies that the covariance of the estimator is

$$E\big[E[(\widetilde{f}_J - f_J)(\widetilde{f}_J - f_J)^T \mid \Phi_J]\big] = \frac{\Sigma^{-1}\sigma^2}{n - m_j - 1}, \tag{2.54}$$

which is $\mathcal{O}(n^{-1})$.

As a numerical illustration, we repeat the simulation discussed in the first example (cf. Figure 2.1) with the initial condition (2.24). The first, second, and third sensors are located at $(1.90, 0.66)$, $(0.97, 0.96)$, and $(1.68, 0.66)$, and $\tau$ is chosen such that $\omega_{\min}\tau = 500$ are used for reconstruction

$$\tilde{B}_{\mathbf{s}_k}(t) = B_{\mathbf{s}_k}(t) + \epsilon_k(t), \quad k = 1, \ldots, n \tag{2.55}$$

on the domain $\mathcal{D} = [\,0, \pi] \times [\,0, 1]$. The Gaussian noise is $\epsilon_k(t) \sim \mathcal{N}(0, 2.0^2)$ where $\epsilon_k(s)$ and $\epsilon_\ell(t)$ are independent if $k \neq \ell$ or $s \neq t$ and $B_{\mathbf{s}_k}(t)$ is the noiseless time series. Figure 2.1(a) shows the exact initial condition (2.24), and 2.1(b) shows its reconstruction using one noiseless sensor. Figures 2.5(a)–(b) show the effect of the noise using one and three noisy sensors, respectively, using Eq. (2.51). The panels in Figure 2.6 show time series reconstructions at representative locations in the domain with one and five noisy sensors, respectively. Linear regression on the numerical data

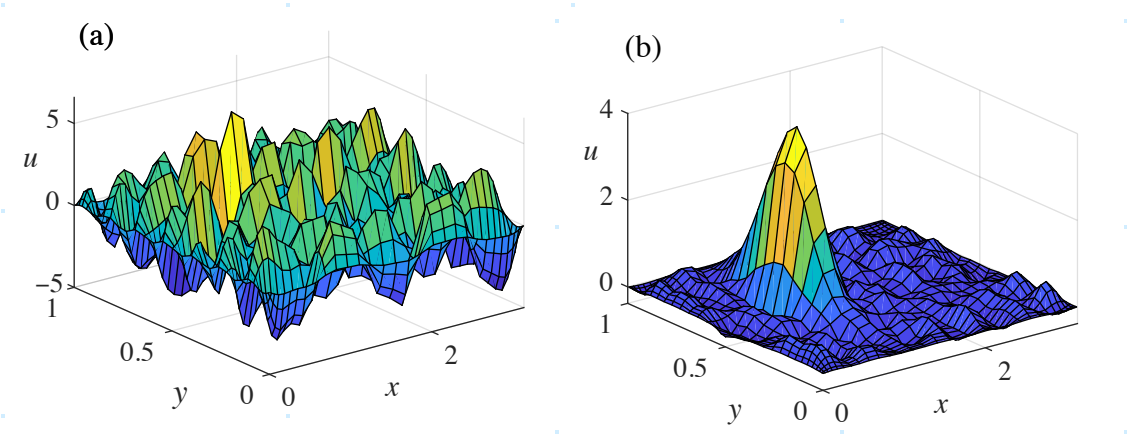


**Figure 2.5:** Reconstructions of the initial condition, Eq. (2.24), on the domain $\mathcal{D} = [0, \pi] \times [0, 1]$ as in Figure 2.1. (a) The effect of Gaussian noise $\epsilon(t) \sim \mathcal{N}(0, 2.0^2)$ as in Eq. (2.55) on the reconstruction using one noisy sensor and (b) three noisy sensors using the least squares solution from Eq. (2.51). The relative errors (2.27) are (a) 2.90 and (b) 0.25. In the presence of noise, the solution can be well approximated only with time series from multiple sensors.

shows that the relative error in the $L^2(\mathcal{D})$ norm of the initial condition decreases as $\mathcal{O}(n^{-0.4963})$ for $n$ sensors, in good agreement with the theory, as shown in Figure 2.7.

In Figure 2.8(a), the $L^2(\mathcal{D})$ reconstruction error increases roughly linearly with the noise level $\sigma$. The error using one sensor is approximately 10 times higher than with 10 sensors and relative reconstruction error stays below 1.0 using 10 sensors for noise as high as $\sigma = 10$. In Figure 2.8(b), the error decreases sharply with an increasing number of periods $p = \tau\omega_{\min}$ of each frequency used in reconstruction.

When the eigenfunctions are sines and cosines, the Nyquist sampling theorem provides necessary conditions under which Fourier coefficients can be estimated from time series data: the sampling rate must be at least twice as fast as the highest relevant frequency. Analogous criteria are expected to apply for more general eigenfunctions, but we do not consider this question in further detail here.

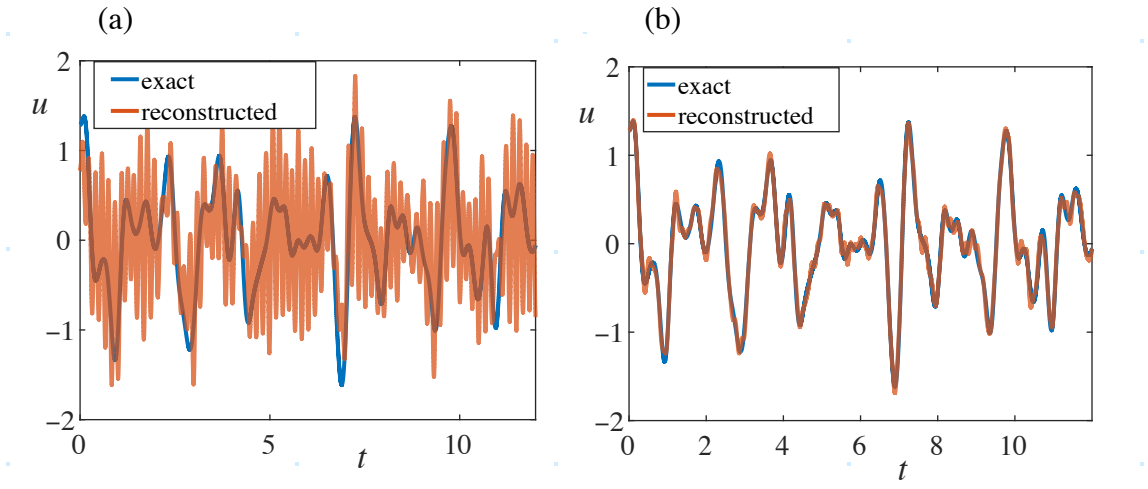


**Figure 2.6:** Reconstruction of wave equation time series (at a randomly chosen spatial location) from noisy sensors using (a) one sensor and (b) five sensors, where the noise in each sensor is $\epsilon(t) \sim \mathcal{N}(0, 2.0^2)$ as in Eq. (2.55). The solution is poorly approximated using data from one sensor. Time series from additional sensors significantly improve the accuracy of reconstruction.

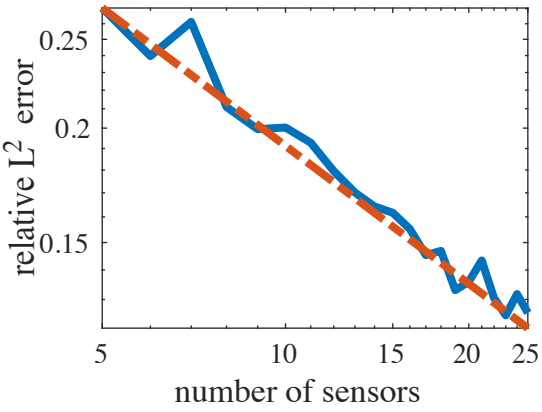


**Figure 2.7:** The blue curve shows the relative error (2.27), as a function of the number of randomly placed sensors $n$ on a log-log scale, in the domain $\mathcal{D} = [0, \pi] \times [0, 1]$. The red dashed line has a slope of $-0.5$, which is the theoretically predicted value.

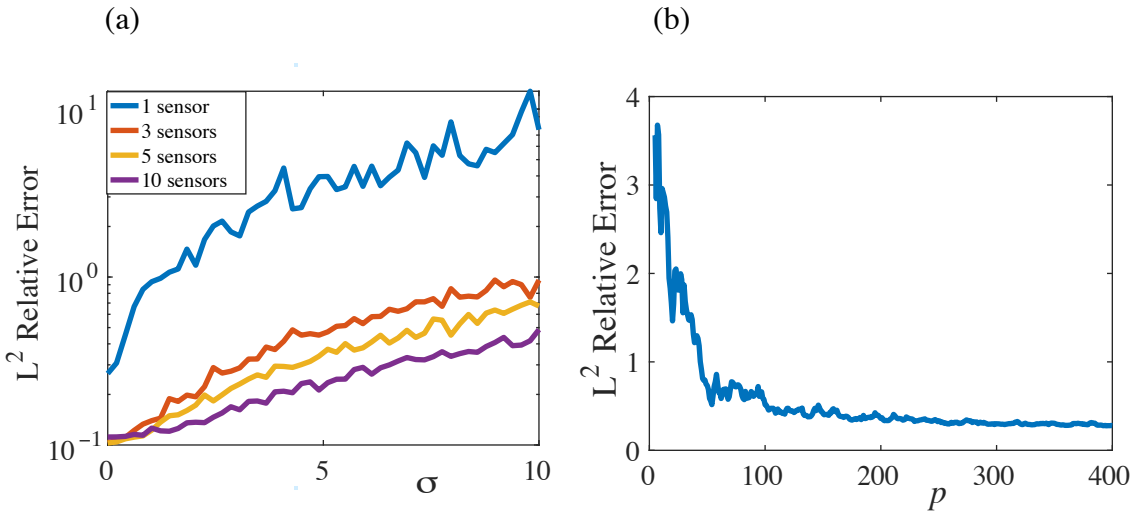


**Figure 2.8:** The relative error (2.27) with respect to (a) noise level $\sigma$ and (b) as a function of the nondimensional parameter $p = \omega_{\min}\tau$ where $\tau$ is observing time interval used in equation (2.40) for the problem (2.1)–(2.4) as in Figure 2.1. Reconstruction is obtained via Eq. (2.51).

## 2.4 Discussion and Future Work

We have explored many possibilities for full reconstruction of wave phenomena from fixed-location sensors and shown that a large class of problems are reconstructible from a single sensor, although the results are sensitive to the location of the sensor in many cases. Multiple sensors provide more robust results. Often, only a few sensors are needed for high-quality reconstructions: in the case of a square domain (as in Figure 2.2) and the case of noisy sensor data (in Figure 2.1), three to five sensors provide satisfactory results. The nodes of the eigenfunctions should be taken into account in placement strategies for sensor networks. Our approach can be extended to vectorial sensors for electric and magnetic fields using Maxwell's equations and to non-rectangular domains. In future work, we will consider this extension as well as the effect of small nonlinearities.

Acknowledgments: This work was partially supported by the Air Force Office of

Scientific Research under award number FA9550-19-1-0064. The work described in this chapter is published [5].

Chapter 3

# OPTIMAL OBSERVATION TIME FOR SOLUTIONS TO THE STOCHASTIC MAXWELL VECTOR WAVE EQUATION

## 3.1 Introduction

There has been a long history in applied dynamics of using time series embedding methods to reconstruct a representation of the chaotic attractor of a dissipative process, from which dynamical quantities like dimension and Lyapunov exponents can be estimated, even in cases where the governing equations are not known exactly [1, 33]. Some recent efforts have focused on identifying the governing equations from time series data including the high noise regime [39, 30, 14].

In this dissertation, we take a different point of view: suppose that we know the dynamical equations (e.g., from physical laws) and are given a time series of measurements from a sensor at a fixed location in space. How can we exploit the dynamics governed by physical laws to analyze the signal? If noise is present, then how long should measurements be taken to estimate dynamical parameters of interest, and how accurate are the estimates? Can measurements at one location predict what would be observed at another location?

Our focus here is on the Maxwell vector wave equation, where the electric field is driven by a stochastic current density whose variance increases in time. One important example of such a phenomenon is in the ionospheric electron layers (the Karman D/E/F layers) around sunrise, when increasing solar radiation excites growing noisy electric currents in the ionized environment [4, 16, 34]. (Near-earth satellites orbit in the ionosphere, and so-called space weather affects their operations.) In such a case,

we might know something about the current density, such as the average current or the level of noise. In this chapter, we consider the problem of taking measurements at a particular point for a limited interval of time and ask what information about the electric field can be obtained from the observations. To be successful, of course, the problem must be well posed. Indeed, in diffusive processes such as the heat equation or the wave equation with a large damping coefficient, the dissipation leads to an irreversible loss of information. We thus provide a detailed analysis of this problem for a general class of wave-like processes without damping, of which the Maxwell vector wave equation is our primary example.

The Maxwell vector wave equation admits a formal solution consisting of a linear combination of eigenfunctions with time-dependent coefficients. From general PDE theory, any time series of the electric field obtained at a given location in space is an almost periodic function. In a given application, one is interested only in a bounded range of frequencies within the electromagnetic spectrum (bandlimited signals), and the dominant frequencies and corresponding eigenfunctions are finite in number. Now consider a time series of measurements of the electric field at a fixed location in space. One goal is to determine the time-dependent coefficients of the eigenfunctions from the data. (In the simplest case, the eigenfunctions are sines and cosines, and the coefficients can be obtained from a Fourier transform of the time series.) Then, since the solution ansatz yields the dynamics at every point, sensor measurements at one location can be used to predict the measurements at another location. In other words, local data yields global information; we refer to this process as "reconstructing" the electric field from the data [5]. This result also implies that the dynamics can be exploited to provide the theoretical basis for an error detection and correction scheme for a network of sensors.

Another goal, since the time series is noisy, is to estimate the mean squared error

in the coefficients computed from the data and, therefore, to quantify the quality of the global reconstruction of the electric field. We show that the mean squared error can be decomposed as

$$\mathrm{MSE}(\tau) = [\mathrm{BIAS}(\tau)]^2 + \mathrm{VAR}(\tau) \sim [A/\tau]^2 + B\tau, \tag{3.1}$$

where $\tau$ is the duration of the sensor time series. Because the bias decreases with time, but the variance increases with time, there is an "optimal" observing time that minimizes the overall error. This so-called bias-variance tradeoff has been studied in the context of signal processing [49], but our analysis traces its origin directly back to Maxwell's equations and the stochastic current density.

Our approach is general insofar as it does not require a homogeneous medium or particular boundary conditions, as long as the eigenfunctions are orthogonal in an appropriate sense (described in the next section). We also emphasize that we are not considering an equilibrium system in which added energy is dissipated.

To our knowledge, our results are new to the field of dynamical time series analysis in the following ways. First, we consider vectorial time series and vectorial solutions to a hyperbolic partial differential equation. Second, if we know the dynamical equations from physical or other considerations, then in some cases we can exploit the dynamics to obtain global information from local data. Finally, we show that a bias-variance tradeoff exists when the dynamics are driven by a stochastic, variance-increasing process. The focus of our investigation is on time series measurements taken at a fixed spatial location; the question of how to handle a moving sensor will be addressed in the next chapter.

This chapter is organized as follows. In section 3.2, we formally introduce our problem and derive the solution to the stochastic Maxwell vector wave equation; in section 3.3, we analyze the behavior of this solution. The main results on optimal ob-

servation time are presented in section 3.4, where we derive a closed-form expression for the MSE (3.1) in terms of bias and variance showing that the MSE can be minimized. In section 3.5, we present an algorithm to minimize the MSE using optimal observation times and the use of the algorithm is illustrated with an example reconstruction. Finally, in concluding remarks, we mention an application of our results for sensor networks in section 3.6.

## 3.2 Problem Setup

Using sensor data to detect and reconstruct vectorial electromagnetic waves propagating in an inhomogeneous medium is an important physical problem with many applications. Data assimilation techniques have been developed to incorporate sensor data in modeling the ionosphere [16, 34] and techniques have been developed to account for ionospheric inhomogeneities in synthetic aperture imaging [25]. In [32], Kak et al. found sensor placement conditions to optimize CubeSat sensor networks. Often, sensor data is noisy and careful treatment is required to obtain the noiseless signal. Dating back to classical work [51], noise in physical problems has been treated rigorously in terms of stochastic processes. More recently, stochastic noise has been extended to PDEs via Hilbert space theory [13, 21]. In particular, stochastic wave-like phenomena have been studied in the context of the oscillator ODE [27, 26, 50]. Stochastic processes can appear additively or multiplicatively in these differential equations, meaning that either the source term, the frequency, or the damping term is stochastic. Maxwell's equations have been studied under the assumption of stochastic current density [22, 36] or stochastic electric permittivity [31]. Inverse source problems for stochastic wave equations have been an active area of research [20]. In these problems, properties of the source of the noise are determined from final-time data.

We consider additive noise in the form of a stochastic forcing term that can be decomposed into a sum of the ensemble average forcing and a stochastic process described in terms of a weighted cylindrical Wiener process (which is an infinite dimensional generalization of a Wiener process and represents noise in space and time). We derive our governing equation directly from Maxwell's equations with variable permittivity and permeability instead of the wave equation with variable wave speed, because phenomena such as depolarization are absent in the scalar wave equation formulation [48]. In this chapter, we assume that the variable permittivity and permeability are known *a priori*, e.g., from standard profiles (see, for example, [34] and references therein); they are not sources of uncertainty in the problem that we consider here.

The problem we tackle is how to construct a global approximation of the ensemble average ("noiseless") electric field using time series measurements $\mathbf{R}_{\mathbf{s}}(t)$ of the electric field obtained from a sensor at a fixed spatial location $\mathbf{s}$. The ensemble average field takes the form

$$\langle \mathbf{E} \rangle (\mathbf{x}, t) = \sum_{n} (a_n \cos(\omega_n t) + b_n \sin(\omega_n t)) \mathbf{\Phi}_n(\mathbf{x}) \tag{3.2}$$

where $\langle \cdot \rangle$ denotes the ensemble average. The functions $\mathbf{\Phi}_n(\mathbf{x})$ can be regarded as "features" of the problem. For the Maxwell vector wave equation, these features are eigenfunctions of a weighted curl squared operator (described below), but the only requirement of the analysis presented in this chapter is that the features be orthogonal. Thus, different operators and boundary conditions can be substituted, provided that the resulting eigenfunctions are orthogonal. The features framework is quite general and is related to work in many areas such as machine learning, compressed sensing, and randomized dynamic mode decomposition, e.g., [29, 17]. In our case, the eigenfunction formulation provides a way to represent wave-like phenomena in a

variety of domains and media.

To construct the ensemble average electric field, the frequencies $\omega_n$ (and other frequency information such as the eigenfunctions $\mathbf{\Phi}_n(\mathbf{x})$ and corresponding eigenvalues $\lambda_n$) and the amplitudes $a_n$ and $b_n$ need to be calculated from the sensor data. This chapter focuses on the latter problem of approximating $a_j$ and $b_j$ once the eigenfunctions and eigenvalues have already been computed. The frequency information can be obtained in several ways, such as extracting the peaks of the amplitude spectrum of the time series $\mathbf{R_s}(t)$ or computing the eigenfunctions and eigenvalues from a given domain. In general, multiple sensors may be necessary to construct an approximation of $\langle \mathbf{E} \rangle$, which we discuss in section 3.4.

The noisy electric field $\mathbf{E}(\mathbf{x}, t)$ is the solution to the stochastic Maxwell vector wave equation

$$\epsilon(\mathbf{x}) \frac{\partial^2 \mathbf{E}}{\partial t^2} + \nabla \times \left( [\mu(\mathbf{x})]^{-1} \nabla \times \mathbf{E} \right) = -\frac{\partial \mathbf{J}}{\partial t} \tag{3.3}$$

$$\frac{\partial \mathbf{J}}{\partial t} := \left\langle \frac{\partial \mathbf{J}}{\partial t} \right\rangle (\mathbf{x}, t) + \sqrt{Q} \frac{\partial \mathcal{W}}{\partial t} \tag{3.4}$$

where $\mathbf{J}$ denotes the current density and $\sqrt{Q}\frac{\partial \mathcal{W}}{\partial t}$ is the stochastic term described below. The goal is to use the sensor time series data $\mathbf{R_s}(t) := \mathbf{E}(\mathbf{s}, t)$ at location $\mathbf{s}$ to reconstruct the ensemble average sensor time series at any other location $\tilde{\mathbf{s}}$ or, equivalently, to reconstruct the solution to the (deterministic) ensemble average equation

$$\epsilon(\mathbf{x}) \frac{\partial^2 \langle \mathbf{E} \rangle}{\partial t^2} + \nabla \times \left( [\mu(\mathbf{x})]^{-1} \nabla \times \langle \mathbf{E} \rangle \right) = -\left\langle \frac{\partial \mathbf{J}}{\partial t} \right\rangle (\mathbf{x}, t). \tag{3.5}$$

To derive (3.5) directly from Maxwell's equations (in SI units), first take the differential form of Faraday's law of induction and Ampére's law:

$$\nabla \times \langle \mathbf{E} \rangle = -\frac{\partial \langle \mathbf{B} \rangle}{\partial t} \tag{3.6}$$

$$\nabla \times \langle \mathbf{H} \rangle = \langle \mathbf{J} \rangle + \frac{\partial \langle \mathbf{D} \rangle}{\partial t} \tag{3.7}$$

with the constitutive relations $\langle \mathbf{D} \rangle = \epsilon(\mathbf{x}) \langle \mathbf{E} \rangle$ and $\langle \mathbf{H} \rangle = [\mu(\mathbf{x})]^{-1} \langle \mathbf{B} \rangle$, and differentiate Ampére's law with respect to $t$:

$$\nabla \times \left( [\mu(\mathbf{x})]^{-1} \frac{\partial \langle \mathbf{B} \rangle}{\partial t} \right) = \left\langle \frac{\partial \mathbf{J}}{\partial t} \right\rangle + \epsilon(\mathbf{x}) \frac{\partial^2 \langle \mathbf{E} \rangle}{\partial t^2}. \tag{3.8}$$

Then, Faraday's law implies

$$-\nabla \times \left( [\mu(\mathbf{x})]^{-1} \nabla \times \langle \mathbf{E} \rangle \right) = \left\langle \frac{\partial \mathbf{J}}{\partial t} \right\rangle + \epsilon(\mathbf{x}) \frac{\partial^2 \langle \mathbf{E} \rangle}{\partial t^2}, \tag{3.9}$$

and rearranging the terms, we obtain the Maxwell vector wave equation (3.5). The spatial domain is $\Gamma$ in $\mathbb{R}^3$ and the initial conditions are

$$\mathbf{E}(\mathbf{x}, 0) = \mathbf{f}(\mathbf{x}), \qquad \mathbf{x} \in \Gamma \tag{3.10}$$

$$\frac{\partial \mathbf{E}}{\partial t}(\mathbf{x}, 0) = \mathbf{g}(\mathbf{x}), \qquad \mathbf{x} \in \Gamma. \tag{3.11}$$

To find the solution analytically, we consider the associated eigenvalue problem

$$\nabla \times \left( [\mu(\mathbf{x})]^{-1} \nabla \times \mathbf{\Phi} \right) - \lambda \epsilon(\mathbf{x}) \mathbf{\Phi} = 0. \tag{3.12}$$

Since the curl operator is symmetric, the eigenfunctions form an orthonormal set in $L^2(\Gamma; \mathbb{R}^3)$ with weight $\epsilon(\mathbf{x})$ up to suitable boundary conditions. We consider band limited electromagnetic signals in this model; therefore, we use only the set of eigenfunctions $\{\mathbf{\Phi}_n\}$ corresponding to positive eigenvalues $\{\lambda_n\}$, where the frequencies $\omega_n := \sqrt{\lambda_n}$ are in the range $[\omega_{min}, \omega_{max}]$ (in particular, we do not consider $\lambda = 0$ corresponding to eigenfunctions that are gradients of scalar functions, $\mathbf{\Phi} = \nabla f$). We can write solutions in the form

$$\mathbf{E}(\mathbf{x}, t) = \sum_n A_n(t) \mathbf{\Phi}_n(\mathbf{x}). \tag{3.13}$$

The operator $Q$ is a self-adjoint, trace-class operator defined by $Q\mathbf{\Phi}_n = \sigma_n^2 \mathbf{\Phi}_n$ with $\sum_{n \in \mathbb{N}} \sigma_n^2 < \infty$. We define a weighted Wiener process $\sqrt{Q}\mathcal{W}$ in terms of the operator

$Q$ and the cylindrical Wiener process $\mathcal{W}$ giving

$$\sqrt{Q}\frac{\partial \mathcal{W}}{\partial t} = \sum_{n\in\mathbb{N}} \sigma_n \frac{\partial \mathcal{W}_n}{\partial t}\epsilon(\mathbf{x})\mathbf{\Phi}_n \tag{3.14}$$

where $\{\mathcal{W}_n(t)\}$ are independent Wiener processes in time and are measured in units $\sec^{1/2}$, because the variance of a Wiener process scales linearly with time. The coefficients $\sigma_n$ are measured in units $NC^{-1}\sec^{-3/2}$. All the results that we present are scaled appropriately so that the relevant quantities, such as the electric field, are of order 1. For simplicity of notation, we define the forcing term $\mathbf{F} := \partial\mathbf{J}/\partial t$. Write the forcing ensemble average using the basis $\{\mathbf{\Phi}_n\}$:

$$\langle \mathbf{F}\rangle(\mathbf{x},t) = \sum_{n\in\mathbb{N}} \hat{F}_n(t)\epsilon(\mathbf{x})\mathbf{\Phi}_n(\mathbf{x}) \tag{3.15}$$

$$\hat{F}_n(t) = \int_\Gamma \epsilon(\mathbf{x})(\langle \mathbf{F}\rangle(\mathbf{x},t)/\epsilon(\mathbf{x}))\cdot\mathbf{\Phi}_n(\mathbf{x})\,d^3\mathbf{x}. \tag{3.16}$$

Then using (3.3) and the orthonormality of the basis $\{\mathbf{\Phi}_n\}$, we obtain the sequence of ODEs

$$A_n'' + \lambda_n A_n = \hat{F}_n + \sigma_n \frac{\partial \mathcal{W}_n}{\partial t}. \tag{3.17}$$

To solve each ODE, rewrite it as a first-order system

$$A_{n,1}' = A_{n,2} \tag{3.18}$$

$$A_{n,2}' = -\lambda_n A_{n,1} + \hat{F}_n + \sigma_n \frac{\partial \mathcal{W}_n}{\partial t}. \tag{3.19}$$

Multiplying by $dt$, we obtain the standard representation

$$d\mathbf{A}_n(t) = M_n\mathbf{A}_n(t)dt + \hat{\mathbf{F}}_n(t)dt + \mathbf{K}_n d\mathcal{W}_n, \tag{3.20}$$

where

$$M_n = \begin{bmatrix} 0 & 1 \\ -\lambda_n & 0 \end{bmatrix}, \hat{\mathbf{F}}_n(t) = \begin{bmatrix} 0 \\ \hat{F}_n(t) \end{bmatrix}, \mathbf{K}_n = \begin{bmatrix} 0 \\ \sigma_n \end{bmatrix}, \mathbf{A}_n = \begin{bmatrix} A_{n,1} \\ A_{n,2} \end{bmatrix}. \tag{3.21}$$

In the classical deterministic case, (3.20) is multiplied by $e^{-M_n t}$:

$$e^{-M_n t} d\mathbf{A}_n(t) - e^{-M_n t} M_n \mathbf{A}_n(t) dt = e^{-M_n t} \hat{\mathbf{F}}_n(t) dt + e^{-M_n t} \mathbf{K}_n d\mathcal{W}_n \tag{3.22}$$

and we rewrite the left hand side as $d(e^{-M_n t}\mathbf{A}_n(t))$. To extend this notion to our stochastic case, we use Itô's formula. Consider the stochastic process

$$Y(t) = g(t, A_{n,1}, A_{n,2}) = e^{-M_n t} \begin{bmatrix} A_{n,1} \\ A_{n,2} \end{bmatrix}. \tag{3.23}$$

Itô's formula gives

$$dY(t) = -M_n e^{-M_n t} \mathbf{A}_n dt + e^{-M_n t} d\mathbf{A}_n. \tag{3.24}$$

Substitute (3.24) into (3.22):

$$d(e^{-M_n t}\mathbf{A}_n(t)) = e^{-M_n t} \hat{\mathbf{F}}_n(t) dt + e^{-M_n t} \mathbf{K}_n d\mathcal{W}_n(t) \tag{3.25}$$

which gives

$$e^{-M_n t}\mathbf{A}_n(t) - e^{-M_n 0}\mathbf{A}_n(0) = \int_0^t e^{-M_n r} \hat{\mathbf{F}}_n(r)\, dr + \int_0^t e^{-M_n r} \mathbf{K}_n d\mathcal{W}_n(r). \tag{3.26}$$

Using the stochastic integration by parts formula:

$$\int_0^t f(r) d\mathcal{W}_n(r) = f(t)\mathcal{W}_n - \int_0^t \mathcal{W}_n(r) df(r) \tag{3.27}$$

with

$$f(r) = e^{-M_n r}\mathbf{K}_n \quad \text{and} \quad df(r) = -M_n e^{-M_n r}\mathbf{K}_n dr, \tag{3.28}$$

the stochastic solution is

$$\mathbf{A}_n(t) = e^{M_n t}\left[\mathbf{A}_n(0) + \int_0^t \left(e^{-M_n r}\hat{\mathbf{F}}_n(r) + \mathcal{W}_n(r) M_n e^{-M_n r}\mathbf{K}_n\right) dr\right] \tag{3.29}$$

and the solution to (3.3) is

$$\mathbf{E}(\mathbf{x},t) = \sum_{n\in\mathbb{N}} A_n(t)\mathbf{\Phi}_n(\mathbf{x}) \tag{3.30}$$

$$A_n(t) = \hat{f}_n \cos(\sqrt{\lambda_n}t) + \frac{\hat{g}_n}{\sqrt{\lambda_n}} \sin(\sqrt{\lambda_n}t) + \int_0^t \frac{1}{\sqrt{\lambda_n}} \sin(\sqrt{\lambda_n}(t-r))\hat{F}_n(r) + \cos(\sqrt{\lambda_n}(t-r))\sigma_n \mathcal{W}_n(r)\, dr. \tag{3.31}$$

We use the Itô integral version of $A_n(t)$ in second-moment calculations:

$$A_n(t) = \hat{f}_n \cos(\sqrt{\lambda_n}t) + \frac{\hat{g}_n}{\sqrt{\lambda_n}} \sin(\sqrt{\lambda_n}t) + \int_0^t \frac{1}{\sqrt{\lambda_n}} \sin(\sqrt{\lambda_n}(t-r))\hat{F}_n(r)\, dr + \int_0^t \frac{\sigma_n}{\sqrt{\lambda_n}} \sin(\sqrt{\lambda_n}(t-r))\, d\mathcal{W}_n(r). \tag{3.32}$$

## 3.3 Analysis of the Stochastic Model

We now compute statistics of the solution and analyze its behavior. Since expectation $\mathbb{E}$ is a linear operator, the mean solution is the deterministic solution:

$$\mathbb{E}\left[\mathbf{E}(\mathbf{x},t)\right] = \sum_{n\in\mathbb{N}} \langle A_n(t)\rangle \mathbf{\Phi}_n(\mathbf{x}) \tag{3.33}$$

$$\langle A_n(t)\rangle = \hat{f}_n \cos(\sqrt{\lambda_n}t) + \frac{\hat{g}_n}{\sqrt{\lambda_n}} \sin(\sqrt{\lambda_n}t) + \int_0^t \frac{1}{\sqrt{\lambda_n}} \sin(\sqrt{\lambda_n}(t-r))\hat{F}_n(r)\, dr. \tag{3.34}$$

We compute the covariance of the fields:

$$\begin{aligned}
\mathrm{COV}\left(\mathbf{E}(\mathbf{x}_1,t_1),\mathbf{E}(\mathbf{x}_2,t_2)\right) &= \sum_{n\in\mathbb{N}}\sum_{m\in\mathbb{N}} \mathbf{\Phi}_n(\mathbf{x}_1)\mathbf{\Phi}_m^T(\mathbf{x}_2) \\
&\times \mathbb{E}\Big[\int_0^{t_1} \frac{\sigma_n}{\sqrt{\lambda_n}}\sin(\sqrt{\lambda_n}(t_1-r))\,d\mathcal{W}_n(r) \\
&\times \int_0^{t_2} \frac{\sigma_m}{\sqrt{\lambda_m}}\sin(\sqrt{\lambda_m}(t_2-r))\,d\mathcal{W}_m(r)\Big] \\
&= \sum_{n\in\mathbb{N}} \mathbf{\Phi}_n(\mathbf{x}_1)\mathbf{\Phi}_n^T(\mathbf{x}_2)\frac{\sigma_n^2}{\lambda_n} \\
&\times \int_0^{t_1\wedge t_2} \sin(\sqrt{\lambda_n}(t_1-r))\sin(\sqrt{\lambda_n}(t_2-r))\,dr \\
&= \sum_{n\in\mathbb{N}} \mathbf{\Phi}_n(\mathbf{x}_1)\mathbf{\Phi}_n^T(\mathbf{x}_2)\frac{\sigma_n^2}{4\lambda_n^{3/2}}\Big(2\sqrt{\lambda_n}t_1\wedge t_2\cos(\sqrt{\lambda_n}(t_2-t_1)) \\
&- \sin(\sqrt{\lambda_n}(2t_1\wedge t_2-t_2-t_1)) - \sin(\sqrt{\lambda_n}(t_1+t_2))\Big)
\end{aligned} \tag{3.35}$$

using the identity

$$\mathbb{E}\left[\int_0^{t_1}\phi(r_1)\,d\mathcal{W}_j(r_1)\cdot\int_0^{t_2}\eta(r_2)\,d\mathcal{W}_j(r_2)\right] = \int_0^{t_1\wedge t_2}\phi(r)\eta(r)\,dr, \tag{3.36}$$

where $a\wedge b$ is the minimum of $a$ and $b$. When $\mathbf{x}_1=\mathbf{x}_2$ and $t_1=t_2$ we obtain the covariance of the components of the electric field:

$$\begin{aligned}
\mathrm{COV}\left[\mathbf{E}(\mathbf{x},t)\right] &= \sum_{n\in\mathbb{N}} \mathbf{\Phi}_n(\mathbf{x})\mathbf{\Phi}_n^T(\mathbf{x})\frac{\sigma_n^2}{4\lambda_n^{3/2}}\left(2\sqrt{\lambda_n}t-\sin(2\sqrt{\lambda_n}t)\right) \\
&= \sum_{n\in\mathbb{N}} \mathbf{\Phi}_n(\mathbf{x})\mathbf{\Phi}_n^T(\mathbf{x})\mathrm{VAR}[A_n(t)]
\end{aligned} \tag{3.37}$$

where

$$\mathrm{VAR}[A_n(t)] = \frac{\sigma_n^2}{4\lambda_n^{3/2}}\left(2\sqrt{\lambda_n}t-\sin(2\sqrt{\lambda_n}t)\right). \tag{3.38}$$

The variance of $A_n(t)$ is displayed in Figure 3.3. From (3.37) we see that the variance of the electric field grows linearly with time. To quantify the noise, we calculate the signal-to-noise ratio. For a time series written as $R(t)=D(t)+S(t)$ where $D(t)$ is

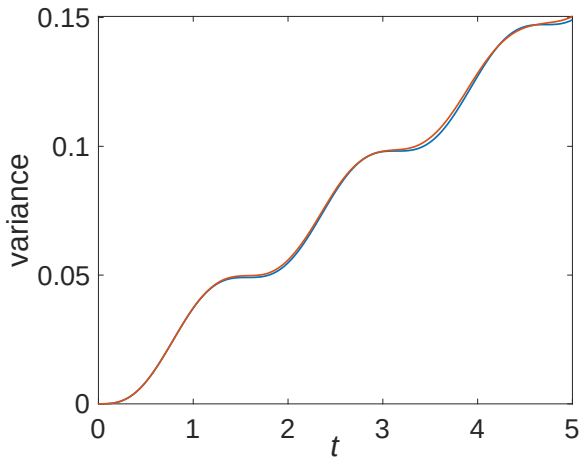


**Figure 3.1:** Variance of $A_n(t)$ (3.38) where $n$ corresponds to the eigenvalue $\lambda_n = 4$ and $\sigma_n = 0.5$. The simulated variance is in red and the exact variance obtained from (3.38) is in blue.

the deterministic signal and $S(t)$ is the stochastic noise, we define the signal-to-noise ratio (SNR) to be

$$\text{SNR} = 10 \log_{10} (P_D / P_S) \tag{3.39}$$

where

$$P_D(\tau) = \frac{1}{\tau} \int_0^\tau D^2(t)\, dt \tag{3.40}$$

$$P_S(\tau) = \frac{1}{\tau} \int_0^\tau \mathbb{E}[S^2(t)]\, dt. \tag{3.41}$$

Suppose we observe the one-frequency case:

$$\mathbf{E}(\mathbf{x}, t) = A_n(t) \mathbf{\Phi}_n(\mathbf{x}), \text{ for some } n \in \mathbb{N} \tag{3.42}$$

from a sensor at a fixed location $\mathbf{s} \in \Gamma$ and obtain the time series $\mathbf{R_s}(t)$. Further suppose $\langle \mathbf{F} \rangle = \mathbf{g} = 0$. The signal of $\mathbf{R_s}(t)$ is averaged over $p = k2\pi$ periods ($\tau =$

$k2\pi/\sqrt{\lambda_n}$) to obtain the power of the signal and noise for the $i^{th}$ component:

$$P_D = \phi_{n,i}^2(\mathbf{s})\frac{\hat{f}_n^2}{2} \tag{3.43}$$

$$\begin{aligned} P_S &= \frac{1}{\tau}\int_0^\tau \phi_{n,i}^2(\mathbf{s})\frac{\sigma_n^2}{4\lambda_n^{3/2}}\left(2\sqrt{\lambda_n}t - \sin(2\sqrt{\lambda_n}t)\right)\,dt \\ &= \phi_{n,i}^2(\mathbf{s})\,\frac{k\pi\sigma_n^2}{2\lambda_n^{3/2}}. \end{aligned} \tag{3.44}$$

The corresponding SNR (in dB) is

$$\mathrm{SNR} = 10\log_{10}\left(\frac{\lambda_n^{3/2}\hat{f}_n^2}{k\pi\sigma_n^2}\right). \tag{3.45}$$

Thus, we see from (3.45) that the noise eventually dominates the signal in the sensor time series as $k$ increases; in practice, however, this will happen only slowly if $\sigma_n$ is small. For the more general case of $N$ frequencies, we can approximate for large $\tau$:

$$P_D = \sum_n \phi_{n,i}^2(\mathbf{s})\frac{\hat{f}_n^2}{2} \tag{3.46}$$

$$\begin{aligned} P_S &= \sum_n \frac{1}{\tau}\int_0^\tau \phi_{n,i}^2(\mathbf{s})\frac{\sigma_n^2}{4\lambda_n^{3/2}}\left(2\sqrt{\lambda_n}t - \sin(2\sqrt{\lambda_n}t)\right)\,dt \\ &= \sum_n \phi_{n,i}^2(\mathbf{s})\frac{\sigma_n^2}{4\lambda_n^{3/2}}\frac{1}{\tau}\left(\sqrt{\lambda_n}\tau^2 + \frac{1}{2\sqrt{\lambda_n}}\cos(2\sqrt{\lambda_n}\tau) - \frac{1}{2\sqrt{\lambda_n}}\right) \\ &\approx \sum_n \phi_{n,i}^2(\mathbf{s})\frac{\sigma_n^2}{4\lambda_n}\tau. \end{aligned} \tag{3.47}$$

The approximate signal-to-noise ratio is

$$\mathrm{SNR} = 10\log_{10}\left(\frac{\sum_n \phi_{n,i}^2(\mathbf{s})\hat{f}_n^2}{\sum_n \phi_{n,i}^2(\mathbf{s})\sigma_n^2/2\lambda_n}\right) - 10\log_{10}(\tau) \tag{3.48}$$

so $\mathrm{SNR} \to \infty$ as $\tau \to 0$.

Lastly, we observe that the expected energy stored in the electric field increases linearly with time:

$$\begin{aligned} U &= \int_\Gamma \frac{\epsilon(\mathbf{x})}{2}\mathbb{E}\left[\mathbf{E}\cdot\mathbf{E}\right]\,d^3\mathbf{x} \\ &= \frac{1}{2}\left[\sum_{n\in\mathbb{N}}[\langle A_n(t)\rangle]^2 + \frac{\sigma_n^2}{4\lambda_n^{3/2}}\left(2\sqrt{\lambda_n}t - \sin(2\sqrt{\lambda_n}t)\right)\right]. \end{aligned} \tag{3.49}$$

## 3.4 Analysis of Global Approximations

To construct an approximation of the $i^{th}$ component of the ensemble average electric field at a spatial location $\tilde{s}$ using the time series $\mathbf{R_s}(t)$ of the electric field at spatial location $\mathbf{s}$, we first construct the ensemble average field at $\mathbf{s}$:

$$\langle R_{\mathbf{s},i}(t)\rangle = \sum_n c_n \cos(\omega_n t) + d_n \sin(\omega_n t) \tag{3.50}$$

and then use the ansatz (3.2) to obtain the time series

$$\langle R_{\tilde{\mathbf{s}},i}(t)\rangle = \sum_n \frac{\Phi_{n,i}(\tilde{\mathbf{s}})}{\Phi_{n,i}(\mathbf{s})} c_n \cos(\omega_n t) + \frac{\Phi_{n,i}(\tilde{\mathbf{s}})}{\Phi_{n,i}(\mathbf{s})} d_n \sin(\omega_n t). \tag{3.51}$$

To accomplish the first step, the dominant frequencies $\omega_n$ are obtained from the peaks of the amplitude spectrum of the time series $\mathbf{R_s}(t)$. Then, the coefficients $c_n$ and $d_n$ are approximated using the frequencies $\omega_n$. Finally, the frequencies $\omega_n$ are used to identify the corresponding eigenfunctions $\mathbf{\Phi}_n(\mathbf{x})$ and eigenvalues $\lambda_n$. The frequencies can then be written as $\omega_n = \sqrt{\lambda_n}$ and the coefficients can be written as $c_n = \hat{f}_n \Phi_{n,i}(\mathbf{s})$ and $d_n = \hat{g}_n \Phi_{n,i}(\mathbf{s})/\sqrt{\lambda_n}$. In general, identifying the eigenfunctions $\mathbf{\Phi}_n(\mathbf{x})$ may require multiple sensors at different locations, which we briefly discuss in section 3.4.1.

In the remainder of this section, we fix an index $j$ and focus on how to determine the particular coefficients $\hat{f}_j$ and $\hat{g}_j$ associated with the frequency $\sqrt{\lambda_j}$ from the sensor time series data. In section 3.4.1, we analyze the estimates of $\hat{f}_j$ and $\hat{g}_j$ and the associated mean squared errors (MSE) which can be expressed as sums of the squared bias and variance. The MSE of a coefficient estimate is a function of the total length $\tau$ of the time series, and we show that it can be minimized by deriving closed-form expressions for the dominant terms. Finally, in section 3.4.2, we simulate the MSE of the coefficient $\hat{f}_j$ for the case of a two-frequency electric field to show how the MSE depends on the relevant parameters of the problem and how the non-dominant terms in the MSE affect the estimation. Throughout this section, $j$ represents the index

of the coefficients associated with the frequency of interest, $n$ is a summation index, and $k$ is the index of another frequency in the series. In section 3.5, we consider the problem of estimating all of the coefficients, not just the coefficients $\hat{f}_j$ and $\hat{g}_j$.

### *3.4.1 Coefficient Estimation and MSE*

First we describe how to estimate the coefficients $\hat{f}_j$ and $\hat{g}_j$ in the deterministic case. Suppose that we observe the (deterministic) vector time series $\mathbf{R}^0_{\mathbf{s}}(t)$ at some fixed location $\mathbf{s}$ in the domain $\Gamma$ over the time interval $0 \leq t \leq \tau$. To obtain the coefficients $\hat{f}_j$ and $\hat{g}_j$ associated with frequency $\sqrt{\lambda_j}$, the classical theory yields the vectors

$$\begin{aligned}\boldsymbol{\alpha}_j(\tau) &:= \frac{1}{\tau}\int_0^\tau \mathbf{R}^0_{\mathbf{s}}(t)\cos(\sqrt{\lambda_j}\,t)\,dt \qquad (3.52)\\ &= \sum_n \boldsymbol{\Phi}_n(\mathbf{s})\left(\hat{f}_n D_{cc}(\tau;\sqrt{\lambda_n},\sqrt{\lambda_j}) + \frac{\hat{g}_n}{\sqrt{\lambda_n}} D_{sc}(\tau;\sqrt{\lambda_n},\sqrt{\lambda_j})\right)\\ \boldsymbol{\beta}_j(\tau) &:= \frac{1}{\tau}\int_0^\tau \mathbf{R}^0_{\mathbf{s}}(t)\sin(\sqrt{\lambda_j}\,t)\,dt \qquad (3.53)\\ &= \sum_n \boldsymbol{\Phi}_n(\mathbf{s})\left(\hat{f}_n D_{cs}(\tau;\sqrt{\lambda_n},\sqrt{\lambda_j}) + \frac{\hat{g}_n}{\sqrt{\lambda_n}} D_{ss}(\tau;\sqrt{\lambda_n},\sqrt{\lambda_j})\right)\end{aligned}$$

where

$$D_{cc}(\tau;\sqrt{\lambda_n},\sqrt{\lambda_j}) := \frac{1}{\tau}\int_0^\tau \cos(\sqrt{\lambda_n}\,t)\cos(\sqrt{\lambda_j}\,t)\,dt. \qquad (3.54)$$

The terms $D_{sc}, D_{cs}$, and $D_{ss}$ are defined similarly by replacing cosine with sine. In the special limit case where $\tau \to \infty$, we obtain

$$\begin{aligned}\lim_{\tau\to\infty}\boldsymbol{\alpha}_j(\tau) &= \sum_{n\in I_{\lambda_j}} \boldsymbol{\Phi}_n(\mathbf{s})\tfrac{\hat{f}_n}{2} \qquad (3.55)\\ \lim_{\tau\to\infty}\boldsymbol{\beta}_j(\tau) &= \sum_{n\in I_{\lambda_j}} \boldsymbol{\Phi}_n(\mathbf{s})\tfrac{\hat{g}_n}{2\sqrt{\lambda_j}}. \qquad (3.56)\end{aligned}$$

The number of terms in each sum is the multiplicity of the eigenvalue $\lambda_j$ of interest, i.e., $I_{\lambda_j} = \{n : \lambda_n = \lambda_j\}$. We can solve for the coefficients $\hat{f}_n$ and $\hat{g}_n$ in each system

using a single sensor time series $\mathbf{R}_{\mathbf{s}}^0(t)$ only if every eigenvalue has multiplicity 1. We thus obtain a result similar to the case of the wave equation as in [5]: the number of sensors must be at least as large as the highest multiplicity of any eigenvalue. When only one sensor is used, we also require $\mathbf{\Phi}_n(\mathbf{s}) \neq \mathbf{0}$ for every $n$.

In the analysis that follows, we consider the case where all eigenvalues have multiplicity 1, which occurs when all waves in the field $\mathbf{E}$ propagate in one direction. In the general case where eigenvalues have higher multiplicity, multiple sensors can be used together to construct the field (see [5]). Assuming that the sensor observes for a finite time $\tau$, the $i^{th}$ component of the sensor time series can be used to obtain the approximation

$$\hat{f}_j \approx \frac{\alpha_{j,i}(\tau)}{\Phi_{j,i}(\mathbf{s}) D_{cc}(\tau; \sqrt{\lambda_j}, \sqrt{\lambda_j})}. \tag{3.57}$$

Now suppose that the electric field $\mathbf{E}$ is the solution of the stochastic Maxwell vector wave equation, (3.3)–(3.4) and we observe the time series $\mathbf{R}_{\mathbf{s}}(t) = \mathbf{E}(\mathbf{s}, t)$ at location $\mathbf{s}$. In this case, the relations (3.55) and (3.56) represent stochastic processes, and the mean squared error (MSE) in the coefficient estimator (3.57) can be decomposed into bias and variance components:

$$\mathrm{MSE}(\tau; j) := \mathbb{E}\left[\left(\hat{f}_j - \frac{\alpha_{j,i}(\tau)}{\Phi_{j,i}(\mathbf{s}) D_{cc}(\tau; \sqrt{\lambda_j}, \sqrt{\lambda_j})}\right)^2\right] = [\mathrm{BIAS}(\tau; j)]^2 + \mathrm{VAR}(\tau; j). \tag{3.58}$$

To better understand how the error in our estimate of $\hat{f}_j$ depends on the observation time $\tau$, we derive closed-form expressions for the bias and variance terms. The analysis is similar for $\hat{g}_j$.

### Bias of the Estimated Coefficients

We first compute the bias. Since each $A_n(t)$ is a superposition of the deterministic solution $\langle A_n(t)\rangle$ and terms containing $\mathcal{W}_n(t)$, we need only to compute expected values of the latter terms. Since $\mathbb{E}[\mathcal{W}_n(t)] = 0$ for all $t$,

$$\mathbb{E}\left[S_c(\tau; \sqrt{\lambda_n}, \sqrt{\lambda_j})\right] = 0 \tag{3.59}$$

where

$$S_c(\tau; \sqrt{\lambda_n}, \sqrt{\lambda_j}) := \frac{1}{\tau}\int_0^\tau \left(\int_0^t \cos(\sqrt{\lambda_n}(t-r))\mathcal{W}_n(r)\,dr\right)\cos(\sqrt{\lambda_j}\,t)\,dt \tag{3.60}$$

and $S_s$ is defined similarly by replacing the last cosine with sine. Thus, the bias is simply the difference between $\hat{f}_j$ and the estimator in (3.57) in the deterministic case:

$$\begin{aligned}\text{BIAS}(\tau; j) = \sum_{n\neq j}\frac{\Phi_{n,i}(\mathbf{s})}{\Phi_{j,i}(\mathbf{s})}\left(\hat{f}_n\frac{D_{cc}(\tau;\sqrt{\lambda_n},\sqrt{\lambda_j})}{D_{cc}(\tau;\sqrt{\lambda_j},\sqrt{\lambda_j})} + \frac{\hat{g}_n}{\sqrt{\lambda_n}}\frac{D_{sc}(\tau;\sqrt{\lambda_n},\sqrt{\lambda_j})}{D_{cc}(\tau;\sqrt{\lambda_j},\sqrt{\lambda_j})}\right) \\ + \frac{\hat{g}_j}{\sqrt{\lambda_j}}\frac{D_{sc}(\tau;\sqrt{\lambda_j},\sqrt{\lambda_j})}{D_{cc}(\tau;\sqrt{\lambda_j},\sqrt{\lambda_j})}.\end{aligned} \tag{3.61}$$

The terms $D_{cc}$ and $D_{sc}$ can be easily computed explicitly. For $\sqrt{\lambda_n} \neq \sqrt{\lambda_j}$,

$$D_{cc}(\tau; \sqrt{\lambda_n}, \sqrt{\lambda_j}) = \frac{1}{2}\left(\frac{\sin((\sqrt{\lambda_n}+\sqrt{\lambda_j})\tau)}{(\sqrt{\lambda_n}+\sqrt{\lambda_j})\tau} + \frac{\sin((\sqrt{\lambda_n}-\sqrt{\lambda_j})\tau)}{(\sqrt{\lambda_n}-\sqrt{\lambda_j})\tau}\right) \tag{3.62}$$

and

$$D_{cc}(\tau; \sqrt{\lambda_j}, \sqrt{\lambda_j}) = \frac{1}{2}\left(\frac{\sin(2\sqrt{\lambda_j}\tau)}{2\sqrt{\lambda_j}\tau} + 1\right). \tag{3.63}$$

### Resonant Variance of the Estimated Coefficients

The calculation of the variance is more complex, so we focus on computing the dominant term of the variance, which is the resonant variance that we define below. We utilize simulations of the MSE to understand the behavior of the nonresonant variance

terms in section 3.4.2. In general, the variance can be written as

$$\mathrm{VAR}(\tau; j) = \mathbb{E}\left[\sum_n \left(\frac{\sigma_n \Phi_{n,i}(\mathbf{s})}{\Phi_{j,i}(\mathbf{s}) D_{cc}(\tau; \sqrt{\lambda_j}, \sqrt{\lambda_j})} S_c(\tau; \sqrt{\lambda_n}, \sqrt{\lambda_j})\right)^2\right]. \tag{3.64}$$

The resonant term of the variance is

$$\mathrm{VAR}_{\mathrm{res}}(\tau; j) := \mathbb{E}\left[\left(\frac{\sigma_j}{D_{cc}(\tau; \sqrt{\lambda_j}, \sqrt{\lambda_j})} S_c(\tau; \sqrt{\lambda_j}, \sqrt{\lambda_j})\right)^2\right] \tag{3.65}$$

which is the variance for the one-frequency case (3.42) and can, for that case, be written as

$$\mathrm{VAR}_{\mathrm{res}}(\tau; j) = \mathrm{VAR}(\tau; j) = \frac{\mathrm{VAR}[\alpha_{j,i}(\tau)]}{(\Phi_{j,i}(\mathbf{s}) D_{cc}(\tau; \sqrt{\lambda_j}, \sqrt{\lambda_j}))^2}. \tag{3.66}$$

We thus find the covariance matrix of $\boldsymbol{\alpha}_j(\tau)$ in the one-frequency case (3.42). Observe that

$$\begin{aligned}
&\mathrm{COV}\left[\frac{1}{\tau}\int_0^\tau \mathbf{R}_{\mathbf{s}}(t)\cos(\sqrt{\lambda_j}\,t)\,dt\right] \qquad (3.67)\\
&= \boldsymbol{\Phi}_j(\mathbf{s})\boldsymbol{\Phi}_j^T(\mathbf{s})\mathbb{E}\left[\left(\frac{1}{\tau}\int_0^\tau\int_0^t \frac{\sigma_j}{\sqrt{\lambda_j}}\sin(\sqrt{\lambda_j}(t-r))\,d\mathcal{W}_j(r)\cos(\sqrt{\lambda_j}\,t)\,dt\right)^2\right]\\
&= \boldsymbol{\Phi}_j(\mathbf{s})\boldsymbol{\Phi}_j^T(\mathbf{s})\frac{\sigma_j^2}{\lambda_j\tau^2}\int_0^\tau\int_0^\tau \mathbb{E}\left[\left(\int_0^{t_1}\sin(\sqrt{\lambda_j}(t_1-r_1))\cos(\sqrt{\lambda_j}\,t_1)\,d\mathcal{W}_j(r_1)\right)\right.\\
&\left.\times\left(\int_0^{t_2}\sin(\sqrt{\lambda_j}(t_2-r_2))\,\cos(\sqrt{\lambda_j}\,t_2)\,d\mathcal{W}_j(r_2)\right)\right]dt_1dt_2.
\end{aligned}$$

We now use the trigonometric difference formula for sine and the identity (3.36) to split the variance into four terms:

$$\begin{aligned}
\frac{\sigma_j^2}{\lambda_j\tau^2}\int_0^\tau\int_0^\tau\int_0^{t_1\wedge t_2} &\Big(\sin(\sqrt{\lambda_j}t_1)\cos(\sqrt{\lambda_j}r)\cos(\sqrt{\lambda_j}t_1) \qquad (3.68)\\
&\quad -\cos(\sqrt{\lambda_j}t_1)\sin(\sqrt{\lambda_j}r)\cos(\sqrt{\lambda_j}t_1)\Big)\\
&\times\Big(\sin(\sqrt{\lambda_j}t_2)\cos(\sqrt{\lambda_j}r)\cos(\sqrt{\lambda_j}t_2)\\
&\quad -\cos(\sqrt{\lambda_j}t_2)\sin(\sqrt{\lambda_j}r)\cos(\sqrt{\lambda_j}t_2)\Big)\,dr\,dt_1\,dt_2.
\end{aligned}$$

We obtain the covariance of $\boldsymbol{\alpha}_j(\tau)$:

$$\mathrm{COV}[\boldsymbol{\alpha}_j(\tau)] = \boldsymbol{\Phi}_j(\mathbf{s})\boldsymbol{\Phi}_j^T(\mathbf{s})\frac{\sigma_j^2}{192\lambda_j^{3/2}}\Big(8\lambda_j^{1/2}\tau + 12\sin(2\sqrt{\lambda_j}\tau) - 12\lambda_j^{-1/2}\tau^{-1} + 3\lambda_j^{-1}\tau^{-2}\sin(4\sqrt{\lambda_j}\tau)\Big). \tag{3.69}$$

By a similar computation, we obtain the covariance of $\boldsymbol{\beta}_j(\tau)$:

$$\mathrm{COV}[\boldsymbol{\beta}_j(\tau)] = \boldsymbol{\Phi}_j(\mathbf{s})\boldsymbol{\Phi}_j^T(\mathbf{s})\frac{\sigma_j^2}{192\lambda_j^{3/2}}\Bigg(8\lambda_j^{1/2}\tau - 12\sin(2\sqrt{\lambda_j}\tau) + 36\lambda_j^{-1/2}\tau^{-1} + 24\lambda_j^{-1/2}\tau^{-1}\cos(2\sqrt{\lambda_j}\tau) - 3\lambda_j^{-1}\tau^{-2}\sin(4\sqrt{\lambda_j}\tau) - 24\lambda_j^{-1}\tau^{-2}\sin(2\sqrt{\lambda_j}\tau)\Bigg). \tag{3.70}$$

Using $\tau = p/\sqrt{\lambda_j}$, the covariance can be written in terms of periods:

$$\mathrm{COV}[\boldsymbol{\alpha}_j(p)] = \boldsymbol{\Phi}_j(\mathbf{s})\boldsymbol{\Phi}_j^T(\mathbf{s})\frac{\sigma_j^2}{192\lambda_j^{3/2}}\Big(8p + 12\sin(2p) - 12p^{-1} + 3p^{-2}\sin(4p)\Big) \tag{3.71}$$

$$\mathrm{COV}[\boldsymbol{\beta}_j(p)] = \boldsymbol{\Phi}_j(\mathbf{s})\boldsymbol{\Phi}_j^T(\mathbf{s})\frac{\sigma_j^2}{192\lambda_j^{3/2}}\Bigg(8p - 12\sin(2p) + 36p^{-1} + 24p^{-1}\cos(2p) - 3p^{-2}\sin(4p) - 24p^{-2}\sin(2p)\Bigg). \tag{3.72}$$

Similar to the covariance of the electric field $\mathbf{E}$ itself, the covariances of $\boldsymbol{\alpha}_j(\tau)$ and $\boldsymbol{\beta}_j(\tau)$ grow as $\mathcal{O}(\tau)$.

### *3.4.2 The Two-Frequency Case*

We now analyze the MSE (3.58) for the simplest model that contains all of the relevant terms: bias, resonant variance, and nonresonant variance. The bias and resonant variance have closed-form expressions, and we simulate the nonresonant variance. The electric field is given by

$$\mathbf{E}(\mathbf{x},t) = \sum_{n\in\{j,k\}} \boldsymbol{\Phi}_n(\mathbf{x})\left(\hat{f}_n\cos(\sqrt{\lambda_n}t) + \int_0^t \cos(\sqrt{\lambda_n}(t-r))\sigma_n\mathcal{W}_n(r)\,dr\right) \tag{3.73}$$

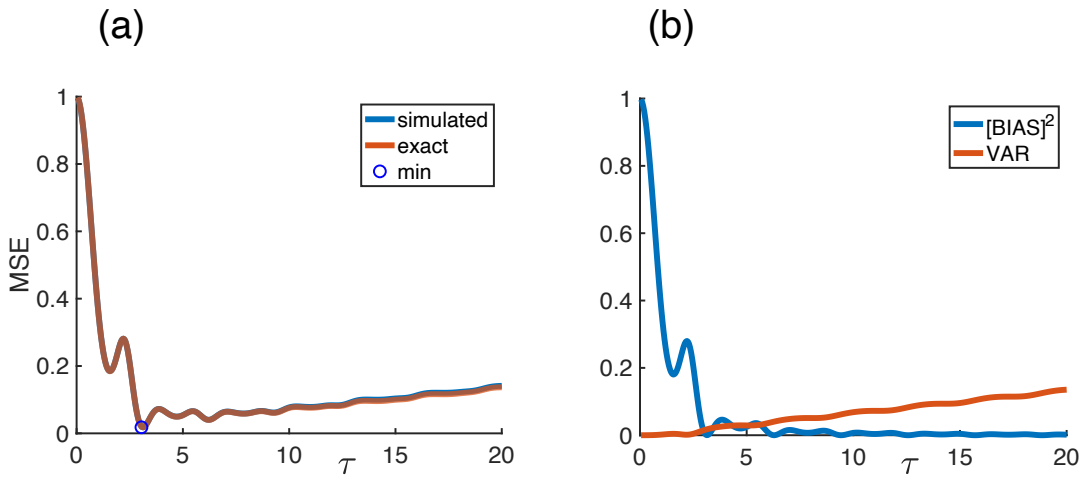


**Figure 3.2:** (a) Mean squared error (MSE) (3.74) versus observation time $\tau$ with $\sigma_k = 0$ for the two-frequency case (3.73). The simulated MSE is in blue and the exact closed-form MSE is in red. (b) The squared bias (3.61) and variance (3.64) terms of coefficient $\hat{f}_j$ whose sum is the MSE (3.74).

and the MSE of the estimate of $\hat{f}_j$ in this case is

$$\begin{aligned}\mathrm{MSE}(\tau; j) &= [\mathrm{BIAS}(\tau; j)]^2 \\ &+ \mathbb{E}\left[\left(\frac{\sigma_j S_c(\tau; \sqrt{\lambda_j}, \sqrt{\lambda_j})}{D_{cc}(\tau; \sqrt{\lambda_j}, \sqrt{\lambda_j})}\right)^2 + \left(\frac{\sigma_k \Phi_{k,i}(\mathbf{s}) S_c(\tau; \sqrt{\lambda_k}, \sqrt{\lambda_j})}{\Phi_{j,i}(\mathbf{s}) D_{cc}(\tau; \sqrt{\lambda_j}, \sqrt{\lambda_j})}\right)^2\right].\end{aligned} \tag{3.74}$$

The MSE (3.74) is dominated by the squared bias term for small $\tau$ since the squared bias term is $\mathcal{O}(\tau^{-2})$ and is dominated by the resonant variance term as $\tau$ becomes large since the resonant variance term is $\mathcal{O}(\tau)$. So, although the error may decrease initially, it grows as $\mathcal{O}(\tau)$ for large $\tau$. Figure 3.2, which displays a graph of the MSE (3.74) with $\sigma_k = 0$, confirms this behavior. In this graph, the error decays initially, reaches a minimum, and then increases approximately linearly with $\tau$. The optimal observation time for the sensor to reconstruct $\hat{f}_j$ is at this minimum.

To plot the MSE (3.74) with $\sigma_k \neq 0$, the nonresonant variance term $S_c(\tau; \sqrt{\lambda_k}, \sqrt{\lambda_j})$ must be simulated numerically. In Figures 3.3-3.4, the MSE is computed with $\sigma_k \neq 0$ for a range of values for the parameters $\omega_k - \omega_j$, $\sigma_j$, and $\sigma_k$. In

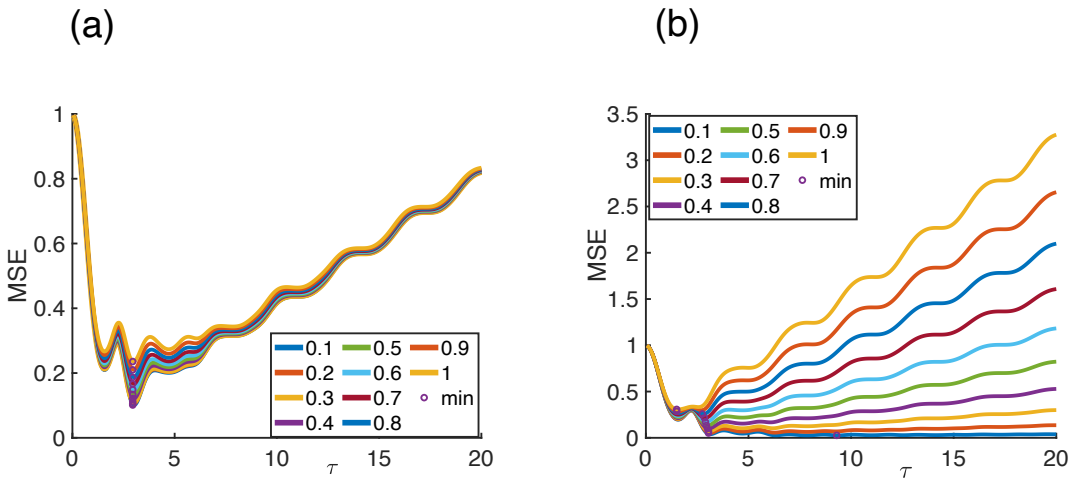


**Figure 3.3:** MSE (3.74) versus observation time $\tau$ as a function of the coefficients $\sigma_j$ and $\sigma_k$ corresponding to the frequency of interest $\omega_j$ and a secondary frequency $\omega_k$. (a) MSE for $\sigma_j$ fixed at 0.5 and various choices of $\sigma_k$. (b) MSE for $\sigma_k$ fixed at 0.5 and various choices of $\sigma_j$. The coefficients are $\hat{f}_j = 1$ and $\hat{f}_k = -1$.

(3.3), $\sigma_k$ is varied between 0.1 and 1 with very little change in either the error function or the optimal observation time (plotted in purple). The results suggest that the behavior of the reconstruction error in the two-frequency case is dominated by the squared bias and resonant variance terms. Figure 3.4 displays a case where no reconstruction can be obtained without significant error. In the deterministic case, when $\omega_j$ and $\omega_k$ are close together, longer observation times are required to differentiate the two signals. In the stochastic model, however, shorter observation times are required to obtain quality reconstructions. As a result of these two conflicting requirements, the reconstruction error may be large for all observation times as shown in Figure 3.4.

## 3.5 Construction of Global Approximations Using Optimal Observation Times

The optimal observation time for each Fourier coefficient can be obtained by minimizing the MSE from the previous section; however, the MSE for the Fourier

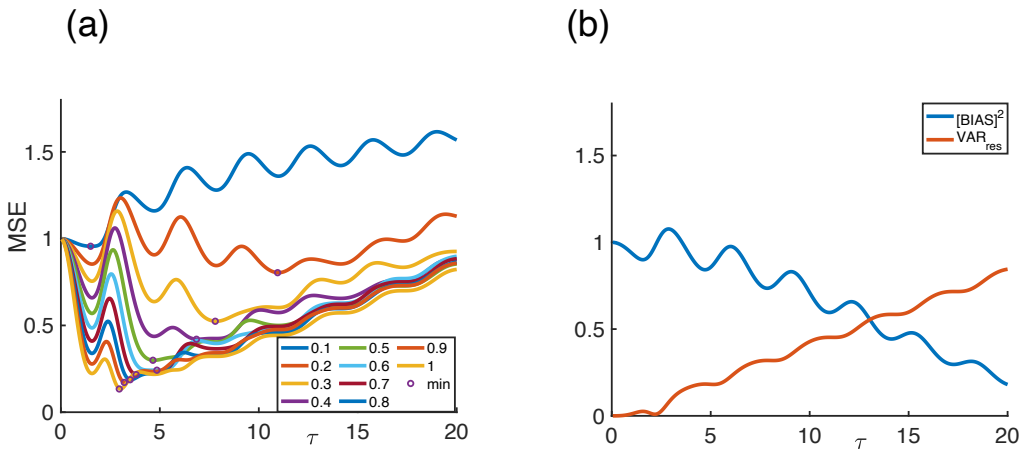


**Figure 3.4:** (a) MSE (3.74) versus observation time $\tau$ as a function of the difference $\omega_k - \omega_j$ between the frequency of interest $\omega_j$ and a secondary frequency $\omega_k$. The circles indicate the minimum MSE for each curve. (b) The MSE (3.74) is a sum of three terms: squared bias, resonant variance, and nonresonant variance. The squared bias (3.61) and resonant variance (3.65) versus observation time $\tau$ are displayed for the case where $\omega_k - \omega_j = 0.1$, corresponding to the top blue curve in (a). The coefficients are $\hat{f}_j = 1$, $\hat{f}_k = -1$ and the noise levels are $\sigma_j = 0.5$, $\sigma_k = 0.5$.

coefficient $\hat{f}_j$ depends on all of the other Fourier coefficients, and so the coefficients must be solved for iteratively using Algorithm 1. To illustrate the effectiveness of this method, we simulate the noisy sensor time series

$$\mathbf{R_s}(t) = \sum_n \mathbf{\Phi}_n(\mathbf{s})\hat{f}_n \cos(\sqrt{\lambda_n}t) + \sum_m \mathbf{\Phi}_m(\mathbf{s}) \int_0^t \cos(\sqrt{\lambda_m}(t-r))\sigma_m \mathcal{W}_m(r)\, dr, \tag{3.75}$$

construct a global approximation of the ensemble average electric field

$$\langle \mathbf{E} \rangle(\mathbf{x}, t) = \sum_n \mathbf{\Phi}_n(\mathbf{x})\hat{f}_n \cos(\sqrt{\lambda_n}t) \tag{3.76}$$

using Algorithm 1, and compare this result to the global approximation obtained using a longer observation time of $\tau_f = 40$. In this simulation, we consider a three-frequency signal, i.e., $n$ ranges over three values in (3.75) and (3.76), and the noise in the sensor time series is represented by a sum over the first 20 frequencies, meaning $m$ ranges from 1 to 20 where the eigenvalues $\lambda_m$ are ordered from smallest to largest.

**Algorithm 1** Optimal Observation Time for $N$ frequencies

$\hat{f}_{k_1}, ..., \hat{f}_{k_N} = 1$

**for** $I = 1 : iter$ **do**

  **for** $j = 1 : N$ **do**

    Simulate MSE$(\tau; k_j)$ (3.58) using $\hat{f}_{k_n}, n \neq j$

    Compute the $\tau$ that minimizes MSE$(\tau; k_j)$ using $\hat{f}_{k_n}, n \neq j$

    set $\hat{f}_{k_j} = \alpha_{k_j,i}(\tau)/(\Phi_{k_j,i}(\mathbf{s})D_{cc}(\tau; \sqrt{\lambda_{k_j}}, \sqrt{\lambda_{k_j}}))$

  **end for**

**end for**

For simplicity and illustration purposes, we reconstruct the first component of the ensemble average field $\langle E_1 \rangle$ at $\mathbf{x} = \mathbf{s}$ to compare to the original sensor time series. The eigenfunctions $\mathbf{\Phi}_n(\mathbf{x})$ are obtained from the eigenvalue problem (3.12) for the case of odd functions and with $\mu$ and $\epsilon$ constant.

Figure 3.5 displays the two approximations of $\langle E_1 \rangle$ at $\mathbf{x} = \mathbf{s}$ from $t = 0$ to $t = 40$ alongside the ensemble average field $\langle E_1 \rangle$ and the original sensor time series $R_{\mathbf{s},1}(t)$. The $L^2([0, \tau_f])$ relative error using the observation time $\tau_f = 40$ is 26.1% and using Algorithm 1 is 15.1%. This example shows that using optimal observation times provides a better reconstruction of the ensemble average signal.

## 3.6 Conclusion

In this chapter, we consider the optimal observing time for obtaining global information about electromagnetic waves from time series data obtained from a sensor at a fixed spatial location. The data obtained from one sensor can be used to predict that taken from another, and the results provide the theoretical basis for a cross-validation or error-correction scheme for a network of sensors. We show how to estimate the time-varying coefficients of the solution of the Maxwell vector wave equation from the

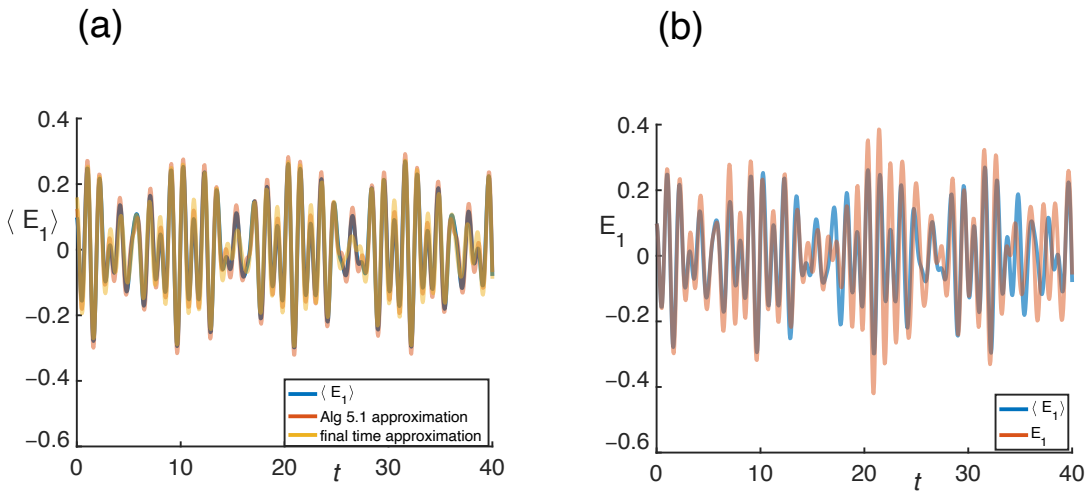


**Figure 3.5:** (a) Approximations of the ensemble average electric field $\langle E_1 \rangle$ (3.76) at $\mathbf{x} = \mathbf{s}$ obtained from noisy sensor data (3.75) using optimal observation time algorithm 1 (in red) and using the sensor time series data up to the time $\tau_f = 40$ (in yellow). The $L^2([0, \tau_f])$ relative errors in these approximations are 15.1% and 26.1% respectively. The ensemble average field $\langle E_1 \rangle$ is displayed in blue for comparison. (b) The noisy sensor data (3.75) (in red) and the ensemble average electric field (3.76) (in blue) at the location $\mathbf{x} = \mathbf{s}$.

time series and show that longer observation times do not in general provide more accurate estimates. The bias and variance of the estimates are derived analytically in important special cases. Although the bias decreases with time, the variance increases with time, leading to an "optimal" observing time that depends in part on the coefficients of interest. An iterative algorithm is presented to utilize the optimal observing times in the general case of $N$ frequencies, and the results of the algorithm in a three-frequency example are compared to those obtained from longer observing times.

Acknowledgments: This work was partially supported by the Air Force Office of Scientific Research under award number FA9550-23-1-0177. B.M.B. was partially supported by the School of Mathematical and Statistical Sciences at Arizona State University. The work described in this chapter was submitted for publication [6].

Chapter 4

# RECONSTRUCTION OF WAVE DYNAMICS FROM ACCELERATING SENSORS

## 4.1 Introduction

In this chapter, we consider the problem of reconstructing wave dynamics using time series data obtained from a sensor moving along a general trajectory $\mathbf{x}_s(t)$ in space. The underlying waves propagate in an inhomogeneous medium and are governed by the wave equation:

$$\frac{\partial^2 u}{\partial t^2} - c^2(\mathbf{x})\Delta u = 0 \tag{4.1}$$

where $c(\mathbf{x})$ is the variable wave speed. We observe the wave field from an accelerating sensor which moves along the spatial trajectory $\mathbf{x}_s(t)$ in some domain $\mathcal{D}$ giving the time series $R_s(t) = u(\mathbf{x}_s(t), t)$. The solution $u$ is a scalar wave field and so it can represent pressure, giving rise to acoustic waves, or a single component of the electric field, giving rise electromagnetic waves. The solution $u$ of (4.1) can be obtained by solving the associated eigenvalue problem:

$$\Delta\Phi + \lambda c^{-2}(\mathbf{x})\Phi = 0. \tag{4.2}$$

The eigenfunctions $\Phi_n$ of the Laplace operator form an orthonormal basis in $L^2(\mathcal{D})$ with weight $c^{-2}(\mathbf{x})$. We can write solutions in the form:

$$u(\mathbf{x}, t) = \sum_n A_n(t)\Phi_n(\mathbf{x}) \tag{4.3}$$

and solve the sequence of ODEs:

$$A_n'' + \lambda_n A_n = 0. \tag{4.4}$$

The solution $u$ can then be obtained from initial conditions:

$$u(\mathbf{x}, 0) = g(\mathbf{x}) \tag{4.5}$$

$$\frac{\partial u}{\partial t}(\mathbf{x}, 0) = h(\mathbf{x}) \tag{4.6}$$

giving

$$u(\mathbf{x}, t) = \sum_n A_n(t)\Phi_n(\mathbf{x}) \tag{4.7}$$

$$A_n(t) = \hat{g}_n \cos(\sqrt{\lambda_n}t) + \frac{\hat{h}_n}{\sqrt{\lambda_n}} \sin(\sqrt{\lambda_n}t). \tag{4.8}$$

Alternatively, the solution can be written as the real part of

$$u(\mathbf{x}, t) = \sum_n C_n \exp(-i\omega_n t)\, \Phi_n(\mathbf{x}), \quad C_n \in \mathbb{C} \tag{4.9}$$

where $\omega_n = \sqrt{\lambda_n}$ is the angular frequency.

To understand the issues encountered in signal processing when the sensor is accelerating, we consider a simple example. Suppose the sensor travels along the one dimensional trajectory $x_s(t) = a_0 t^2$ in a homogeneous medium. Since $c$ is constant, the solution can be written explicitly as

$$u(x, t) = \sum_n C_n \exp(i(k_n x - \omega_n t)) \tag{4.10}$$

and the resulting sensor time series is

$$R_s(t) = \sum_n C_n \exp\left(i(k_n a_0 t^2 - \omega_n t)\right). \tag{4.11}$$

Standard Fourier analysis of almost periodic signals suggests that we should compute:

$$\hat{R}_s(\omega) := \lim_{\tau \to \infty} \frac{1}{\tau} \int_0^\tau R_s(t) \exp(-i\omega t)\, dt. \tag{4.12}$$

The space of almost periodic functions $\mathcal{B}$ can be defined as the closure of the trigonometric polynomials

$$f(t) = \sum_{k=1}^{m} A_k \exp(i\omega_k t) \tag{4.13}$$

with respect to the uniform norm $||f||_\infty = \sup_t |f(t)|$, [2]. The space $\mathcal{B}$ can be metrized by the inner product

$$(f(t), g(t)) := \lim_{\tau\to\infty} \frac{1}{\tau} \int_0^\tau f(t)\overline{g(t)}\, dt \tag{4.14}$$

and contains the uncountable orthonormal set of functions $\{\exp(i\omega t) : \omega \in \mathbb{R}\}$ which makes $\mathcal{B}$ nonseparable. The closure of the trigonometric polynomials with respect to the inner product (4.14) is a nonseparable Hilbert space containing $\mathcal{B}$. For more details on almost periodic functions see [2].

For an almost periodic signal $R_0(t)$, the transformation $\hat{R}_0(\omega)$ provides the coefficients of the signal and the relevant frequencies because the basis $\{\exp(i\omega t) : \omega \in \mathbb{R}\}$ is orthogonal:

$$(\exp(i\omega_1 t), \exp(i\omega_2 t)) = \lim_{\tau\to\infty} \frac{1}{\tau} \int_0^\tau \exp(i\omega_1 t) \exp(-i\omega_2 t)\ dt = \mathbf{1}_{\{\omega_1=\omega_2\}} \tag{4.15}$$

where $\mathbf{1}_D$ is the indicator function for the set $D$. The signal $R_s(t)$, however, is a linear combination of functions of the form $\exp(i(ka_0t^2 - \omega t))$. The inner product of functions in the set $\{\exp(i\omega t^2) : \omega \in \mathbb{R}\}$ can be computed in terms of the Fresnel integral:

$$\begin{aligned}
(\exp(i\omega_1 t^2), \exp(i\omega_2 t^2)) &= \lim_{\tau\to\infty} \frac{1}{\tau} \int_0^\tau \exp(i\omega_1 t^2) \exp(-i\omega_2 t^2)\ dt && (4.16)\\
&= \lim_{\tau\to\infty} \frac{1}{\tau} \int_0^\tau \exp(i(\omega_1 - \omega_2)t^2)\ dt && (4.17)\\
&= \lim_{\tau\to\infty} \frac{1}{\tau} \frac{1}{\sqrt{\omega_1 - \omega_2}} \mathrm{Fr}(\sqrt{\omega_1 - \omega_2}\tau) && (4.18)\\
&= \mathbf{1}_{\{\omega_1=\omega_2\}}. && (4.19)
\end{aligned}$$

where

$$\begin{aligned}
\mathrm{Fr}(x) &= \int_0^x \exp(it^2)\ dt && (4.20)\\
&= \sqrt{\frac{\pi}{8}}(1+i)\mathrm{erf}\left(\frac{1-i}{\sqrt{2}}x\right) && (4.21)
\end{aligned}$$

is the Fresnel integral which is used in optics to study diffraction [9]. Generally, for the kernel $\kappa(t) = (at+b)^2 + \kappa_0$ we can write

$$\mathrm{Fr}_\kappa(x) = \int_0^x \exp\left(i\kappa(t)\right)\, dt \tag{4.22}$$

$$= \exp\left(i\kappa_0\right) \int_b^{ax+b} \frac{1}{a} \exp\left(ir^2\right)\, dr \tag{4.23}$$

$$= \frac{\exp\left(i\kappa_0\right)}{a} (\mathrm{Fr}(ax+b) - \mathrm{Fr}(b)). \tag{4.24}$$

For example, the time series $R_s(t)$ can be written in terms of the kernels:

$$\kappa_n(t) = \left(\sqrt{k_n a_0}t - \frac{\omega_n}{2\sqrt{k_n a_0}}\right)^2 - \frac{\omega_n^2}{4k_n a_0}. \tag{4.25}$$

For the kernel $\kappa(t) = (at+b)^2 + \kappa_0$ with $a \neq 0$, we compute:

$$\lim_{\tau\to\infty} \frac{1}{\tau}\mathrm{Fr}_\kappa(\tau) = \lim_{\tau\to\infty} \frac{1}{\tau}\frac{\exp\left(i\kappa_0\right)}{a}(\mathrm{Fr}(a\tau+b) - \mathrm{Fr}(b)) = 0. \tag{4.26}$$

Thus, the coefficients $C_n$ are not recovered using $\hat{R}_s(\omega)$. Traditional Fourier methods using the basis $\{\exp(i\omega t) : \omega \in \mathbb{R}\}$ cannot be used directly to analyze the time series $R_s(t)$. In the next section, we review the Doppler effect and describe a time transformation method that orthogonalizes the basis functions in special cases, allowing the use of the Fourier transform with a nonuniform sampling method. In section 4.3, we present a randomized algorithm to reconstruct the wave field $u$.

## 4.2 Reconstruction Using Time Transformations and the Doppler Effect

When the propagation medium is homogeneous, i.e., the wave speed $c$ is independent of $\mathbf{x}$, explicit transformations can be used because the wave field $u$ can be written explicitly:

$$u(\mathbf{x},t) = \int_{\mathbb{R}^3} \hat{u}(\mathbf{k}) \exp\left(i(\mathbf{k}\cdot\mathbf{x} - \omega t)\right)\, d^3\mathbf{k}. \tag{4.27}$$

If we consider solutions in the space of almost periodic functions, then the solution is

$$u(\mathbf{x}, t) = \sum_n C_n \exp\left(i(\mathbf{k}_n \cdot \mathbf{x} - \omega_n t)\right). \tag{4.28}$$

When the waves propagate in the same direction $\hat{\mathbf{k}}$, the sensor time series is

$$R_s(t) = \sum_n C_n \exp\left(i(\mathbf{k}_n \cdot \mathbf{x}_s(t) - \omega_n t)\right) = \sum_n C_n \exp\left(i\omega_n(c^{-1}\hat{\mathbf{k}} \cdot \mathbf{x}_s(t) - t)\right) \tag{4.29}$$

where $c = \frac{\omega_n}{|\mathbf{k}_n|}$. Thus, we can apply the transformation

$$\tilde{t} = t - c^{-1}\hat{\mathbf{k}} \cdot \mathbf{x}_s(t) \tag{4.30}$$

to obtain the new time series

$$R_s(\tilde{t}) = \sum_n C_n \exp\left(-i\omega_n \tilde{t}\right). \tag{4.31}$$

The Fourier transform can be readily applied to (4.31) to obtain the frequencies $\omega_n$ of the signal. For a discrete time series $R_s(t_i)$ with uniform sampling $t_i - t_{i-1} = \Delta t$, the transformed time series $R_s(\tilde{t}_i)$ will have nonuniform sampling; therefore, the nonuniform fast Fourier transform has to be used to analyze the signal. If the velocity of the sensor in the direction of wave propagation is less than the speed of the wave, i.e., $\hat{\mathbf{k}} \cdot \mathbf{v}(t) < c$ then the transformation (4.30) does not change the direction of time: $\frac{d\tilde{t}}{dt} > 0$. The effect of this time transformation method on the Fourier transform of the signal is illustrated in Figure 4.1. In the left panel, the peaks of the spectrum are blurred as a result of the accelerating sensor. This can be contrasted with the spectrum of a constant velocity sensor, where the peaks are merely shifted. The shifting of frequencies due to movement of the sensor is the well-studied Doppler effect [47, 23]. In the right panel, the original frequencies are recovered.

This can be generalized to the case where the direction of propagation is unknown or waves propagate in different directions. First, parameterize the direction of

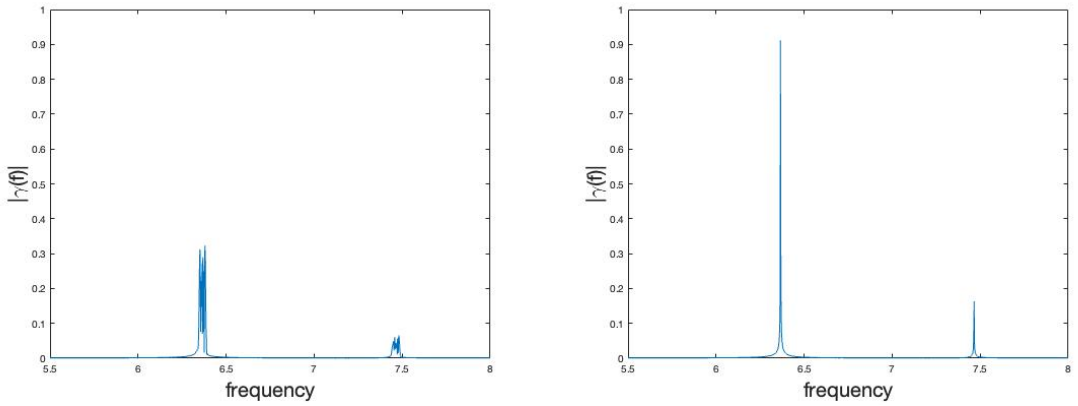


**Figure 4.1:** (left) The spectrum of a two frequency sensor time series $R_s(t)$ given by (4.29) where the sensor traverses a circle in the $x_1$-$x_3$ plane at a constant speed. (right) The spectrum of the same time series after applying the time transformation (4.30) to obtain (4.31). To obtain the spectrum in the right panel, a nonuniform FFT is used.

propagation. For example, in a two dimensional case:

$$\hat{\mathbf{k}}(\theta) = (\cos(\theta), \sin(\theta)), \quad \theta \in [0, 2\pi). \tag{4.32}$$

Consider the collection of transformations:

$$\tilde{t}_\theta = t - \frac{1}{c}\hat{\mathbf{k}}(\theta) \cdot \mathbf{x}_s(t). \tag{4.33}$$

Each transformation provides a new time series:

$$R_s(\tilde{t}_\theta) = \sum_n C_n \exp\left(i\omega_n \left(\frac{1}{c}\hat{\mathbf{k}}_n \cdot \mathbf{x}_s(t) - \frac{1}{c}\hat{\mathbf{k}}(\theta) \cdot \mathbf{x}_s(t) - \tilde{t}_\theta\right)\right) \tag{4.34}$$

and a corresponding Fourier transform. The resulting parameterized collection of Fourier transforms is plotted in Figure 4.2. Notice that varying the direction of propagation $\hat{\mathbf{k}}$ and varying the frequencies $\omega$ is equivalent to just varying $\mathbf{k}$. When $\hat{\mathbf{k}}(\theta) = \hat{\mathbf{k}}_n$, the frequency $\omega_n$ becomes unblurred in the amplitude spectrum as in Figure 4.1.

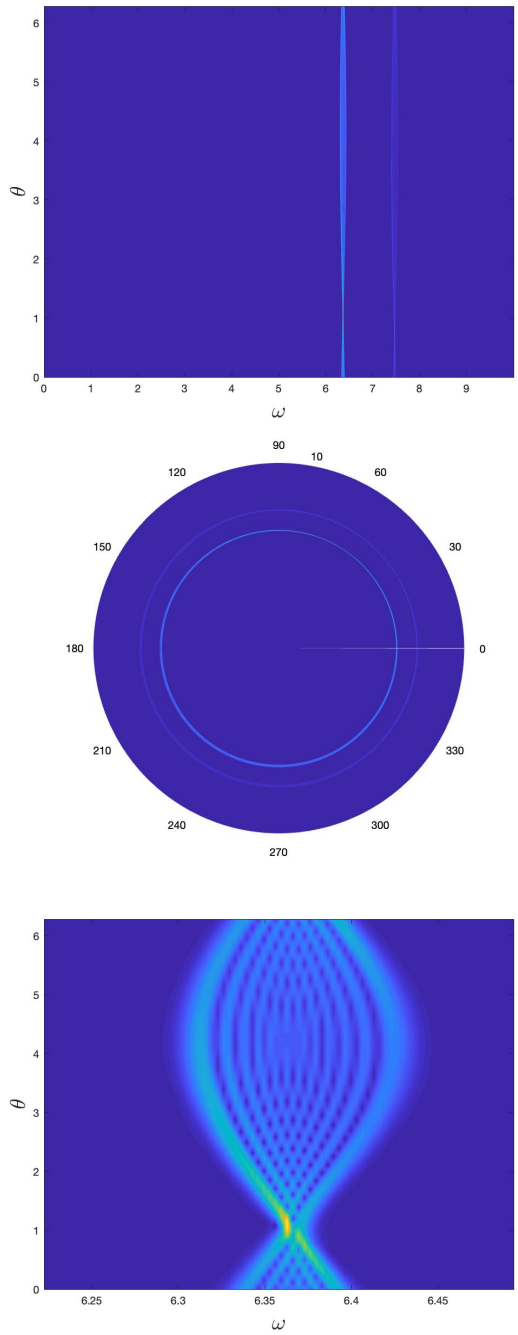


**Figure 4.2:** Parameterized collection of amplitude spectra of a two frequency sensor time series. For each fixed $\theta \in [0, 2\pi)$, the amplitude spectrum of (4.34) is plotted. The first and second panel display the same information in polar and Cartesian coordinates. The third panel displays the same plot as the first panel but zoomed in on a small frequency range. Each frequency of the original signal creates a ring in the second panel with its magnitude represented by the color in the plot. Each ring (in the second panel) is thinnest when $\hat{\mathbf{k}}(\theta)$ is pointing in the direction of propagation $\hat{\mathbf{k}}_n$ which can be seen most easily in the third panel.

## 4.3 Randomized Algorithm

In the previous section, we outlined a method for reconstructing the field $u$ from accelerating sensors utilizing an explicit closed-form solution of the field. In this section, we develop a method of reconstruction of $u$ that only relies on the decomposition of the field into eigenfunctions $\Phi_n$ of the weighted Laplace operator (4.9). With this method, the eigenfunctions can be computed numerically, as opposed to analytically as in the previous sections, and the medium can be inhomogeneous. In particular, we consider a randomized algorithm. One of the primary advantages of using a randomized algorithm is speed [42]. The sensor time series in this case is

$$R_s(t) = \sum_{n=1}^{N} C_n \exp\left(-i\omega_n t\right) \Phi_n(\mathbf{x}_s(t)). \tag{4.35}$$

Where $N$ is the number of dominant frequencies in the wave field. In general, the frequency information (the frequencies $\omega_n$ and the eigenfunctions $\Phi_n$) and the coefficients $C_n$ are unknown; however, we can utilize the Fourier transform and the maximum Doppler shift to obtain an initial bounded range of relevant frequencies.

### *4.3.1 The Doppler Window*

For general spatially-varying media, a representation of the electric field cannot be obtained except in special cases. We now consider general stratified media, represented by the wave speed $c(x_3)$, where an approximate explicit solution can be obtained. To derive this approximate solution, we need to solve the eigenvalue problem (4.2) with wave speed $c(x_3)$. Writing $\Phi(\mathbf{x}) = \alpha(x_1, x_2)\beta(x_3)$ separates (4.2) into two eigenvalue problems:

$$\Delta\alpha(x_1, x_2) + \xi\alpha(x_1, x_2) = 0 \tag{4.36}$$

$$\beta''(x_3) + (c^{-2}(x_3)\lambda - \xi)\beta(x_3) = 0. \tag{4.37}$$

If we consider solutions of the form $\beta(x_3) = \exp(b(x_3))$ where $b(x_3) = b_r(x_3) + ib_i(x_3)$ then we obtain a nonlinear ODE for $b(x_3)$:

$$b''(x_3) + (b'(x_3))^2 + (c^{-2}(x_3)\lambda - \xi) = 0 \tag{4.38}$$

that is an equation only in $b''$ and $b'$ but not $b$. So, we instead consider the transformation

$$\beta(x_3) = \exp\left(\int_0^{x_3} b(y)\, dy\right) \tag{4.39}$$

and the ODE for $b$ becomes the Riccati equation

$$b'(x_3) = -k_3^2(x_3) - b^2(x_3) \tag{4.40}$$

where

$$k_3^2(x_3) = c^{-2}(x_3)\lambda - \xi. \tag{4.41}$$

We use the conditions at $x_3 = 0$:

$$\beta(0) = 1 \tag{4.42}$$

$$\beta'(0) = -\frac{k_3'(0)}{2k_3(0)} + ik_3(0). \tag{4.43}$$

If we assume the wave speed $c(x_3)$ is slowly varying, then the WKB approximation can be used, reducing the Riccati equation (4.40) to

$$0 = -k_3^2(x_3) - b^2(x_3) \tag{4.44}$$

since $b' << 1$. This approximation method is similar to the Rytov approximation $\beta = \exp(\sum_n \psi_n)$ [31, 43]. The first order approximation is thus

$$b(x_3) = \pm ik_3(x_3) = \pm i\sqrt{c^{-2}(x_3)\lambda - \xi} \tag{4.45}$$

with derivative

$$b'(x_3) = \pm ik_3'(x_3) = \mp i\frac{c'(x_3)}{c(x_3)}\frac{c^{-2}(x_3)\lambda}{\sqrt{c^{-2}(x_3)\lambda - \xi}}. \tag{4.46}$$

To obtain a second approximation, substitute (4.46) into (4.40), obtaining an equation that is quadratic in $b$. Thus, we use the quadratic formula and a binomial expansion:

$$\begin{aligned} b(x_3) &= \pm\sqrt{-k_3^2(x_3) \mp ik_3'(x_3)} \\ &\approx \left( \pm ik_3(x_3) \pm \frac{ik_3'(x_3)}{i2k_3(x_3)} \right) \\ &\approx \pm\frac{k_3'(x_3)}{2k_3(x_3)} \pm ik_3(x_3). \end{aligned} \tag{4.47}$$

To obtain the approximate solution $\beta(x_3)$ to our eigenvalue problem, recall the transformation $\beta(x_3) = \exp\left(\int_0^{x_3} b(y)\,dy\right)$. We obtain

$$\beta(x_3) \approx \left(\frac{k_3(x_3)}{k_3(0)}\right)^{-1/2} \exp\left(\pm i\int_0^{x_3} k_3(y)\,dy\right). \tag{4.48}$$

Therefore, the approximate wave field (in two dimensions) is

$$u(\mathbf{x}, t) = \sum_n C_n \left(\frac{k_{n,3}(x_3)}{k_{n,3}(0)}\right)^{-1/2} \exp\left(i\left(k_{n,1}x_1 + \int_0^{x_3} k_{n,3}(y)\,dy - \omega_n t\right)\right). \tag{4.49}$$

Notice that $k_{n,3}(x_3)$ implicitly depends on $\omega_n = \sqrt{\lambda_n}$ since $k_{n,3}(x_3) = \sqrt{c^{-2}(x_3)\lambda_n - \xi_n}$.

The sensor time series $R_s(t)$ along the trajectory $\mathbf{x}_s(t)$, using the WKB approximation, is

$$R_s(t) = \sum_n C_n \left(\frac{k_{n,3}(x_3(t))}{k_{n,3}(0)}\right)^{-1/2} \exp\left(i\left(k_{n,1}x_1(t) + \int_0^{x_3(t)} k_{n,3}(y)\,dy - \omega_n t\right)\right) \tag{4.50}$$

$$= \sum_n C_n \exp\left(\gamma_n(t) + i\eta_n(t)\right) \tag{4.51}$$

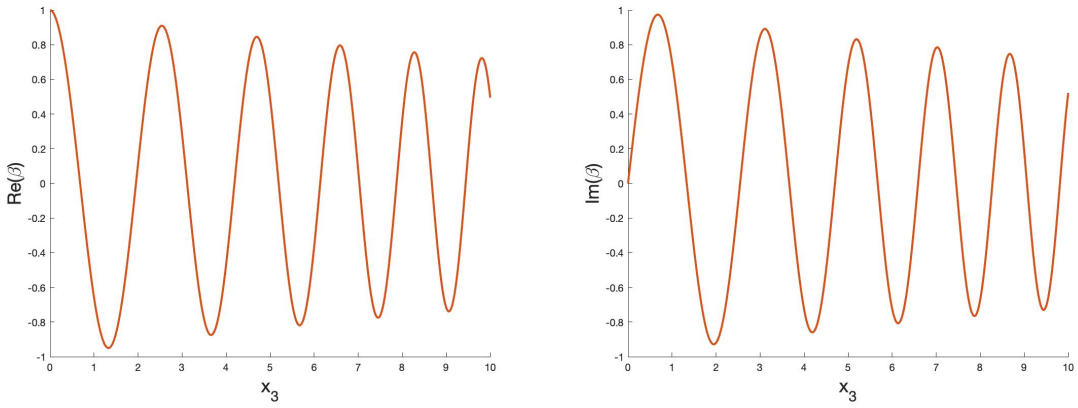


**Figure 4.3:** Comparison of simulated $\beta(x_3)$ to the WKB approximation of $\beta(x_3)$. The curves are practically indistinguishable. On the left the real part of $\beta$ is plotted for both the simulated and WKB solution. Similarly, the imaginary part is plotted on the right. The wave speed profile is $c(x_3) = c_0 \exp(\gamma x_3)$.

where

$$\eta_n(t) = k_{n,1}x_1(t) + \int_0^{x_3(t)} k_{n,3}(y)\,dy - \omega_n t. \tag{4.52}$$

For simplicity, assume the sensor trajectory begins at the origin: $\mathbf{x}_s(0) = \mathbf{0}$. If we apply the Fourier transform to this time series, the peaks of the amplitude spectrum will be shifted as a result of the fact that $\eta_n(t) \neq -\omega_n t$. Instead, the frequencies $\tilde{\omega}$ given by the Fourier transform of $\exp(i\eta_n(t))$ will belong to some range $(1-\zeta_-)\omega_n \leq \tilde{\omega} \leq (1+\zeta_+)\omega_n$. Observe

$$1 - \zeta_- = 1 - \frac{1}{\omega_n t}\left(k_{n,1}x_1(t) + \int_0^{x_3(t)} k_{n,3}(y)\,dy\right) \tag{4.53}$$

$$\geq 1 - \frac{1}{\omega_n t}\left(k_{n,1}x_1(t) + x_3(t)\tilde{k}_{n,3}(y)\right) \tag{4.54}$$

$$\geq 1 - \frac{|\tilde{\mathbf{k}}_n|}{\omega_n}\frac{|\mathbf{x}(t)|}{t} \tag{4.55}$$

$$\geq 1 - \frac{\tilde{v}}{\tilde{c}} \tag{4.56}$$

where $\tilde{k}_{n,i}$ and $\tilde{v}$ are the maximum values of $k_{n,i}(x_3)$ and $|\mathbf{v}(t)|$ along the trajectory $\mathbf{x}_s(t)$ and $\tilde{c}$ is the minimum value of $c(x_3)$ along the trajectory. The calculation of

$\zeta_+$ is similar. Thus, the peaks of the Fourier transform of the signal $\exp(i\eta_n(t))$ corresponding to the frequency $\omega_n$ will appear in the Doppler window

$$\left[\left(1-\frac{\tilde{v}}{\tilde{c}}\right)\omega_n, \left(1+\frac{\tilde{v}}{\tilde{c}}\right)\omega_n\right] \tag{4.57}$$

and we define the maximum shift $\tilde{\zeta} := \tilde{v}/\tilde{c}$.

### *4.3.2 Randomized Algorithm*

We now describe the randomized algorithm used to obtain the vector of complex coefficients $\mathbf{C} = (C_1, ..., C_N)$ and the corresponding frequencies $\omega_1, ..., \omega_N$. In this algorithm, we focus on wave fields where waves propagate in the same direction $\hat{\mathbf{k}}$; however, the algorithm can be easily extended to waves propagating in different directions. We are given a time series at the discrete times $t_1 = 0, ..., t_N = \tau$:

$$R_s(t_j) = \sum_{n=1}^{N} C_n \exp(-i\omega_n t_j)\, \Phi_n(\mathbf{x}_s(t_j)), \quad j = 1, ..., J. \tag{4.58}$$

We first apply the fast Fourier transform to $\{R_s(t_j)\}_{j=1}^{J}$ to obtain the frequencies $\tilde{\omega}_m$ where the peaks of the spectrum occur. From the analysis in the previous subsection, we know that these frequencies will not be the frequencies of interest $\omega_n$. Instead, the frequencies $\tilde{\omega}_m$ belong to the band (4.57) around each $\omega_n$. Thus, the frequencies of interest $\omega_n$ belong to the set

$$\Omega = \bigcup_m \left[\left(1+\tilde{\zeta}\right)^{-1}\tilde{\omega}_m, \left(1-\tilde{\zeta}\right)^{-1}\tilde{\omega}_m\right]. \tag{4.59}$$

Now that we have identified a range of frequencies to consider for reconstruction of the field, the randomized algorithm can be summarized as follows: (1) select $N$ frequencies from $\Omega$ uniformly at random:

$$\omega_1, ..., \omega_N \sim \text{Unif}(\Omega) \tag{4.60}$$

(to extend this algorithm to wave fields with arbitrary directions of propagation, the directions of wave propagation will also need to be selected uniformly at random); (2) simulate the corresponding eigenfunctions $\Phi_n(\mathbf{x})$ from (4.2); (3) construct the matrix

$$M_{j,n} = \exp\left(-i\omega_n t_j\right) \Phi_n(\mathbf{x}(t_j)); \tag{4.61}$$

(4) compute the least squares fit for the coefficients $C_n$:

$$\tilde{\mathbf{C}} = (M^T M)^{-1} M^T \mathbf{R} \tag{4.62}$$

where $R_j = R_s(t_j)$; (5) repeat this process $P$ times. Finally, select the resulting estimated time series:

$$\tilde{R}_s(t_j) = (M\tilde{\mathbf{C}})_j = \sum_{n=1}^{N} \tilde{C}_n \exp\left(-i\omega_n t_j\right) \Phi_n(\mathbf{x}_s(t_j)), \quad j = 1, ..., J \tag{4.63}$$

with the lowest relative root mean squared error:

$$\text{RMSE}(\tau) := \left( \frac{\sum_{j=1}^{J} (\tilde{R}_j - R_j)^2}{\sum_{j=1}^{J} R_j^2} \right)^{1/2}. \tag{4.64}$$

The resulting approximate wave field at any location $\mathbf{x}_a$ is

**Algorithm 2** Randomized Algorithm

**for** $p = 1 : P$ **do**

  **for** $n = 1 : N$ **do**

    sample $\omega_n$ from Unif($\Omega$)

    simulate solution $\Phi_n(\mathbf{x})$ of (4.2)

  **end for**

  construct the matrix $M$ (4.61)

  calculate least squares coefficients $\tilde{\mathbf{C}}$ (4.62)

  calculate relative RMSE (4.64)

**end for**

$$u(\mathbf{x}_a, t) = \sum_{n=1}^{N} \tilde{A}_n \exp(-i\omega_n t) \tag{4.65}$$

where $\tilde{A}_n = \tilde{C}_n \Phi_n(\mathbf{x}_a)$.

## 4.4 Analysis of Algorithm and Examples

In this section, we illustrate the effectiveness of Algorithm 2 through two important examples and we analyze the accuracy of the algorithm through simulations.

### *4.4.1 Examples*

We look at two different sensor trajectories: acceleration in a straight line and acceleration in a circle. We simulate the field

$$u(\mathbf{x}, t) = C_1 \exp(-i\omega_1 t)\, \Phi_1(\mathbf{x}) + C_2 \exp(-i\omega_2 t)\, \Phi_2(\mathbf{x}) \tag{4.66}$$

in the $x_1$-$x_3$ plane with the wave speed $c(x_3) = c_0 \exp(\gamma x_3)$ and generate the sensor time series $R_s(t)$ along a trajectory $\mathbf{x}_s(t)$. The first trajectory $\mathbf{x}_s(t)$ is a circle with constant speed. The results of Algorithm 2 for this case are displayed in Figure 4.4. In the top right panel, we see that the two frequencies $\omega_1$ and $\omega_2$ are blurred as a result of the circular trajectory. For comparison, we also display the spectrum of the time series obtained from a sensor at the fixed location $\mathbf{x}_s(0)$:

$$R_0(t) = C_1 \exp(-i\omega_1 t)\, \Phi_1(\mathbf{x}_s(0)) + C_2 \exp(-i\omega_2 t)\, \Phi_2(\mathbf{x}_s(0)). \tag{4.67}$$

For the signal $R_0(t)$, the maximum Doppler shift is zero and so the exact frequencies $\omega_1$ and $\omega_2$ are trivially obtained from Algorithm 2. The bottom panel shows the resulting time series of Algorithm 2 which is practically indistinguishable from the original sensor time series. The second trajectory is a straight line with constant acceleration shown in Figure 4.5. In this case, the peaks of the spectrum are blurred and shifted.

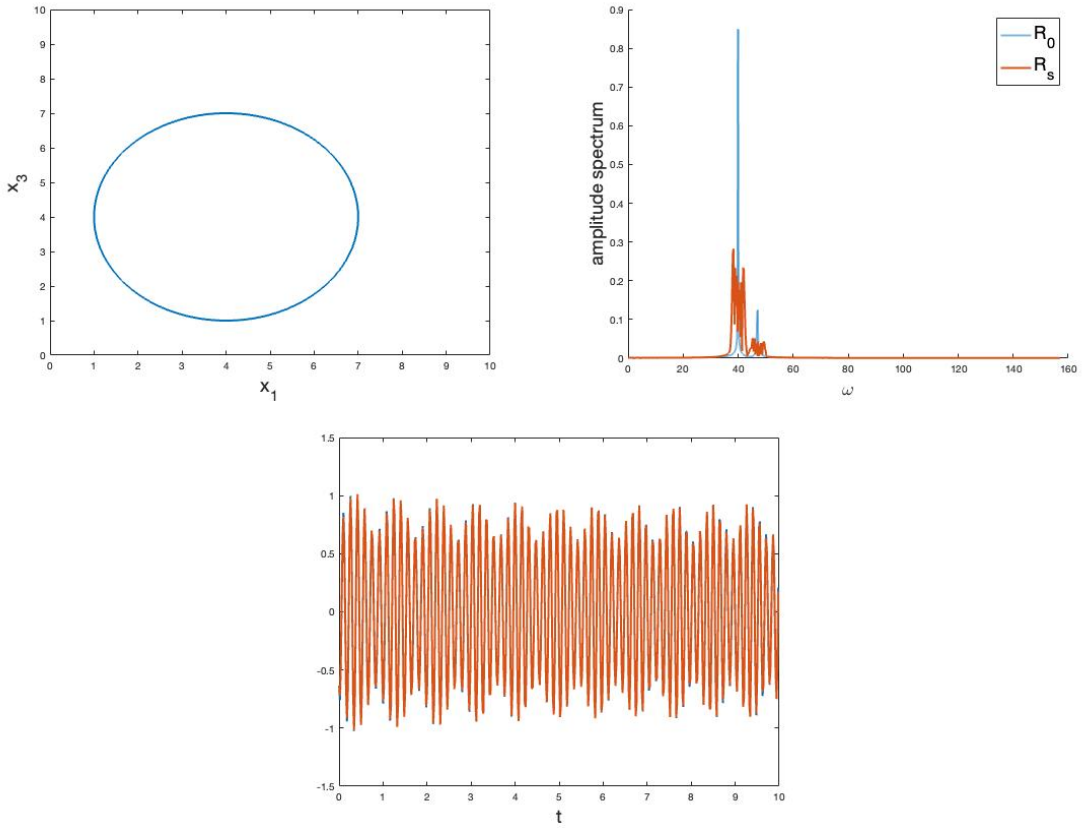


**Figure 4.4:** Reconstruction of the two-frequency sensor time series $R_s(t)$. (top left) The sensor trajectory $\mathbf{x}_s(t)$ in the $x_1$-$x_3$ plane. (top right) The single-sided amplitude spectrum of the time series $R_s(t)$. (bottom) The original time series $R_s(t)$ in blue and the reconstructed time series $\tilde{R}_s(t)$ using Algorithm 2 in red. Because the sensor trajectory $\mathbf{x}_s(t)$ is a circle, the two frequencies in the spectrum are blurred.

As in the first case, the approximate sensor time series $\tilde{R}_s(t)$ is similar to the original time series $R_s(t)$. More general smooth trajectories in two and three dimensions can be generated using Bézier curves which are sums of Bernstein polynomials weighted by control points in space [12, 44].

### *4.4.2 Analysis of Algorithm*

Since Algorithm 2 selects the frequencies $\omega$ from $\Omega$ uniformly at random, the accuracy of the algorithm can be described in terms of the probability of receiving a successful result after $P$ trials. Given a maximum acceptable relative RMSE $E$, the

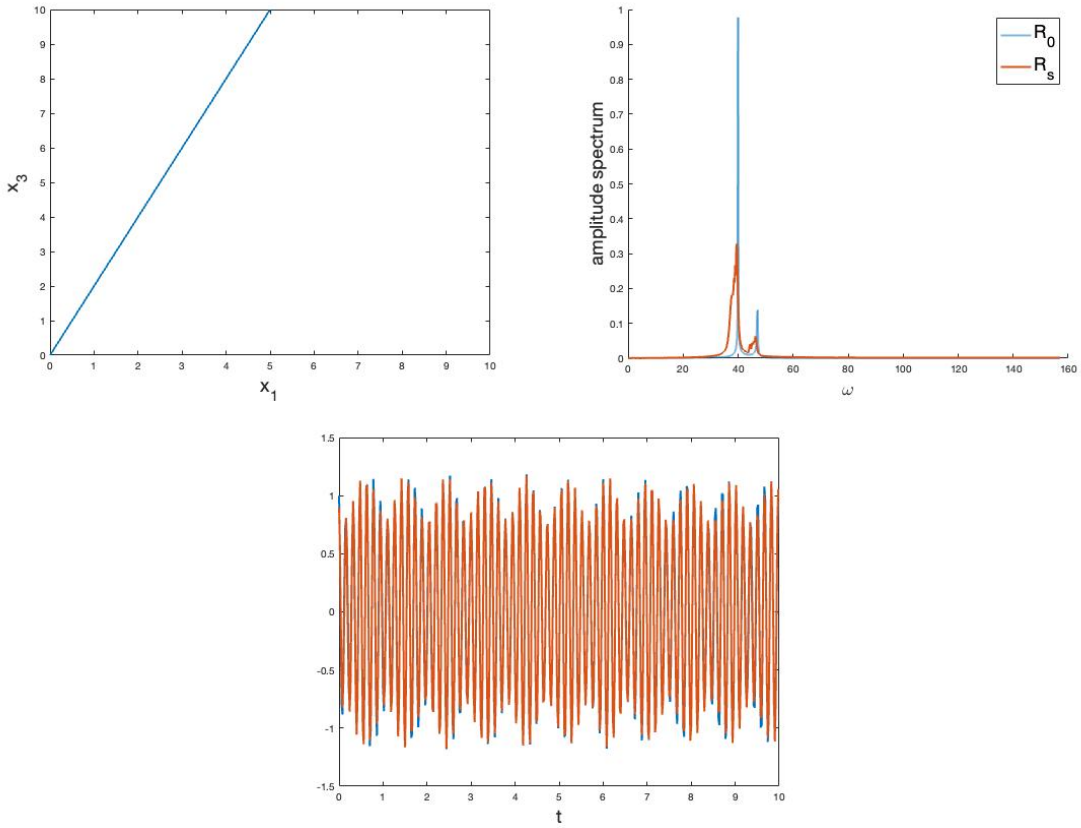


**Figure 4.5:** Reconstruction of the two-frequency sensor time series $R_s(t)$. (top left) The sensor trajectory $\mathbf{x}_s(t)$ in the $x_1$-$x_3$ plane. (top right) The single-sided amplitude spectrum of the time series $R_s(t)$. (bottom) The original time series $R_s(t)$ in blue and the reconstructed time series $\tilde{R}_s(t)$ using Algorithm 2 in red. Because the sensor trajectory $\mathbf{x}_s(t)$ is a line, the two frequencies in the spectrum are blurred and shifted.

probability of success from one trial is simply the fraction of the frequencies in the domain $\Omega$ that provide a relative RMSE less than $E$. If we call this fraction $\Omega_E$, then the probability of success after $P$ trials is

$$1 - (1 - \Omega_E)^P. \tag{4.68}$$

Figure 4.6 shows how $\Omega_E$ depends on the length $\tau$ of the time series $R_s(t)$ and on the maximum Doppler shift $\tilde{\zeta}$. When $\tilde{\zeta}$ is doubled in Figure 4.6, the fraction $\Omega_E$ is approximately halved.

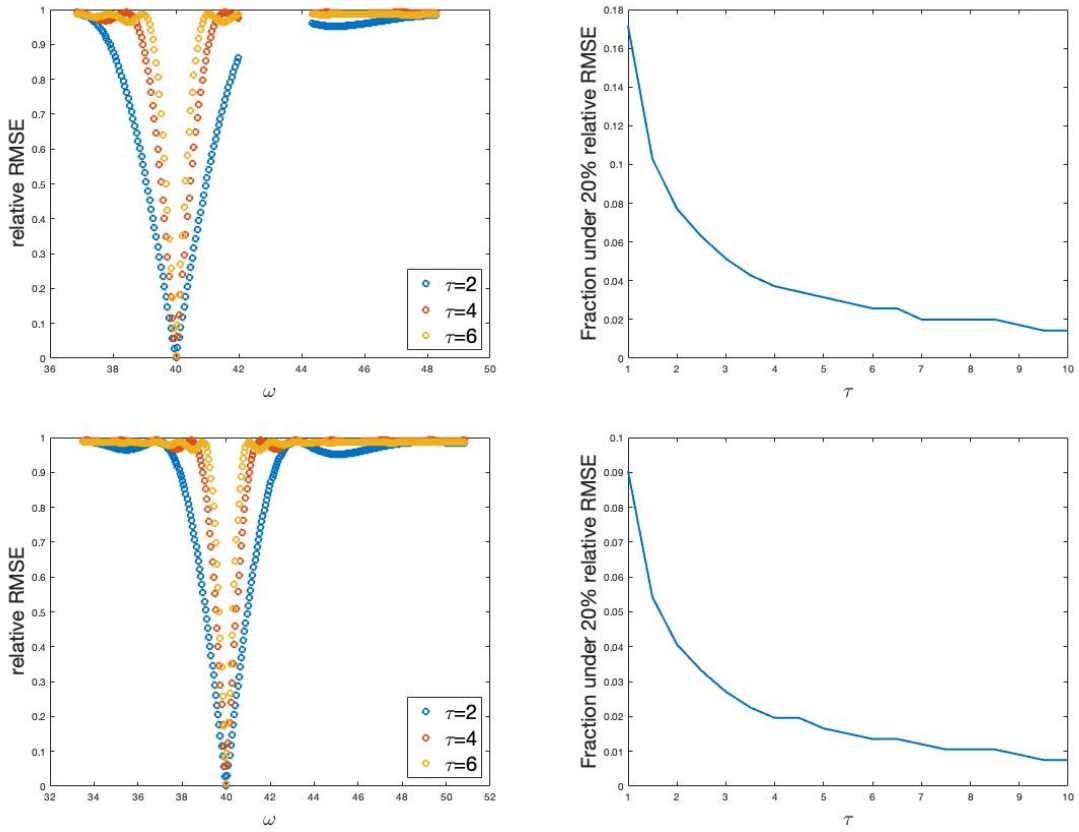


**Figure 4.6:** Relative RMSE as a function of the length $\tau$ of the time series $R_s(t)$ used for reconstruction. (top left) Relative RMSE is plotted against $\omega \in \Omega$ for different lengths $\tau$ of the time series $R_s(t)$. (top right) The fraction of reconstructions from the top left panel that have relative RMSE less than 20% as a function of the length of the time series $\tau$. The bottom two panels display the same information as the top two panels but for a sensor moving at twice the speed. The sensor trajectory is a line as in Figure 4.5.

## 4.5 Discussion and Future Work

In this work, we considered a random frequency algorithm to analyze and reconstruct wave fields from an accelerating sensor moving in an inhomogeneous medium. Obtaining the frequencies of a wave field from an accelerating frame of reference is, in general, a difficult problem because the Fourier basis in an accelerating reference frame is no longer orthogonal. The randomized algorithm we presented mitigates this issue by limiting the scope of possible frequencies to consider and randomly sampling

from this range until the desired error tolerance is reached. We also showed that the algorithm works in practice by simulating several important examples. In future work, we would like to tackle this issue with other methods such as the transformation method we discussed in section 4.2 (applied in the context of inhomogeneous media) or averaging methods.

# Chapter 5

# CONCLUSION

In this dissertation, we have provided fundamental results for analyzing wave dynamics using the mathematical theory of hyperbolic PDEs and sensor data. We investigated three major questions in chapters 2, 3, and 4 and presented several algorithms to analyze time series data obtained from noisy sensors that observe wave fields which are governed by the inhomogeneous wave equation and by the Maxwell vector wave equation.

We first looked at how to approximate global wave field information (such as frequencies and amplitudes of waves) from time series data obtained from a network of fixed-location sensors. The wave field information was then used to construct an approximate global wave field. We found that multiple sensors are usually required to provide a global approximation of the wave field since the information obtained from individual sensors is sensitive to perturbations in sensor location.

Next, we considered how to estimate the global electric field from a fixed-location sensor in the presence of a stochastic current density. We showed that, as a result of the bias-variance tradeoff, longer sensor observation times do not necessarily provide a more accurate estimate of the electric field. We then showed how to obtain the optimal observation time and how to utilize it to obtain a global estimate of the electric field.

Lastly, we considered how to obtain global approximations of wave fields when sensors are accelerating. Conventional Fourier analysis and data sampling methods fail to provide accurate estimates of the frequency and amplitude information of the underlying wave field in this case. We developed a new analytical approach and

implemented a randomized algorithm to obtain the frequencies of the wave field and a global representation thereof.

The work presented in this dissertation can be extended in several ways. For accelerating sensors, the governing equations were assumed to be noiseless, so we could consider how noise in the inhomogeneous wave equation would affect the global approximations obtained from accelerating sensors. In future work, we will extend this method to stochastic PDEs and further develop the theory of stochastic Maxwell's equations including weakly nonlinear regimes.

REFERENCES


[1] Henry Abarbanel. *Analysis of observed chaotic data*. Springer Science & Business Media, New York, 2012.

[2] N I Akhiezer and I M Glazman. *Theory of linear operators in Hilbert space*. Frederick Ungar Publishing Co., 1961.

[3] Andrea Alu. Extreme control of light and sound waves with metamaterials. Simons Foundation Presidential Lectures, 2023.

[4] N V Bakhmet'eva, V V Belikovich, L M Kagan, and A A Ponyatov. Sunset-sunrise characteristics of sporadic layers of ionization in the lower ionosphere observed by the method of resonance scattering of radio waves from artificial periodic inhomogeneities of the ionospheric plasma. *Radiophysics and Quantum Electronics*, 48(1):14–28, 2005.

[5] Bryce M Barclay, Eric J Kostelich, and Alex Mahalov. Sensor placement sensitivity and robust reconstruction of wave dynamics from multiple sensors. *SIAM Journal on Applied Dynamical Systems*, 21(4):2297–2313, 2022.

[6] Bryce M Barclay, Eric J Kostelich, and Alex Mahalov. Optimal observation time for solutions to the stochastic maxwell vector wave equation. Submitted 2023.

[7] Paul H Bezandry and Toka Diagana. *Almost periodic stochastic processes*. Springer Science & Business Media, 2011.

[8] Space Studies Board, National Research Council, et al. *Solar and space physics: A science for a technological society*. National Academies Press, 2013.

[9] Max Born and Emil Wolf. *Principles of optics: electromagnetic theory of propagation, interference and diffraction of light*. Cambridge University Press, 7th edition, 1999.

[10] Emmanuel J Candes, Justin K Romberg, and Terence Tao. Stable signal recovery from incomplete and inaccurate measurements. *Communications on Pure and Applied Mathematics: A Journal Issued by the Courant Institute of Mathematical Sciences*, 59(8):1207–1223, 2006.

[11] Bin Cheng and Zisis N Sakellaris. Near resonant approximation of the rotating stratified boussinesq system on a 3-torus. *Physica D: Nonlinear Phenomena*, 444:133588, 2023.

[12] Ji-wung Choi, Renwick Curry, and Gabriel Elkaim. Path planning based on Bézier curve for autonomous ground vehicles. In *Advances in Electrical and Electronics Engineering-IAENG Special Edition of the World Congress on Engineering and Computer Science 2008*, pages 158–166. IEEE, 2008.

[13] Giuseppe Da Prato and Jerzy Zabczyk. *Stochastic equations in infinite dimensions*. Cambridge University Press, Cambridge, United Kingdom, 2nd edition, 2014.

[14] Charles B Delahunt and J Nathan Kutz. A toolkit for data-driven discovery of governing equations in high-noise regimes. *IEEE Access*, 10:31210–31234, 2022.

[15] Alireza Doostan and Houman Owhadi. A non-adapted sparse approximation of pdes with stochastic inputs. *Journal of Computational Physics*, 230(8):3015–3034, 2011.

[16] Juan A Durazo, Eric J Kostelich, and Alex Mahalov. Local ensemble transform kalman filter for ionospheric data assimilation: Observation influence analysis during a geomagnetic storm event. *Journal of Geophysical Research: Space Physics*, 122(9):9652–9669, 2017.

[17] N Benjamin Erichson, Lionel Mathelin, J Nathan Kutz, and Steven L Brunton. Randomized dynamic mode decomposition. *SIAM Journal on Applied Dynamical Systems*, 18(4):1867–1891, 2019.

[18] Nasim Mohammadi Estakhri and Andrea Alu. Wave-front transformation with gradient metasurfaces. *Physical Review X*, 6(4):041008, 2016.

[19] Shima Fardad and Alessandro Salandrino. Plasmonic parametric absorbers. *Optics Letters*, 43(24):6013–6016, 2018.

[20] Xiaoli Feng, Meixia Zhao, Peijun Li, and Xu Wang. An inverse source problem for the stochastic wave equation. *Inverse Problems and Imaging*, 16(2):397–415, 2022.

[21] Franco Flandoli and Alex Mahalov. Stochastic three-dimensional rotating Navier–Stokes equations: averaging, convergence and regularity. *Archive for Rational Mechanics and Analysis*, 205:195–237, 2012.

[22] Mathieu Francoeur and M Pinar Mengüç. Role of fluctuational electrodynamics in near-field radiative heat transfer. *Journal of Quantitative Spectroscopy and Radiative Transfer*, 109(2):280–293, 2008.

[23] Bruce A Garetz. Angular doppler effect. *JOSA*, 71(5):609–611, 1981.

[24] Yoshikazu Giga, Alex Mahalov, and Basil Nicolaenko. *Mathematical Aspects of Nonlinear Dispersive Equations*, chapter The Cauchy problem for the Navier–Stokes equations with spatially almost periodic initial data, pages 213–222. Number 163. Princeton University Press, 2007.

[25] Mikhail Gilman, Erick Smith, and Semyon Tsynkov. *Transionospheric synthetic aperture imaging*. Birkhäuser, Cham, Switzerland, 2017.

[26] Moshe Gitterman. Classical harmonic oscillator with multiplicative noise. *Physica A: Statistical Mechanics and its Applications*, 352(2-4):309–334, 2005.

[27] Moshe Gitterman. *The Noisy Oscillator: The First Hundred Years, From Einstein Until Now*. World Scientific, Singapore, 2005.

[28] Yanqiu Guo and Edriss S Titi. Persistency of analyticity for nonlinear wave equations: An energy-like approach. *Bulletin of the Institute of Mathematics Academia Sinica*, 8(4):445–479, 2013.

[29] Abolfazl Hashemi, Hayden Schaeffer, Robert Shi, Ufuk Topcu, Giang Tran, and Rachel Ward. Generalization bounds for sparse random feature expansions. *Applied and Computational Harmonic Analysis*, 62:310–330, 2023.

[30] Forough Hassanibesheli, Niklas Boers, and Jürgen Kurths. Reconstructing complex system dynamics from time series: a method comparison. *New Journal of Physics*, 22(7):073053, 2020.

[31] Akira Ishimaru. *Wave propagation and scattering in random media*. Wiley-IEEE Press, 1997.

[32] Ahan Kak and Ian F Akyildiz. Designing large-scale constellations for the internet of space things with cubesats. *IEEE Internet of Things Journal*, 8(3):1749–1768, 2020.

[33] Holger Kantz and Thomas Schreiber. *Nonlinear time series analysis*. Cambridge University Press, Cambridge, United Kingdom, 2nd edition, 2004.

[34] Michael C Kelley. *The Earth's ionosphere: Plasma physics and electrodynamics*. Academic Press, Burlington, MA, 2009.

[35] Charles A Langston. Spatial gradient analysis for linear seismic arrays. *Bulletin of the Seismological Society of America*, 97(1B):265–280, 2007.

[36] Gi-Ren Liu. Stochastic wave propagation in Maxwell's equations. *Journal of Statistical Physics*, 158(5):1126–1146, 2015.

[37] Shukai Ma, Sendy Phang, Zachary Drikas, Bisrat Addissie, Ronald Hong, Valon Blakaj, Gabriele Gradoni, Gregor Tanner, Thomas M Antonsen, Edward Ott, et al. Efficient statistical model for predicting electromagnetic wave distribution in coupled enclosures. *Physical Review Applied*, 14(1):014022, 2020.

[38] Alex Mahalov and Austin McDaniel. Long-range propagation through inhomogeneous turbulent atmosphere: Analysis beyond phase screens. *Physica Scripta*, 94(3):034003, 2019.

[39] Sylvain Mangiarotti and Mireille Huc. Can the original equations of a dynamical system be retrieved from observational time series? *Chaos: An Interdisciplinary Journal of Nonlinear Science*, 29(2):023133, 2019.

[40] Krithika Manohar, Bingni W Brunton, J Nathan Kutz, and Steven L Brunton. Data-driven sparse sensor placement for reconstruction: Demonstrating the benefits of exploiting known patterns. *IEEE Control Systems Magazine*, 38(3):63–86, 2018.

[41] Austin McDaniel and Alex Mahalov. Coupling of paraxial and white-noise approximations of the helmholtz equation in randomly layered media. *Physica D: Nonlinear Phenomena*, 409:132491, 2020.

[42] Rajeev Motwani and Prabhakar Raghavan. *Randomized algorithms*. Cambridge University Press, 1995.

[43] Guy Potvin. General rytov approximation. *JOSA A*, 32(10):1848–1856, 2015.

[44] Hartmut Prautzsch, Wolfgang Boehm, and Marco Paluszny. *Bézier and B-spline techniques*, volume 6. Springer, 2002.

[45] Holger Rauhut and Rachel Ward. Sparse legendre expansions via $\ell_1$-minimization. *Journal of Approximation Theory*, 164(5):517–533, 2012.

[46] Alessandro Salandrino. Plasmonic parametric resonance. *Physical Review B*, 97(8):081401, 2018.

[47] N Seddon and T Bearpark. Observation of the inverse doppler effect. *Science*, 302(5650):1537–1540, 2003.

[48] Stephen R Shaffer and Alex Mahalov. Permittivity gradient induced depolarization: Electromagnetic propagation with the Maxwell vector wave equation. *IEEE Transactions on Antennas and Propagation*, 69(3):1553–1559, 2020.

[49] Ljubisa Stankovic. Performance analysis of the adaptive algorithm for bias-to-variance tradeoff. *IEEE Transactions on Signal Processing*, 52(5):1228–1234, 2004.

[50] Ke-Gang Wang and Jaume Masoliver. Linear oscillators driven by gaussian colored noise: crossovers and probability distributions. *Physica A: Statistical Mechanics and its Applications*, 231(4):615–630, 1996.

[51] Norbert Wiener. *Extrapolation, interpolation, and smoothing of stationary time series: with engineering applications*. MIT Press, Cambridge, MA, 1949.

# APPENDIX A

# COVARIANCE CALCULATIONS

## Covariance of $\boldsymbol{\alpha}_j$ and $\boldsymbol{\beta}_j$

In this section we provide more detail for the derivation of $\mathrm{COV}[\boldsymbol{\alpha}_j(\tau)]$. As in section 3.4.1, the covariance can be written as

$$\begin{aligned}
&\mathrm{COV}\left[\frac{1}{\tau}\int_0^\tau \mathbf{R}_{\mathbf{s}}(t)\cos(\sqrt{\lambda_j}\,t)\,dt\right] \qquad (A.1)\\
&= \boldsymbol{\Phi}_j(\mathbf{s})\boldsymbol{\Phi}_j^T(\mathbf{s})\mathbb{E}\left[\left(\frac{1}{\tau}\int_0^\tau\int_0^t \frac{\sigma_j}{\sqrt{\lambda_j}}\sin(\sqrt{\lambda_j}(t-r))\,d\mathcal{W}_j(r)\cos(\sqrt{\lambda_j}\,t)\,dt\right)^2\right]\\
&= \boldsymbol{\Phi}_j(\mathbf{s})\boldsymbol{\Phi}_j^T(\mathbf{s})\frac{\sigma_j^2}{\lambda_j\tau^2}\int_0^\tau\int_0^\tau \mathbb{E}\left[\left(\int_0^{t_1}\sin(\sqrt{\lambda_j}(t_1-r_1))\cos(\sqrt{\lambda_j}\,t_1)\,d\mathcal{W}_j(r_1)\right)\right.\\
&\left.\times\left(\int_0^{t_2}\sin(\sqrt{\lambda_j}(t_2-r_2))\,\cos(\sqrt{\lambda_j}\,t_2)\,d\mathcal{W}_j(r_2)\right)\right]dt_1dt_2.
\end{aligned}$$

We now use the trigonometric difference formula for sine and the identity (3.36) to split the variance into four terms:

$$\begin{aligned}
\frac{\sigma_j^2}{\lambda_j\tau^2}\int_0^\tau\int_0^\tau\int_0^{t_1\wedge t_2} &\Big(\sin(\sqrt{\lambda_j}t_1)\cos(\sqrt{\lambda_j}r)\cos(\sqrt{\lambda_j}t_1) \qquad (A.2)\\
&\quad-\cos(\sqrt{\lambda_j}t_1)\sin(\sqrt{\lambda_j}r)\cos(\sqrt{\lambda_j}t_1)\Big)\\
&\times\Big(\sin(\sqrt{\lambda_j}t_2)\cos(\sqrt{\lambda_j}r)\cos(\sqrt{\lambda_j}t_2)\\
&\quad-\cos(\sqrt{\lambda_j}t_2)\sin(\sqrt{\lambda_j}r)\cos(\sqrt{\lambda_j}t_2)\Big)\,dr\,dt_1\,dt_2.
\end{aligned}$$

The first term of (A.2) is

$$\begin{aligned}
&\frac{\sigma_j^2}{\lambda_j\tau^2}\int_0^\tau\int_0^\tau \sin(\sqrt{\lambda_j}t_1)\cos(\sqrt{\lambda_j}t_1)\sin(\sqrt{\lambda_j}t_2)\cos(\sqrt{\lambda_j}t_2)\\
&\times\int_0^{t_1\wedge t_2}\cos^2(\sqrt{\lambda_j}r)\,dr\,dt_1dt_2 \qquad (A.3)\\
&=\frac{\sigma_j^2}{\lambda_j\tau^2}\int_0^\tau\int_0^\tau \sin(\sqrt{\lambda_j}t_1)\cos(\sqrt{\lambda_j}t_1)\sin(\sqrt{\lambda_j}t_2)\cos(\sqrt{\lambda_j}t_2)\\
&\times\left(\frac{\sin(2\sqrt{\lambda_j}t_1\wedge t_2)+2\sqrt{\lambda_j}t_1\wedge t_2}{4\sqrt{\lambda_j}}\right)dt_1dt_2. \qquad (A.4)
\end{aligned}$$

Utilizing the symmetry of the double integral in $t_1$ and $t_2$, (A.4) becomes

$$\frac{\sigma_j^2}{2\lambda_j^{3/2}\tau^2}\int_0^\tau\int_0^{t_2}\sin(\sqrt{\lambda_j}t_1)\cos(\sqrt{\lambda_j}t_1)\left(\sin(2\sqrt{\lambda_j}t_1)+2\sqrt{\lambda_j}t_1\right)\,dt_1 \tag{A.5}$$
$$\times\sin(\sqrt{\lambda_j}t_2)\cos(\sqrt{\lambda_j}t_2)\,dt_2$$
$$=\frac{\sigma_j^2}{32\lambda_j^2\tau^2}\int_0^\tau\left(4\sin(2\sqrt{\lambda_j}t)-\sin(4\sqrt{\lambda_j}t)-8\sqrt{\lambda_j}t\cos(2\sqrt{\lambda_j}t)+4\sqrt{\lambda_j}t\right) \tag{A.6}$$
$$\times\sin(\sqrt{\lambda_j}t)\cos(\sqrt{\lambda_j}t)\,dt$$
$$=\frac{\sigma_j^2}{768\lambda_j^{5/2}\tau^2}\Bigg(\sin\left(6\sqrt{\lambda_j}\tau\right)-9\sin\left(4\sqrt{\lambda_j}\tau\right)+12\sqrt{\lambda_j}\tau\cos\left(4\sqrt{\lambda_j}\tau\right) \tag{A.7}$$
$$+9\sin\left(2\sqrt{\lambda_j}\tau\right)-24\sqrt{\lambda_j}\tau\cos\left(2\sqrt{\lambda_j}\tau\right)+24\sqrt{\lambda_j}\tau\Bigg).$$

The middle two terms of (A.2) are of the form

$$\frac{\sigma_j^2}{\lambda_j\tau^2}\int_0^\tau\int_0^\tau\cos(\sqrt{\lambda_j}t_1)\cos(\sqrt{\lambda_j}t_1)\sin(\sqrt{\lambda_j}t_2)\cos(\sqrt{\lambda_j}t_2) \tag{A.8}$$
$$\times\int_0^{t_1\wedge t_2}\sin(\sqrt{\lambda_j}r)\cos(\sqrt{\lambda_j}r)\,dr\,dt_1dt_2$$
$$=\frac{\sigma_j^2}{2\lambda_j^{3/2}\tau^2}\int_0^\tau\int_0^\tau\cos(\sqrt{\lambda_j}t_1)\cos(\sqrt{\lambda_j}t_1)\sin(\sqrt{\lambda_j}t_2)\cos(\sqrt{\lambda_j}t_2) \tag{A.9}$$
$$\times(1-\cos^2(\sqrt{\lambda_j}t_1\wedge t_2))dt_1dt_2.$$

Since this double integral is not symmetric in $t_1$ and $t_2$, we split (A.9) into two double integrals:

$$\frac{\sigma_j^2}{2\lambda_j^{3/2}\tau^2}\int_0^\tau\int_0^{t_2}\cos(\sqrt{\lambda_j}t_1)\cos(\sqrt{\lambda_j}t_1)\sin(\sqrt{\lambda_j}t_2)\cos(\sqrt{\lambda_j}t_2)$$
$$\times(1-\cos^2(\sqrt{\lambda_j}t_1))dt_1dt_2 \tag{A.10}$$
$$+\frac{\sigma_j^2}{2\lambda_j^{3/2}\tau^2}\int_0^\tau\int_0^{t_1}\cos(\sqrt{\lambda_j}t_1)\cos(\sqrt{\lambda_j}t_1)\sin(\sqrt{\lambda_j}t_2)\cos(\sqrt{\lambda_j}t_2)$$
$$\times(1-\cos^2(\sqrt{\lambda_j}t_2))dt_2dt_1$$
$$=\frac{\sigma_j^2}{64\lambda_j^{4/2}\tau^2}\int_0^\tau\sin(\sqrt{\lambda_j}t_2)\cos(\sqrt{\lambda_j}t_2)(4\sqrt{\lambda_j}t_2-\sin(4\sqrt{\lambda_j}t_2))dt_2 \tag{A.11}$$
$$+\frac{\sigma_j^2}{8\lambda_j^{4/2}\tau^2}\int_0^\tau\cos(\sqrt{\lambda_j}t_1)\cos(\sqrt{\lambda_j}t_1)(\cos^4\left(\sqrt{\lambda_j}\,t_1\right)-2\cos^2\left(\sqrt{\lambda_j}\,t_1\right)+1)dt_1.$$

Finally, to obtain the sum of the middle two terms of (A.2), multiply (A.11) by $-2$ and integrate:

$$\frac{-\sigma_j^2}{768\lambda_j^{5/2}\tau^2}\left(\sin\left(6\sqrt{\lambda_j}\tau\right)+9\sin\left(2\sqrt{\lambda_j}\tau\right)-24\sqrt{\lambda_j}\tau\cos\left(2\sqrt{\lambda_j}\tau\right)\right) \tag{A.12}$$
$$-\frac{\sigma_j^2}{768\lambda_j^{5/2}\tau^2}\left(\sin\left(6\sqrt{\lambda_j}\tau\right)-3\sin\left(4\sqrt{\lambda_j}\tau\right)-3\sin\left(2\sqrt{\lambda_j}\tau\right)+12\sqrt{\lambda_j}\tau\right).$$

The last term of (A.2) is

$$\frac{\sigma_j^2}{\lambda_j\tau^2}\int_0^\tau\int_0^\tau\cos(\sqrt{\lambda_j}t_1)\cos(\sqrt{\lambda_j}t_1)\cos(\sqrt{\lambda_j}t_2)\cos(\sqrt{\lambda_j}t_2)$$
$$\times\int_0^{t_1\wedge t_2}\sin^2(\sqrt{\lambda_j}r)\,dr\,dt_1dt_2 \tag{A.13}$$
$$=\frac{\sigma_j^2}{\lambda_j\tau^2}\int_0^\tau\int_0^\tau\cos(\sqrt{\lambda_j}t_1)\cos(\sqrt{\lambda_j}t_1)\cos(\sqrt{\lambda_j}t_2)\cos(\sqrt{\lambda_j}t_2)$$
$$\times\left(\frac{-\sin(2\sqrt{\lambda_j}t_1\wedge t_2)+2\sqrt{\lambda_j}t_1\wedge t_2}{4\sqrt{\lambda_j}}\right)dt_1dt_2. \tag{A.14}$$

Again utilizing the symmetry of the double integral in $t_1$ and $t_2$, (A.14) becomes

$$\frac{\sigma_j^2}{2\lambda_j^{3/2}\tau^2}\int_0^\tau\int_0^{t_2}\cos(\sqrt{\lambda_j}t_1)\cos(\sqrt{\lambda_j}t_1)\left(-\sin(2\sqrt{\lambda_j}t_1)+2\sqrt{\lambda_j}t_1\right)dt_1$$
$$\times\cos(\sqrt{\lambda_j}t_2)\cos(\sqrt{\lambda_j}t_2)\,dt_2 \tag{A.15}$$
$$=\frac{\sigma_j^2}{32\lambda_j^{4/2}\tau^2}\int_0^\tau(8\lambda_jt_2^2+8\sqrt{\lambda_j}t_2\sin\left(2\sqrt{\lambda_j}t_2\right)+\cos\left(4\sqrt{\lambda_j}t_2\right)$$
$$+8\cos\left(2\sqrt{\lambda_j}t_2\right)-9)\cos(\sqrt{\lambda_j}t_2)\cos(\sqrt{\lambda_j}t_2)\,dt_2 \tag{A.16}$$
$$=\frac{\sigma_j^2}{768\lambda_j^{5/2}\tau^2}\Bigg(32\lambda_j^{3/2}\tau^3+48\lambda_j\tau^2\sin\left(2\sqrt{\lambda_j}\tau\right)-12\lambda_j^{1/2}\tau\cos\left(4\sqrt{\lambda_j}\tau\right)-60\lambda_j^{1/2}\tau \tag{A.17}$$
$$+\sin\left(6\sqrt{\lambda_j}\tau\right)+18\sin\left(4\sqrt{\lambda_j}\tau\right)-3\sin\left(2\sqrt{\lambda_j}\tau\right)\Bigg).$$

Summing together (A.7), (A.12), and (A.17) we obtain the covariance of $\boldsymbol{\alpha}_j(\tau)$:

$$\mathrm{COV}[\boldsymbol{\alpha}_j(\tau)]=\boldsymbol{\Phi}_j(\mathbf{s})\boldsymbol{\Phi}_j^T(\mathbf{s})\frac{\sigma_j^2}{192\lambda_j^{3/2}}\Bigg(8\lambda_j^{1/2}\tau+12\sin(2\sqrt{\lambda_j}\tau)$$
$$-12\lambda_j^{-1/2}\tau^{-1}+3\lambda_j^{-1}\tau^{-2}\sin(4\sqrt{\lambda_j}\tau)\Bigg). \tag{A.18}$$

By a similar computation, we obtain the covariance of $\boldsymbol{\beta}_j(\tau)$:

$$\mathrm{COV}[\boldsymbol{\beta}_j(\tau)] = \boldsymbol{\Phi}_j(\mathbf{s})\boldsymbol{\Phi}_j^T(\mathbf{s})\frac{\sigma_j^2}{192\lambda_j^{3/2}}\Bigg(8\lambda_j^{1/2}\tau - 12\sin(2\sqrt{\lambda_j}\tau) + 36\lambda_j^{-1/2}\tau^{-1} \\ + 24\lambda_j^{-1/2}\tau^{-1}\cos(2\sqrt{\lambda_j}\tau) - 3\lambda_j^{-1}\tau^{-2}\sin(4\sqrt{\lambda_j}\tau) - 24\lambda_j^{-1}\tau^{-2}\sin(2\sqrt{\lambda_j}\tau)\Bigg). \tag{A.19}$$

Using $\tau = p/\sqrt{\lambda_j}$, the covariance can be written in terms of periods:

$$\mathrm{COV}[\boldsymbol{\alpha}_j(p)] = \boldsymbol{\Phi}_j(\mathbf{s})\boldsymbol{\Phi}_j^T(\mathbf{s})\frac{\sigma_j^2}{192\lambda_j^{3/2}}\Big(8p + 12\sin(2p) - 12p^{-1} + 3p^{-2}\sin(4p)\Big) \tag{A.20}$$

$$\mathrm{COV}[\boldsymbol{\beta}_j(p)] = \boldsymbol{\Phi}_j(\mathbf{s})\boldsymbol{\Phi}_j^T(\mathbf{s})\frac{\sigma_j^2}{192\lambda_j^{3/2}}\Bigg(8p - 12\sin(2p) + 36p^{-1} + 24p^{-1}\cos(2p) \\ - 3p^{-2}\sin(4p) - 24p^{-2}\sin(2p)\Bigg). \tag{A.21}$$

# APPENDIX B

# CURL-SQUARED OPERATOR

In this section, we discuss the curl-squared operator in detail. We seek the solutions of the eigenvalue problem:

$$\nabla \times \left( [\mu(\mathbf{x})]^{-1} \nabla \times \mathbf{\Phi} \right) - \lambda \epsilon(\mathbf{x}) \mathbf{\Phi} = 0 \tag{B.1}$$

on the domain $\Gamma = [0, L_1] \times [0, L_2] \times [0, L_3] \subset \mathbb{R}^3$ with periodic boundary conditions. We first prove that the curl operator is symmetric. Let $\mathbf{u}, \mathbf{v} \in H^1(\Gamma)$. We will use the multidimensional integration by parts:

$$\int_\Gamma \partial_{x_i} uv d\mathbf{x} = \int_{\partial\Gamma} uvn_i d\mathbf{x} - \int_\Gamma u \partial_{x_i} v d\mathbf{x} \tag{B.2}$$

where $\mathbf{n} = (n_1, n_2, n_3)$ is the unit outward normal defined on the boundary $\partial\Gamma$. Observe

$$\begin{aligned}
\langle \nabla \times \mathbf{u}, \mathbf{v} \rangle_{L_2} &= \int_\Gamma (\nabla \times \mathbf{u}) \cdot \mathbf{v} d\mathbf{x} \\
&= \int_{\partial\Gamma} (u_3 v_1 n_2 - u_2 v_1 n_3 + u_1 v_2 n_3 - u_3 v_2 n_1 + u_2 v_3 n_1 - u_1 v_3 n_2) d\mathbf{x} \\
&- \int_\Gamma (u_3 \partial_{x_2} v_1 - u_2 \partial_{x_3} v_1 + u_1 \partial_{x_3} v_2 - u_3 \partial_{x_1} v_2 + u_2 \partial_{x_1} v_3 - u_1 \partial_{x_2} v_3) d\mathbf{x} \\
&= \int_\Gamma \mathbf{u} \cdot (\nabla \times \mathbf{v}) \, d\mathbf{x} = \langle \mathbf{u}, \nabla \times \mathbf{v} \rangle_{L_2}
\end{aligned}$$

since $u_i$ and $v_i$ are periodic for all $i$ and so $(u_i v_j n_k) \mid_{x_k=0} = -(u_i v_j n_k) \mid_{x_k=L_k}$. So all of the boundary terms cancel and the curl operator is symmetric. Using (B.1) we obtain

$$(\lambda_k - \lambda_m) \int_\Gamma \epsilon(\mathbf{x}) \mathbf{\Phi}_k \cdot \mathbf{\Phi}_m d\mathbf{x} = 0 \tag{B.3}$$

which implies orthogonality with weight $\epsilon(\mathbf{x})$ whenever $\lambda_k \neq \lambda_m$.

*Eigenvector basis*

To illustrate the form of the solutions to (B.1), we derive the eigenvector basis in the homogeneous case: $\epsilon(\mathbf{x}) = \epsilon_0$. A natural function to consider when looking for eigenvectors of an operator is with a function of the form $e^{ikx}$. Since our problem is vectorial, we consider functions of the form

$$\mathbf{\Phi}(\mathbf{x}) = \mathbf{v} e^{i\mathbf{k}\cdot\mathbf{x}}, \quad \mathbf{v}, \mathbf{k} \in \mathbb{R}^3. \tag{B.4}$$

Observe

$$\nabla \times \mathbf{\Phi}(\mathbf{x}) = i e^{i\mathbf{k}\cdot\mathbf{x}} \begin{bmatrix} -v_2 k_3 + v_3 k_2 \\ v_1 k_3 - v_3 k_1 \\ -v_1 k_2 + v_2 k_1 \end{bmatrix} = i e^{i\mathbf{k}\cdot\mathbf{x}} \begin{bmatrix} 0 & -k_3 & k_2 \\ k_3 & 0 & k_1 \\ -k_2 & k_1 & 0 \end{bmatrix} \mathbf{v} =: i e^{i\mathbf{k}\cdot\mathbf{x}} A\mathbf{v}. \tag{B.5}$$

Thus, $\mathbf{\Phi}$ is an eigenfunction of the curl operator exactly when $\mathbf{v}$ is an eigenvector of $A$. So, for every $\mathbf{k} \in \mathbb{R}^3$, there is the skew-symmetric matrix

$$A_{\mathbf{k}} = \begin{bmatrix} 0 & -k_3 & k_2 \\ k_3 & 0 & -k_1 \\ -k_2 & k_1 & 0 \end{bmatrix} \tag{B.6}$$

which has 3 eigenvectors $\mathbf{v}_{\mathbf{k},1}, \mathbf{v}_{\mathbf{k},2}$, and $\mathbf{v}_{\mathbf{k},3}$ with corresponding eigenvalues $\lambda_{\mathbf{k},1}, \lambda_{\mathbf{k},2}$, and $\lambda_{\mathbf{k},3}$ such that

$$\mathbf{\Phi}_{\mathbf{k},j}(\mathbf{x}) = \mathbf{v}_{\mathbf{k},j} e^{i\mathbf{k}\cdot\mathbf{x}}, \quad j = 1, 2, 3 \tag{B.7}$$

is an eigenfunction of the curl operator with eigenvalues $i\lambda_{\mathbf{k},1}, i\lambda_{\mathbf{k},2}$, and $i\lambda_{\mathbf{k},3}$. The eigenfunctions as described satisfy the equation

$$\nabla \times \mathbf{\Phi}_{\mathbf{k},j}(\mathbf{x}) = i\lambda_{\mathbf{k},j} \mathbf{\Phi}_{\mathbf{k},j}(\mathbf{x}). \tag{B.8}$$

If $\Gamma = [-\pi, \pi]^3$, then $\mathbf{\Phi}_{\mathbf{k},j} \in L^2(\Gamma; \mathbb{R}^3)$ exactly when $\mathbf{k} \in \mathbb{Z}^3$. In this case, our collection of eigenfunctions is

$$\{\mathbf{\Phi}_{\mathbf{k},j}; \mathbf{k} \in \mathbb{Z}^3\}. \tag{B.9}$$

Lastly, observe that

$$\nabla \times \nabla \times (\mathbf{\Phi}) = -e^{i\mathbf{k}\cdot\mathbf{x}} A^2 \mathbf{v} \tag{B.10}$$

so that the eigenvalues of the curl-squared operator are exactly the squares of the eigenvalues of the curl operator: the eigenfunctions are constructed as above but with $v_{\mathbf{k},j}$ eigenvectors of the symmetric matrix $A_{\mathbf{k}}^2$ and the eigenvalues are $-\lambda_{\mathbf{k},j}$ where $\lambda_{\mathbf{k},j}$ are eigenvalues of $A_{\mathbf{k}}^2$.

The eigenvalues of $A_{\mathbf{k}}$ are

$$\lambda = \pm i|\mathbf{k}|, 0 \tag{B.11}$$

with the respective eigenvectors

$$\begin{bmatrix} -i|\mathbf{k}|_2 \, k_1^2 k_2 - i|\mathbf{k}|_2 \, k_2^3 - i|\mathbf{k}|_2 \, k_2 \, k_3^2 + k_1^3 k_3 + k_1 \, k_2^2 k_3 + k_1 \, k_3^3 \\ |\mathbf{k}|_2^2 \, k_3 k_2 + i|\mathbf{k}|_2 k_1^3 + i|\mathbf{k}|_2 k_1 \, k_2^2 + i|\mathbf{k}|_2 k_1 \, k_3^2 \\ -|\mathbf{k}|_2^2 \, (k_1^2 + k_2^2) \end{bmatrix} \tag{B.12}$$

$$\begin{bmatrix} i|\mathbf{k}|_2 \, k_1^2 k_2 + i|\mathbf{k}|_2 \, k_2^3 + i|\mathbf{k}|_2 \, k_2 \, k_3^2 + k_1^3 k_3 + k_1 \, k_2^2 k_3 + k_1 \, k_3^3 \\ |\mathbf{k}|_2^2 \, k_3 k_2 - i|\mathbf{k}|_2 k_1^3 - i|\mathbf{k}|_2 k_1 \, k_2^2 - i|\mathbf{k}|_2 k_1 \, k_3^2 \\ -|\mathbf{k}|_2^2 \, (k_1^2 + k_2^2) \end{bmatrix} \tag{B.13}$$

$$\begin{bmatrix} k_1 \\ k_2 \\ k_3 \end{bmatrix}. \tag{B.14}$$

Notice that each component of the vector $\mathbf{v}_{\mathbf{k},j}$ is zero for a nonzero $\mathbf{k}$.

# APPENDIX C

## STATEMENT OF APPROVAL FOR PUBLISHED WORKS

Permission for replication of the content of the publication "Sensor Placement Sensitivity and Robust Reconstruction of Wave Dynamics from Multiple Sensors"[5] has been granted by all authors. The authors are Bryce M. Barclay, Eric J. Kostelich, and Alex Mahalov. This publication was replicated and is the content of chapter 2. The content of chapter 2 was first published in SIAM Journal on Applied Dynamical Systems in Vol. 21 No. 4, published by the Society for Industrial and Applied Mathematics (SIAM).

# APPENDIX D

# LINK TO CODE

The code for the algorithms developed in this dissertation can be found at

`https://github.com/BryceBarclay/Wave_Dynamics.git`